STUDY OF HIGGS AT LHC ENERGY USING CMS DETECTOR

A THESIS

submitted to the

FACULTY OF SCIENCE

PANJAB UNIVERSITY CHANDIGARH

for the degree of

DOCTOR OF PHILOSOPHY

2007

Ashok Kumar

CENTRE OF ADVANCED STUDY IN PHYSICS

PANJAB UNIVERSITY CHANDIGARH

Dedicated to my revered teachers

&

lovable parents

Acknowledgement

As I stand at the threshold of earning my doctorate, I am overwhelmed when I recall all the people who have helped me to get this far. First and the foremost, I would like to thank my Ph.D. advisors Prof. Suman Beri and Prof. J. M. Kohli for their constant support, judicious guidance and invaluable inspiration.

Prof. Suman Beri is remarkable in her continual patience, kind insight, and helpful suggestions in tackling problems in my research. Her enthusiasm, curiosity and suggestions in high energy research is truly inspirational.

Prof. J. M. Kohli has always been readily available for help and support. I acknowledge him for his generosity and approachability in every step of my research.

I sincerely thank Chairman, Department of Physics, Panjab University for providing adequate facilities to work in the department. I also thank Head, Department of Physics, Guru Nanak Dev University, Amritsar and my colleagues for all their help and support in completing my Ph.D.

I am very grateful to Dr. Ritva Kinnunen from HIP-Helsinki, who constantly helped me in Higgs simulation physics analysis. Many thanks to Dr. Sami Lehti for his help in full detector simulation and reconstruction software. I acknowledge Dr. Alexandra Nikitenko, Coordinator - CMS Higgs group, for helpful physics discussions.

My special thanks to Prof. A. Gurtu, Spokesperson India-CMS Collaboration for his help and support throughout. I also thank entire India-CMS Collaboration (DU, BARC, TIFR members) for their help in hardware and software activities. Many Thanks to Prof. N. K. Mondal and Dr. K. Sudhakar for their help in carrying out HO fabrication and testing at TIFR and installation work at CERN. I would also like to acknowledge Prof. Sunanda Banerjee, Prof. Sudeshna Banerjee, Dr. Pawel De Barbaro, Dr. G. Majumdar, and Dr. S. K. Dugad for their help in test beam analysis. I thank Prof. N. K. Ganguly, Prof. T. Aziz, Dr. K. Majumdar, and Dr. M. Guchait for their valuable inputs.

I would like to thank Prof. J.B. Singh and Prof. Manjit kaur for their support and encouragement. I also thank Mr. V. K. Bhandari and Mr. Baljinder Singh for their help in Electronics and hardware activities. I also wish to thank Dr. Vipin Bhatnagar, Mr. Sanjeev Gautam and Dr. Rajwant Kaur for providing help in computer facilities. I would like to thank PU-EHEP group members (specially Mr. Gain and Mr. Sohan) for *their help in administrative jobs pertaining to my research work.*

I specially thank Mr. Harinder Singh for his help, support and encouragement during all the HO hardware activities we have done together.

This research has been supported and funded by Department of Science and Technology (DST), India. The financial support by DST is duly acknowledged. I would also like to thank Department of Atomic Energy (DAE) for funding my international CERN visits. I also thank all members of International CMS Collaboration for providing valuable inputs and suggestions in many steps of my research.

I would like to express my gratitude to my parents and brother Satish for their love and support. I would like to thank all my friends including Birbikram, Chandel, Sushil, Narendra, Rakesh and Lab members to make this journey more enjoyable, exciting and motivational.

Last but not least, My deepest and sincere gratitude to the almighty "God' for inspiring and guiding this humble being.

July 17, 2007 *Ashok Kumar*

Abstract

One of the major physics goals of the Large Hadron Calorimeter (LHC) is to discover Higgs boson and study its properties. The Higgs boson is the fundamental particle which is responsible for electroweak symmetry breaking as predicted by the Standard Model. A discovery of Higgs boson and studying its properties will enhance our understanding of origin of mass. The Compact Muon Solenoid (CMS) is one of the experiments which is optimized for Higgs searches and understanding the unanswered question in particle physics at high energy of TeV scale. Present study is a step towards it, and work has been done towards fabrication of scintillator detectors of outer hadron calorimeter (HO) for CMS detector, testing and installation at CERN and physics analysis work for Higgs to dimuon channel. This research work is done as a member of CMS collaboration and briefly given below:

The whole responsibility of fabrication, testing and installation of HO in CMS detector was undertaken by TIFR and Panjab University. HO is divided in to 5 rings ±2, ±1, 0 (with inner and outer layers). Panjab University took responsibility for the fabrication of HO ±1 ring. The plastic scintillator sheets were procured from Bicron BC408. After cutting them in to required dimensions grooving and side polishing was done using sophisticated controlled CNC machine. Stringent quality control was maintained at each step. These scintillator tiles were assembled in to bigger HO modules called tray. The testing and quality control of the assembled trays was done with three tests, Cosmic muon test, sliding wire source Co^{60} test and collimated Cs^{137} X-Y scanner test. The fabrication of the fiber readouts called as pigtail was also done and quality control tests were performed. These assembled trays were transported to CERN.

HO trays were cross-checked for stable response by using wire-source and collimated X-Y scanning at CERN. After that HO trays were mounted on the test beam table of H2 beamline along with other hadron calorimeter (HCAL) detectors and electromagnetic calorimeter (ECAL) for studying the real effects of particles at different energies. Data taking shifts were taken at CERN during 2003 test beam. ECAL was exposed to electrons for its calibration purpose. Muon beam of 150 GeV energy was used to calibrate hadron barrel (HB) and HO. The linearity in response of ECAL with HCAL was checked at different particle energies. We analyzed the data for different energy pions. The response of HO in addition to HB was understood with and without ECAL configurations.

Detectors were exposed to low energy and high energy pions. Constrained to outside of the CMS tracker and ECAL, the hadron barrel calorimeter was found to be thin to effectively absorb high energy hadrons near the central region. This would lead to degraded sensitivity for establishing new physics signals whose main signature can be missing E_T. The addition of sensitive detector layers of HO, ensures much smaller energy leakage and hence improvement in the energy resolution.

The CMS detector should be able to elucidate the mechanism of electroweak symmetry breaking and to study a variety of other topics related to physics at the TeV scale. After Higgs discovery, it would be more important and more challenging to understand its properties, in particular their couplings to the Standard Model (SM) particles. Higgs couple to the SM particles proportional to their masses. It is necessary to confirm the proportionality of m_μ for the Higgs coupling $H\mu^+\mu^-$ as predicted by the SM and also to know that Higgs particle that generates mass for the weak boson is also responsible for mass generation of the second generation of fermions. The relevance of studying $H \to \mu^+\mu^-$ stands in understanding its couplings to second generation leptons. The present study has been performed with multi-purpose event generator, PYTHIA and some comparisons are also performed with ALPGEN. The electro-weak qqZ background was generated with MadGraph. Since full simulation is used to validate the real physics prior to real experimental data, the CMS full detector response was simulated using the package OSCAR. It is an application of the Geant4 toolkit for detector description and simulation. OSCAR is used to describe the detector geometry and materials. It also includes and uses information about the magnetic field. OSCAR reads the individual generated events and simulates the effects of energy loss, multiple scattering and showering in the detector materials with Geant4. The digitization (simulation of the electronic response), the emulation of the level-1 and high level triggers (HLT), and the offline reconstruction of physics objects was done with the CMS full-reconstruction ORCA package. The cuts were optimized using cut-based analysis method to study signal to background ratio. The main backgrounds needed to be simulated are coming from Z+jets, $t\bar{t}$ and qqZ events. The main source of systematic uncertainty on the determination of the background level in the known signal area is the uncertainty of the jet energy scale through the forward jet tagging and central jet veto methods. An upper bound was calculated according to Standard Model hypothesis i.e. Higgs couplings to fermions is directly proportional to their masses.

List of Publications

Publications in International Journals

1. G. L. Bayatian, A. Kumar, S. B. Beri, J. M. Kohli et al. (CMS Collaboration), J. Phys. G: Nucl. Part. Phys. 34 (2007) 995-1579.

2. S. Abdullin, A. Kumar, S. B. Beri, J. M. Kohli et al., ***"Design, Performance, and Calibration of CMS Forward Calorimeter Wedges "*** to be submitted to Nucl. Inst. and Meth. (NIM).

3. S. Abdullin, A. Kumar, S. B. Beri, J. M. Kohli et al., ***"Longitudinal Shower Profiles Measured in CMS HCAL and Comparison with Geant4"*** preprint submitted to Elsevier Science.

4. S. Abdullin, A. Kumar, S. B. Beri, J. M. Kohli et al., ***"Design, Performance, and Calibration of CMS Hadron-Barrel Calorimeter Wedges "*** preprint submitted to European Physical Journal A.

5. S. Abdullin, A. Kumar, S. B. Beri, J. M. Kohli et al., ***"Synchronisation and Timing in the CMS Hadron Calorimeter"*** to be submitted to Nucl. Inst. and Meth (NIM).

CMS Research Publications

1. B. S. Acharya, A. Kumar, S. B. Beri, J. M. Kohli et al., CMS NOTE 2006/127, ***"The CMS Outer Hadron Calorimeter"***.

2. G. Baiatian, A. Kumar, S. B. Beri, J. M. Kohli et al., CMS NOTE 2006/044, ***"Design, Performance, and Calibration of CMS Forward Calorimeter Wedges "***.

3. G. Baiatian, A. Kumar, S. B. Beri, J. M. Kohli et al., CMS NOTE 2006/143, ***"Energy Response and Longitudinal Shower Profiles Measured in CMS HCAL and Comparison With Geant4"***.

4. S. Abdullin, A. Kumar, S. B. Beri, J. M. Kohli et al., CMS NOTE 2006/139, ***"Synchronisation and Timing in the CMS HCAL"***.

5. S. Abdullin, A. Kumar, S. B. Beri, J. M. Kohli et al., CMS NOTE 2006/138, ***"Design, Performance, and Calibration of CMS Hadron-Barrel Calorimeter Wedges "***.

6. Ashok Kumar, Suman Beri, Ritva Kinnunen, CMS AN 2006/105, ***"Search for the Standard Model Higgs Boson Decaying to Muons in the Weak Gauge Boson Fusion"***.

Research Publications in Conferences/Symposiums

1. Ashok Kumar, Suman Beri, Ritva Kinnunen, Proceedings of XVII DAE HEP symposium, Dec. 2006, IIT, Kharagpur, India, ***"Study of Higgs Decay to dimuons"***.

2. Ashok Kumar, Suman Beri, J. M. Kohli et al., (CMS Collaboration), Proceedings of XVI DAE HEP symposium, Nov. 2004, SINP, Kolkata, India, ***"Response of CMS Calorimeter to electrons and muons"***.

3. Ashok Kumar, Suman Beri, J. M. Kohli et al., (India CMS Collaboration), Proceedings of XV DAE HEP symposium, Nov. 2002, University of Jammu, Jammu, India, ***"Fabrication of outer hadron calorimeter scintillator module for CMS detector"***.

4. Ashok Kumar, Suman Beri, J. M. Kohli et al., (India CMS Collaboration), Proceedings of XV DAE HEP symposium, Nov. 2002, University of Jammu, Jammu, India, ***"Quality Control Check and Testing of Outer hadron calorimeter Scintillator Module for CMS detector"***.

5. Ashok Kumar, Suman Beri, J. M. Kohli et al., (India CMS Collaboration) poster presentation in concern to ***"Indian contribution to CERN since 1960"*** on the occasion of CERN's 50th anniversary, Oct. 2004, CERN, Geneva, Switzerland.

Conferences/Workshops Attended

1. **XVII DAE-BRNS Symposium on High Energy Physics** held at IIT, Kharagpur, India, Dec. 11-15, 2006.
2. **International conference on Computing in High Energy and Nuclear Physics** held at TIFR, Mumbai, India, Feb. 13-17, 2006.
3. **XVI DAE-BRNS Symposium on High Energy Physics** held at Saha Institute of Nuclear Physics, Kolkata, India, Nov. 29-Dec.03, 2004.
4. **XV DAE-BRNS Symposium on High Energy Physics** held at University of Jammu, Jammu, India, Nov. 11-15, 2002.
5. **42nd DAE-BRNS Symposium on Nuclear physics** held at Panjab University, Chandigarh, India, Dec. 27-31, 1999.
6. **91st Session of Indian Science Congress** held at Panjab University, Chandigarh, India, Jan. 3-7, 2004.
7. **CERN's 50th Anniversary Open House** held at CERN, Geneva, Switzerland, Oct. 16-19, 2004.
8. **Workshop on LHC Physics** held at TIFR, Mumbai, India, Sept. 04-08, 2006.
9. **International CERN school of computing** held at TIFR, Mumbai, India, Feb. 11-12, 2006.
10. **V SERC school on Experimental High Energy Physics** held at Panjab University, Chandigarh, India, March 7-27, 2005.
11. **IV SERC school on Experimental High Energy Physics** held at SINP-VECC, Kolkata, India, 16 Feb.- 1st March, 2003.
12. Seminar on **Computational Techniques in Physics** held at Panjab University, Chandigarh, India, March 7-8, 2002.

Contents

List of Figures

List of Tables

Chapter 1

Introduction

1.1 The Particles and Their Interactions

Particle physics is a branch of physics that studies the elementary constituents of matter and radiation, and the interactions between them. It is also called high energy physics, because many elementary particles do not occur under normal circumstances in nature, but can be created and detected during energetic collisions of other particles, as is done in particle accelerators. Particle physicists try to understand the nature at the smallest scales possible. Today, we know that atoms do not represent the smallest unit of matter. Particles called quarks and leptons seem to be the fundamental building blocks - but perhaps there is something even smaller. Physicists are still far from understanding why a proton has about 2,000 times more mass than an electron. And on top of it all, scientists suspect a whole new class of undiscovered symmetric particles to complete the subatomic family.

Quantum effects constantly produce particles and antiparticles "out of nothing",only to have them disappear few moments later. And space itself can either be almost flat or curved, depending on the amount of matter it contains. We have also learned that many subatomic processes can be reversed in time - but not every process. There are some small but crucial differences in the way matter and antimatter behave. Could it be the reason why our universe is made of matter, while antimatter has all but disappeared? Astrophysicists have found that less than 10 percent of the mass of the entire universe consists of the kind of “luminous” matter that we can see. What is the dark matter that makes up the rest of the universe? How can we find out? Though we understand many important properties of the fundamental building blocks of our universe, there are untold mysteries still to solve. Advances in technology allow physicists to build more powerful and sophisticated instruments to look deeper and deeper inside matter. Like adventurers entering unknown territory, physicists forge ahead into ever smaller dimensions.

Quantum electrodynamics (QED)is the quantum field theory which describes the properties of electromagnetic radiation and its interaction with electrically charged matter in the framework of quantum theory . QED deals with processes involving the creation of elementary particles from electromagnetic energy, and with the reverse processes in which a particle and its antiparticle annihilate each other and produce energy. The fundamental equations of QED apply to the emission and absorption of light by atoms and the basic interactions of light with electrons and other elementary particles. Charged particles interact by emitting and absorbing photons, the particles of light that transmit electromagnetic forces. For this reason, QED is also known as the quantum theory of light. QED is based on the elements of quantum mechanics laid down by such physicists as P. A. M. Dirac , W. Heisenberg , and W. Pauli during the 1920s, when photons were first postulated. In 1928 Dirac discovered an equation describing the motion of electrons that incorporated both the requirements of quantum theory and the theory of special relativity . During the 1930s, however, it became clear that QED as it was then postulated gave the wrong answers for some relatively elementary problems. For example, although QED correctly described the magnetic properties of the electron and its antiparticle, the positron, it proved difficult to calculate specific physical quantities such as the mass and charge of the particles. Proceeding independently, Freeman J. Dyson, Richard P. Feynman, J. S. Schwinger and Shinichiro Tomonaga refined and fully developed QED.

They showed that two charged particles can interact in a series of processes of increasing complexity, and that each of these processes can be represented graphically through a diagramming technique developed by Feynman. Not only do these diagrams provide an intuitive picture of the process but they show how to precisely calculate the variables involved. The mathematical structures of QED later were adapted to the study of the strong interactions between quarks, which is called quantum chromodynamics .

Quantum chromodynamics (QCD) is quantum field theory which describes the properties of the strong interactions between quarks and between protons and neutrons in the framework of quantum theory . Quarks possess a distinctive property called color that governs their binding together to form other elementary particles . Analogous to electric charge in charged particles, color is of three varieties, arbitrarily designated as red, blue, and green, analogous to positive and negative charges, three anticolor varieties. Just as positively and negatively charged particles form electrically neutral atoms, colored quarks form particles with no net color. Quarks interact by emitting and absorbing massless particles called gluons , each of which carries a color-anticolor pair. Eight kinds of gluons are required to transmit the strong force between quarks, e.g., a blue quark might interact with a green quark by exchanging a blue-antigreen gluon. The concept of color was proposed by Oscar Greenberg and independently by Yoichiro Nambu in 1964. The theory was confirmed when quarks were shown to emit gluons during studies of high-energy particle collisions at DESY, Hamburg.

Another interaction known as weak interaction was first recognized in cataloging the types of nuclear radioactive decay chains, as alpha, beta, and gamma decays. After deep probe in the beta decay processes it was understood that the fundamental weak interaction occur for all fundamental particles except gluons and photons. In other way, the weak interaction affects all left-handed leptons and quarks. It is the only force affecting neutrinos (except for gravitation, which is negligible on laboratory scales). The weak interaction is unique in a number of respects:

- It is the only interaction capable of changing flavor.
- It is the only interaction which violates parity symmetry P (because it only acts on left-handed particles). It is also the only one which violates CP.
- Having short range and strength 10^{13} times less than that of the nuclear force, this interaction is mediated by relatively heavy gauge bosons ($W^{\pm}$ and Z^0). This unusual feature is explained in the Standard Model by the Higgs mechanism.

QCD is nearly identical in mathematical structure to quantum electrodynamics (QED) and to the unified theory of weak and electromagnetic interactions advanced by Steven Weinberg and Abdus Salam . Physicists call the theoretical framework that describes the interactions between elementary building blocks (quarks and leptons) and the force carriers (bosons) the Standard Model. It describes the strong, weak, and electromagnetic fundamental forces, using mediating gauge bosons. The species of gauge bosons are the gluons, W^- and W^+ and Z^0 bosons, and the photons, respectively. Gravity is not yet part of this framework, and a central question of 21st century particle physics is the search for a quantum formulation of gravity that could be included in the Standard Model. The model also contains 24 fundamental particles, which are the constituents of matter. Finally, it predicts the existence of a type of boson known as the Higgs boson, which has yet to be discovered.

The Standard Model (SM) [1], of strong and electroweak interactions is in excellent agreement with the experimental measurements. However, the core of the theory, the electroweak symmetry breaking manifesting itself in the heavy vector bosons W and Z and the massless photon, is the least known sector of the model. The SM Higgs boson would be the first fundamental scalar particle. It has the nice features of allowing the spontaneous symmetry breaking giving gauge bosons their masses and it also provides fermions their masses through Yukawa couplings. The Higgs mechanism [2], provides a mathematical explanation to this phenomenon, and one of the main tasks of upcoming Large Hadron

Collider (LHC) at CERN, Geneva will be the quest for experimental evidence of the Higgs particle, or any observable of some other symmetry breaking mechanism.

1.2 LHC-CMS International Effort

The Large Hadron Collider (LHC) at CERN, Geneva is on the verge of completion. The LHC will be the highest energy accelerator in the world for many years following its completion after Tevatron which is operating on center of mass energy $\sqrt{s} = 2$ TeV). Fig. 1.1 shows a variety of SM cross section for hadron collisions of various energy, and marks off in particular Tevatron and LHC. The LHC will provide two proton beams, circulating in apposite directions, at an energy of 7 TeV each (center-of-mass $\sqrt{s} = 14$ TeV). The Compact Muon Solenoid (CMS) is a general purpose experiment, designed to study the physics at TeV scale at the LHC [12]. It currently involves more than 2000 physicists from more than 150 institutions and 37 countries. It is expected that the data produced at the LHC will elucidate the electroweak symmetry breaking mechanism (EWSB) and provide evidence of physics beyond the Standard Model. CMS will also be an instrument to perform precision measurements of the parameters of the Standard Model, mainly the result of the very high event rates for a luminosity of 2×10^{33} cm^{-2}s^{-1}. Details of are given in Chapter 3.

1.3 Present Research Work

International CMS collaboration is responsible for the design, construction and commissioning of CMS experiment at LHC. The present research work comprises of three main aspects of CMS experiment, starting from hardware detector fabrication to physics analysis in one of the Standard Model Higgs decay. Namely

- Hardware: fabrication, testing and installation of scintillator detectors.
- Test beam study for understanding actual particle-detector interaction.

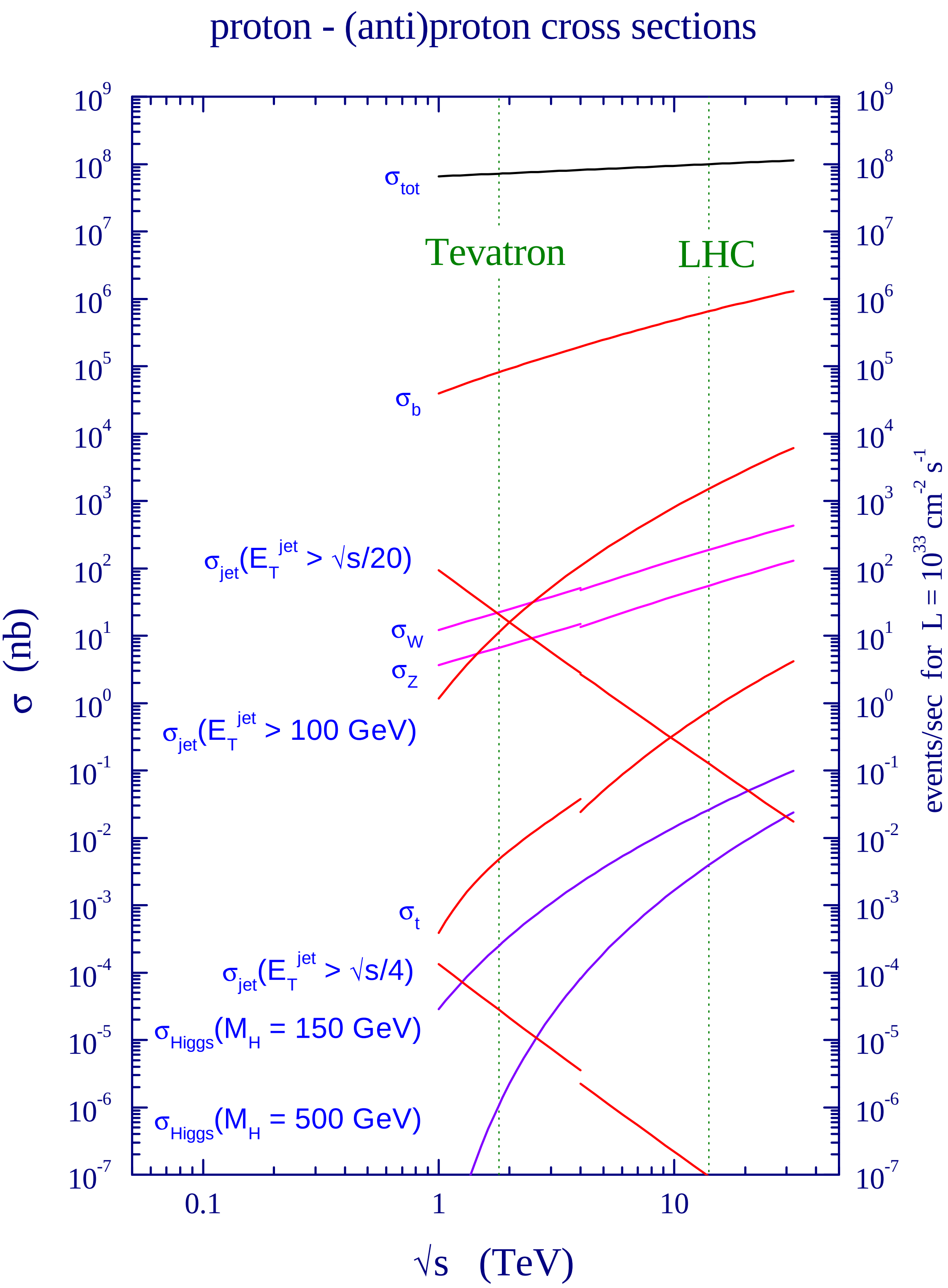

Figure 1.1: Various SM "standard candle" cross sections at hadron colliders of varying energy, with Tevatron and LHC marked in particular. Discontinuities are due to the difference between $p\bar{p}$ for Tevatron and pp for LHC [4].

- Physics simulation studies of Standard Model $H \rightarrow \mu^+\mu^-$ channel.

This work is part of International CMS collaboration CERN, Geneva [5] and contribution of India-CMS collaboration (EHEP and HECR groups from TIFR - Mumbai, University of Delhi - Delhi, BARC - Mumbai and Panjab University - Chandigarh). In all the activities mentioned below we participated and contributed significantly.

1.3.1 Hardware Activities

Detector R&D and Fabrication

Indian contingent mainly Panjab University, Chandigarh and Tata Institute of Fundamental Research (TIFR), Mumbai took the complete responsibility for the fabrication of the outer hadron calorimeter (HO) [4] for the CMS detector. The addition of sensitive detector layers of HO ensures high energy shower containment and improvement in the energy resolution. The HO is physically divided in to 5 rings in η confirming to the muon ring structure. The rings are numbered $0, \pm 1, \pm 2$. Each ring of the HO is divided in to 12 identical ϕ sectors and each sector has 6 slices in ϕ. The ϕ slices of a layer are identical in all sectors. In each ϕ slice the scintillator is further divided along η.

In total 432 trays were needed for completing HO. The grooving of the all ring 1 scintillator tiles was done at Panjab University. My contribution was to measure thickness of ring 1 tiles and then test them using cosmic ray test set up at Panjab University. These scintillator tiles were then shipped to TIFR for tray assembly work. Details of HO are given in Chapter 4.

Assembly, Testing and Installation

All the tray assembly work has been performed at TIFR. HO scintillator tiles were assembled in the single tray units. The performance of outer hadron calorimeter is checked for its sensitivity to produce a usable signal for a given radiation and relation between the amount of scintillation light and the charge contained in the output signal i.e integral of the pulse with respect to time by using photo-sensor and charge sensitive analog to digital convertor (ADC). Testing and quality control of the HO detector module is done mainly by three tests namely cosmic-muon test, radioactive wire source test and radioactive X-Y scanning [4]. My contribution was to participate in HO tray assembly work and to test them with all three tests at TIFR. HO trays were also cross checked for their light response using wire source and X-Y scanning set up at CERN.

1.3.2 CMS HCAL Test Beam Studies at CERN

HO trays were mounted on the test beam table of H2 beamline of the along with other hadron calorimeter (HCAL) detectors and electromagnetic calorimeter (ECAL) for studying the real effects of particles of different energies. ECAL was exposed to 100 GeV electrons for its calibration purpose. The muon beam of 150 GeV energy was used to calibrate hadron barrel (HB) and HO. The wire source runs were also used to calibrate HB and HO trays. The data was analyzed to see the response of CMS calorimeters i.e. ECAL and HCAL at different energy electrons and pions respectively. The HCAL test beam study helps to understand the performance of the CMS hadronic calorimeter in measuring energies of single electrons, pions and muons. It helps in calculating preliminary calibration constants which can be used in simulation and reconstruction softwares. It also helps in directing trigger related algorithms for physics analysis. The test beam data allows us to evaluate and study the physics potential of the HCAL detectors.

1.3.3 Physics Simulation Studies

Study of Higgs decay to dimuon channel

The $H \to \mu^+\mu^-$ channel would be the first observation for a Higgs boson to decay to second-generation fermions. It is necessary to confirm the proportionality of m_μ for the Higgs coupling $H\mu^+\mu^-$ as predicted by the SM and hence Higgs particle that generates mass for the weak boson is also responsible for mass generation of the second generation of fermions. Discovery potential for the SM Higgs boson in the $H \rightarrow \mu^+\mu^-$ decay channel with $m_H = 120$ GeV/c^2 in the Weak Gauge Boson fusion (WBF) at the low luminosity was also studied [30], with full simulation and reconstruction of the CMS detector and with a cut-based analysis method. A resolution of 1.2% was obtained for the reconstructed Higgs boson mass. The main backgrounds from Z+jets, $t\bar{t}$ and qqZ events were simulated. An efficient background suppression was obtained tagging the forward quark jets in the $qq \rightarrow qqH$ production process. The analysis method used leads to a signal to background ratio of 46% [29]. Assuming an uncertainty of 100% for the present background determination an upper bound of 6.6 fb is obtained for $qq \rightarrow qqH, H \rightarrow \mu^+\mu^-$ at 95% Confidence level (CL) for $\mathrm{m}_H = 120$ GeV/c^2.

1.4 Outline of Thesis

Chapter 2 deals with the Standard Model details in relevance to Higgs Physics possible specially at LHC energy. The reach of upcoming hadron collider is discussed with limits on Higgs mass in specific decay channels. Chapter 3 is review of LHC and CMS detector. CMS is foreseen in relevance to its tracking, calorimetry and particle detection. Chapter 4 is comprehensive in understanding Panjab University - TIFR effort for the CMS detector. The outer hadron calorimeter (HO) is a thin scintillator layer of about 10 cm for containing the high E_T jets. The fabrication, testing and installation of HO is also discussed. The work is collectively done at Panjab University, TIFR and CERN. Chapter 5 contains testing of HO by the accelerated muons and pions of varying energies as well as calibration and response of ECAL and HCAL . Chapter 6 gives us insight to the CMS object-oriented softwares which were understood, installed and used for generating and reconstructing event samples for physics simulation activities and usage of LHC Grid in carrying out data production. The study of Higgs decay in to dimuon channel is explained in chapter 6. The relevance of this channel stands in the Higgs couplings to second generation fermions. Conclusions are given in chapter 7.

Bibliography

[1] S. Glashow: Nucl. Phys. 22 (1961) 579;
S. Weinberg: Phys. Rev. Letter. 19 (1967) 1264;
A. Salam in *Elementary Particle Theory*, Nobel Symp. N. 8, ed. by N. Svartholm, Aspenäsgården, Stockholm (1968), 367.

[2] P. Higgs: Phys. Lett. 12 (1964) 132; Phys. Rev. Lett. 13 (1964) 508; Phys. Rev. 1156 (1966) 145;
F. Englert and R. Brout: Phys.Rev. Lett. 13 (1964) 321;
G. S. Guralnik, C. R. Hagen and T. W. Kibble: Phys. Rev. Lett 13 (1964) 585.

[3] G. L. Bayatian, A. Kumar, S. B. Beri, J. M. Kohli et al. (The CMS Collaboration), J. Phys. G: Nucl. Part. Phys. 34 (2007) 995-1579.

[4] F. Gianotti, Phys. Rept. 403, 379 (2004).

[5] G. L. Bayatian, A. Kumar, S. B. Beri, J. M. Kohli et al. (The CMS Collaboration), http://cms.cern.ch/.

[6] B. S. Acharya, A. Kumar, S. B. Beri, J. M. Kohli et al., The CMS Outer Hadron Calorimeter, CMS NOTE 2006/127.

[7] Ashok Kumar, Suman Beri, Ritva Kinnunen, Search for the Standard Model Higgs Boson Decaying to Muons in the Weak Gauge Boson Fusion, CMS AN 2006/105.

Chapter 2

Standard Model and Higgs Physics

2.1 Overview

All known particle physics phenomena are well described within the Standard Model (SM) of elementary particles and their fundamental interactions. The SM provides a very elegant theoretical framework and it has successfully passed very precise tests which at present are at the 0.1% level [1].

We understand by elementary particles, the point-like constituents of matter with no known substructure up to the present limits of $10^{-18} - 10^{-19}m$. These are of two types, the basic building blocks of matter themselves known as matter particles and the intermediate interaction particles. The first ones are fermions of spin $s = \frac{1}{2}$ and are classified into leptons and quarks. The known leptons are electron (e^-), muon (μ^-) and tau (τ^-) with electric charge $Q = -1$ (all charges are given in units of the elementary charge e) and the corresponding neutrinos ν_e, ν_μ and ν_τ with $Q = 0$. The known quarks are of six different flavors up (u), down (d), strange (s), charm (c), bottom (b) and top (t). They have fractional charge $Q = \frac{2}{3}, -\frac{1}{3}, -\frac{1}{3}, \frac{2}{3}, -\frac{1}{3}$ and $\frac{2}{3}$ respectively.

The quarks have an additional quantum number, the color, which for them can be of three types, generically denoted as q_i, $i = 1, 2, 3$. We know that color is not seen in nature and therefore the elementary quarks must be confined into the experimentally observed matter particles, the hadrons. These colorless composite particles are classified into baryons and mesons. The baryons are fermions made of three quarks, qqq, as for instance the proton, $p \sim uud$, and the neutron, $n \sim ddu$. The mesons are bosons made of one quark and one antiquark as for instance the pions, $\pi^+ \sim u\bar{d}$ and $\pi^- \sim d\bar{u}$.

The second kind of elementary particles are the intermediate interaction particles. All the relevant interactions in particle physics are mediated by the exchange of bosons. The photon, γ, is the exchanged particle in the electromagnetic interactions, the eight gluons $g_\alpha, \alpha = 1, ..8$ mediate the strong interactions among quarks, and the three weak bosons, W^+, W^-, Z are the corresponding intermediate bosons of the weak interactions. The gravitational interaction is supposed to be mediated by graviton.

As for the theoretical aspects, the SM is a quantum field theory that is based on the gauge symmetry $SU(3)_C \times SU(2)_L \times U(1)_Y$. This gauge group includes the symmetry group of the strong interactions, $SU(3)_C$, and the symmetry group of the electroweak interactions, $SU(2)_L \times U(1)_Y$. The group symmetry of the electromagnetic interactions, $U(1)_{em}$, appears in the SM as a subgroup of $SU(2)_L \times U(1)_Y$ and it is in this sense that the weak and electromagnetic interactions are said to be unified.

The gauge sector of the SM is composed of eight gluons which are the gauge bosons of $SU(3)_C$ and the γ, $W^\pm$ and Z particles which are the four gauge bosons of $SU(2)_L \times U(1)_Y$. The main physical properties of these intermediate gauge bosons are as follows. The gluons are massless, electrically neutral and carry color quantum number. There are eight gluons since they come in eight different colors. The consequence of the gluons being colorful is that they interact not just with the quarks but also with themselves. The weak bosons, $W^\pm$ and Z are massive particles and also self-interacting. The $W^\pm$ are charged with $Q = \pm 1$ respectively and the Z is electrically neutral. The photon γ is massless, chargeless and non-selfinteracting.

Concerning the range of the various interactions, it is well known the infinite range of the electromagnetic interactions as it corresponds to an interaction mediated by a massless gauge boson, the short range of the weak interactions of about $10^{-16} cm$

correspondingly to the exchange of a massive gauge particle with a mass of the order of 100 GeV and, finally, the strong interactions whose range is not infinite, as it should correspond to the exchange of a massless gluon, but finite due to the extra physical property of confinement. In fact, the short range of the strong interactions of about $10^{-13}cm$ corresponds to the typical size of the lightest hadron.

As for the strength of the three interactions, the electromagnetic interactions are governed by the size of the electromagnetic coupling constant e or equivalently $\alpha = \frac{e^2}{4\pi}$ which at low energies is given by the fine structure constant, $\alpha(Q = m_e) = \frac{1}{137}$. The weak interactions at energies much lower than the exchanged gauge boson mass, M_V, have an effective (weak) strength given by the Fermi constant $G_F = 1.167 \times 10^{-5}\, GeV^{-2}$. The name of strong interactions is due to their comparative stronger strength than the other interactions. This strength is governed by the size of the strong coupling constant g_S or equivalently $\alpha_S = \frac{g_s^2}{4\pi}$ and varies from large values to low energies, $\alpha_S(Q = m_{hadron}) \sim 1$ up to the vanishing asymptotic limit $\alpha_S(Q \to \infty) \to 0$. This last limit indicates that the quarks behave as free particles when they are observed at infinitely large energies or, equivalently, infinitely short distances and it is known as the property of asymptotic freedom.

Finally, regarding the present status of the matter particle content of the SM the situation is summarized as follows.

The fermionic sector of quarks and leptons are organized in three families with identical properties except for mass. The particle content in each family is:

$$1^{st} \text{ family: } \begin{pmatrix} \nu_e \\ e^- \end{pmatrix}_L, \; e_R^-, \; \begin{pmatrix} u \\ d \end{pmatrix}_L, \; u_R, \; d_R$$

$$2^{nd} \text{ family: } \begin{pmatrix} \nu_\mu \\ \mu^- \end{pmatrix}_L, \; \mu_R^-, \; \begin{pmatrix} c \\ s \end{pmatrix}_L, \; c_R, \; s_R$$

$$3^{rd} \text{ family: } \begin{pmatrix} \nu_\tau \\ \tau^- \end{pmatrix}_L, \tau_R^-, \begin{pmatrix} t \\ b \end{pmatrix}_L, t_R, b_R$$

and their corresponding antiparticles. The left-handed and right-handed fields are defined by means of the chirality operator γ_5 as usual,

$$e_L^- = \frac{1}{2}(1-\gamma_5)e^-,\ e_R^- = \frac{1}{2}(1+\gamma_5)e^-$$

and they transform as doublets and singlets of $SU(2)_L$ respectively.

The scalar sector of the SM is not experimentally confirmed yet. The fact that the weak gauge bosons are massive particles, $M_{W^\pm}$, $M_{Z^0} \neq 0$, indicates that $SU(2)_L \times U(1)_Y$ is not a symmetry of the vacuum. In contrast, the photon being massless reflects that $U(1)_{em}$ is a good symmetry of the vacuum. Therefore, the spontaneous symmetry breaking (SSB) pattern in the SM must be:

$$SU(3)_C \times SU(2)_L \times U(1)_Y \rightarrow SU(3)_C \times U(1)_{em}$$

The above pattern is implemented in the SM by means of the so-called Higgs mechanism [2] which provides the proper masses to the $W^\pm$ and Z^0 gauge bosons and to the fermions, and leaves as a consequence the prediction of a new particle: the Higgs boson particle. This must be scalar and electrically neutral. This particle has not been seen in the experiments so far [3].

2.2 Standard Model

The electroweak sector of the Standard Model (SM) is described as a $SU(2) \times U(1)$ gauge theory. In its basic form it describes all the electroweak interactions between fermions by the exchange of massless vector bosons.

The Lagrangian density of the free massless boson fields can be written as the sum of the $U(1)$ gauge field B_μ and the three real $SU(2)$ gauge fields W^i_μ , i = 1,2,3 . It takes the form

$$L^B = -\frac{1}{4}F_{B\mu\nu}(x)F_B^{\mu\nu}(x) - \frac{1}{4}F^i_{W\mu\nu}(x)F_W^{i\mu\nu}(x) \tag{2.1}$$

where the field tensors are defined as

$$F_B^{\mu\nu} = \partial^\nu B^\mu - \partial^\mu B^\nu \tag{2.2}$$

$$F_W^{i\mu\nu} = \partial^\nu B^{i\mu} - \partial^\mu B^{i\nu} \tag{2.3}$$

Through the transformation

$$A_\mu = \cos\theta_W B_\mu + \sin\theta_W B^3_\mu \tag{2.4}$$

$$Z_\mu = \sin\theta_W B_\mu - \cos\theta_W B^3_\mu \tag{2.5}$$

$$W^\pm_\mu = \frac{1}{\sqrt{2}}W^1_\mu \mp iW^2_\mu \tag{2.6}$$

Where the Weinberg angle θ_W is a free parameter, the Lagrangian describing the free vector boson field can be written as

$$L^B = -\frac{1}{4}F_{\mu\nu}(x)F^{\mu\nu}(x) - \frac{1}{2}F^\dagger_{W\mu\nu}(x)F_W^{\mu\nu}(x) - \frac{1}{4}F_{Z\mu\nu}(x)F_Z^{\mu\nu}(x) \tag{2.7}$$

where $F^{\mu\nu}$ is now the electromagnetic field tensor and $F_W^{\mu\nu}$, $F_Z^{\mu\nu}$ the field tensors for the $W^\pm$ and Z^0 fields. The $W^\pm$ and Z^0 fields can be made massive by including the terms

$$m^2_W W^\dagger_\mu(x)W^\mu(x) + \frac{1}{2}m^2_Z Z_\mu(x)Z^\mu(x). \tag{2.8}$$

Introducing masses in this way, however, causes the Lagrangian density no longer to be invariant under the $U(1)$ gauge transformation

$$\psi(x) \rightarrow \psi'(x) = e^{iY\xi(x)}\psi(x) \tag{2.9}$$

where ψ is the different boson fields with weak hypercharge Y and ξ(x) any differentiable function. The Lagrangian including the mass terms will not be invariant under $SU(2)$

gauge transformations. Ignoring the lack of gauge invariance results in a theory which is not renormalizable and thus only adequate for describing tree level processes. The spontaneous symmetry breaking is the way to give the $W^{\pm}$ and Z^0 vector bosons mass while keeping the gauge theory $SU(2) \times U(1)$ invariant.

2.3 Spontaneous Symmetry Breaking

The Goldstone model is a simple model with spontaneous symmetry breaking. Starting with a classical theory, take a Lagrangian density

$$L = \partial^{\mu}\varphi^{*}\partial_{\mu}\varphi - V(\varphi), \tag{2.10}$$

where φ is a complex field

$$\varphi = \frac{\sqrt{2}}{2}[\varphi_1 + i\varphi_2] \tag{2.11}$$

and $V(\varphi)$ the potential energy

$$V(\varphi) = \mu^2|\varphi|^2 + \lambda|\varphi|^4. \tag{2.12}$$

The constants μ^2 , λ are real with λ positive to make the total field energy bounded from below. The Lagrangian is invariant under the global $U(1)$ transformation describing rotations in the complex plane. It should be noted that φ is a function of the space-time coordinate 'x' which is suppressed to simplify the notation.

Requiring that the vacuum, the lowest energy state, is invariant under Lorentz transformations and translations implies that $\varphi(x)$ is a constant in this vacuum state. Two different possibilities exist for the vacuum state depending on the parameter μ^2 .

If μ^2 is positive the situation is quite normal with the minimum potential energy at $\varphi = 0$. If instead μ^2 is negative, the minimum energy no longer corresponds to a unique value of φ but is instead degenerate (as shown in Fig. 2.1) with the minimum as a ring in the complex plane

$$\varphi_{V_{min}} = \sqrt{\frac{-\mu^2}{2\lambda}}e^{i\theta}, \quad 0 \leq \theta < 2\pi. \tag{2.13}$$

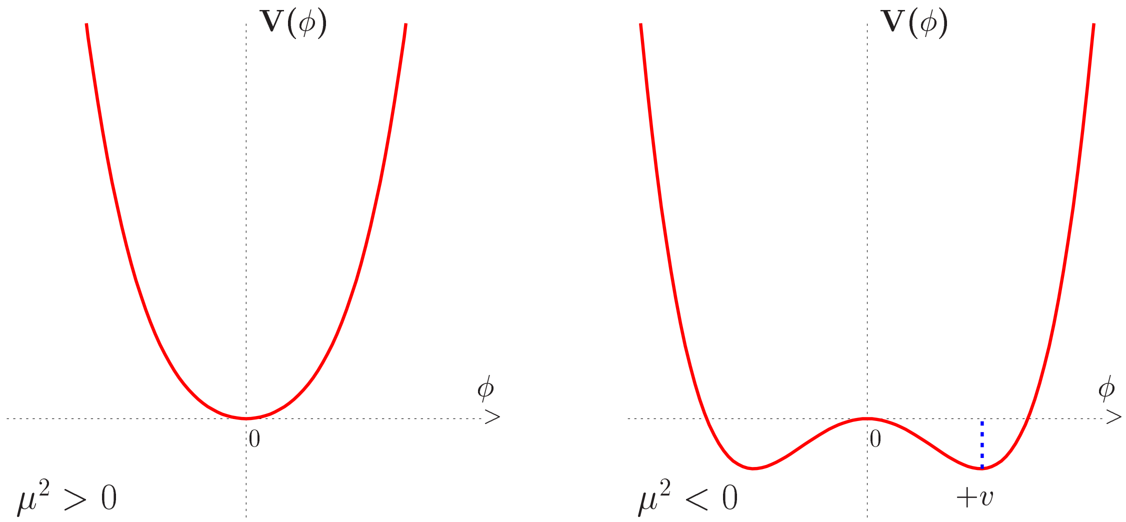

Figure 2.1: If $\mu^2 > 0$, ground state is having unique vacuum and if $\mu^2 < 0$, there is degeneracy in vacuum states.

As the Lagrangian (2.10) is invariant under rotations in the complex plane of φ each direction is equally good and setting $\theta = 0$ such that

$$\varphi_{V_{min}} = \sqrt{\frac{-\mu^2}{2\lambda}} \equiv \frac{v}{\sqrt{2}} \tag{2.14}$$

can be done without loss of generalization. A theory where the vacuum has less symmetry than the Lagrangian is called a theory with spontaneous symmetry breaking. The deviation from the chosen minimum can be described by the two real fields σ and η defined through

$$\varphi = \frac{\sqrt{2}}{2}[v + \sigma + i\eta]. \tag{2.15}$$

The Lagrangian (2.10) rewritten in terms of σ and η is

$$L = \frac{1}{2}\partial^\mu\sigma\partial_\mu\sigma - \lambda v^2\sigma^2 + \frac{1}{2}\partial^\mu\eta\partial_\mu\eta - \lambda v\sigma[\sigma^2 + \eta^2] - \frac{1}{4}\lambda[\sigma^2 + \eta^2]^2 + c \tag{2.16}$$

with c a constant of interest only for general relativity. Taking the higher order terms as interaction terms the free Lagrangian reads

$$L = \frac{1}{2}\partial^\mu\sigma\partial_\mu\sigma - \lambda v^2\sigma^2 + \frac{1}{2}\partial^\mu\eta\partial_\mu\eta. \tag{2.17}$$

It is seen that σ and η in fact are two real Klein-Gordon fields. By quantizing these fields the Lagrangian (2.17) describes two different spin 0 particle fields. The σ bosons will have mass

$$m_\sigma = v\sqrt{2\lambda} \tag{2.18}$$

rising from the σ^2 term while the η bosons will be massless. The masslessness of the η bosons are a direct consequence of the minimum being degenerate. The remaining terms from (2.16) can be treated as interactions among the σ and η particles through perturbation theory.

From the above situation it can be seen how the spontaneous symmetry breaking (SSB) of the U(1) symmetry caused by the degenerate energy minimum of the Lagrangian (2.10) creates a pertubative theory with a massive scalar boson.

2.4 Higgs Mechanism

There are three important properties of the Higgs Mechanism that are worth mentioning:

1. It respects the gauge symmetry of the Lagrangian.
2. It preserves the total number of polarization degrees.
3. It does not spoil the good high energy properties nor the renormalizability of the massless gauge theories.

Also following facts must be considered in order to see how the Higgs Mechanism is implemented in the $SU(2)_L \times U(1)_Y$ Gauge Theory in order to generate a mass for the weak gauge bosons, $W^\pm$ and Z^0:

1. The Lagrangian of the SM is gauge $SU(2)_L \times U(1)_Y$ symmetric. Therefore, anything we wish to add must preserve this symmetry.

2. We wish to generate masses for the three gauge bosons $W^{\pm}$ and Z^0 but not for the photon. Therefore, we need three would-be-Goldstone bosons, ϕ_+, ϕ_- and χ, which will combine with the three massless gauge bosons of the $SU(2)_L \times U(1)_Y$ symmetry.

3. Since $U(1)_{em}$ is a symmetry of the physical spectrum, it must be a symmetry of the vacuum of the Electroweak Theory.

From the above considerations we conclude that in order to implement the Higgs Mechanism in the Electroweak Theory we need to introduce 'ad hoc' and additional system that interacts with the gauge sector $SU(2)_L \times U(1)_Y$ in a gauge invariant manner and whose self-interactions, being also introduced 'ad hoc' must produce the wanted breaking, $SU(2)_L \times U(1)_Y \to U(1)_{em}$ with the three associated would-be-Goldstone bosons. This system is the so-called SBS of the Electroweak Theory.

So, what is called the Higgs mechanism is the extension of the spontaneous symmetry breaking to create massive vector bosons in a gauge invariant theory. Here it will be shown for a $U(1)$ theory. The idea is to replace the normal derivative in (2.10) with the covariant derivative

$$D_\mu = \partial_\mu + iqA_\mu. \tag{2.19}$$

Adding the Lagrangian of the free gauge field A_μ , results in

$$L = D^\mu \varphi^* D_\mu \varphi - V(\varphi) - \frac{1}{4} F_{\mu\nu} F^{\mu\nu} \tag{2.20}$$

This new Lagrangian is now invariant under the $U(1)$ gauge transformation

$$\begin{aligned} \varphi(x) \to \varphi'(x) &= \varphi(x) e^{iq\xi(x)} \\ A_\mu(x) \to A'_\mu(x) &= A_\mu(x) + \partial_\mu \xi(x), \end{aligned} \tag{2.21}$$

with ξ any differentiable function. Continuing in exactly the same way as for the Goldstone model with a negative μ^2 and expressing the Lagrangian in terms of the variables σ and

η as defined in (2.15) the result is

$$\begin{aligned} L = & \frac{1}{2}\partial^\mu\sigma\partial_\mu\sigma - \lambda v^2\sigma^2 + \frac{1}{2}\partial^\mu\eta\partial_\mu\eta \\ & - \frac{1}{4}F_{\mu\nu}F^{\mu\nu} + \frac{1}{2}q^2v^2A_\mu A\mu \\ & + qvA^\mu\partial_\mu\eta \\ & + \text{higher order terms.} \end{aligned} \tag{2.22}$$

The Lagrangian clearly has a massive vector boson field A and two scalar fields σ , η with η massless, but unfortunately also a term $A^\mu\partial_\mu\eta$ which does not fit in. It can not be understood as a pertubative interaction term since it is quadratic in the fields as the terms for the free field are. However, a careful analysis shows that the Lagrangian (2.22) has one more degree of freedom. This extra degree of freedom can be absorbed by choosing a specific gauge, i.e. performing a gauge transformation of the type (2.21), where $\varphi(x)$ has the form

$$\varphi(x) = \frac{\sqrt{2}}{2}[v + \sigma(x)]. \tag{2.23}$$

Such a gauge transformation is always possible and the chosen gauge is called the unitary gauge. In this gauge the η field disappears and what is left in the Lagrangian is

$$\begin{aligned} L = & \frac{1}{2}\partial^\mu\sigma\partial_\mu\sigma - \lambda v^2\sigma^2 \\ & - \frac{1}{4}F_{\mu\nu}F^{\mu\nu} + \frac{1}{2}q^2v^2A_\mu A\mu \\ & + \text{higher order terms.} \end{aligned} \tag{2.24}$$

In summary, it is seen that a complex scalar field and a massless vector field, both with two degrees of freedom, in (2.20) as a result of the Higgs mechanism was transformed in (2.24) into one real scalar field with one degree of freedom and a massive vector boson field with 3 degrees of freedom. A massless spin 1 particle has two transverse polarized states while a massive spin 1 particle has an additional longitudinal polarized state. It should be noted that the η field only disappears if the η bosons are massless. This requires the vacuum state to be degenerate i.e. the Higgs mechanism will only work with a degenerate vacuum.

The Higgs mechanism was demonstrated here for a $U(1)$ gauge invariant Lagrangian. To extend it to the $SU(2)\times U(1)$ gauge invariant Lagrangian of the electroweak theory is relatively simple. The starting point is a Lagrangian with a complex scalar doublet and four massless vector bosons. Counting degrees of freedom gives four from the scalars and eight from the vector bosons.

Through the Higgs mechanism the Lagrangian is transformed into one real scalar, three massive vector and one massless vector boson. The massless vector boson is of course to be identified with the photon and the single remaining scalar with the Higgs boson. Counting degrees of freedom again gives one from the Higgs, two from the photon and nine from the massive vector bosons, again adding up to twelve.

Introducing the masses of the vector bosons with one doublet of complex scalars is the simplest scenario, in principle an infinite number of scalar fields can be introduced. The simplest supersymmetric models instead have five scalar fields left after the Higgs mechanism, a doublet of charged scalars, two neutral scalars and one neutral pseudoscalar.

The masses of the particles in the Standard Model are given as

$$m_H = \sqrt{2\lambda}v, \quad m_W = \frac{1}{2}vg, \quad m_Z = \frac{m_W}{\cos\theta_W}, \tag{2.25}$$

where g is the weak coupling constant and θ_W the Weinberg angle. Using

$$v^2 = \frac{\sqrt{2}}{2G_F}, \quad \alpha = \frac{g^2\sin^2\theta_W}{4\pi}, \tag{2.26}$$

where G_F is the Fermi constant and α the fine structure constant, the vector boson masses can be expressed through G_F, α and $sin\theta_W$. With the Fermi constant measured from the muon lifetime and the Weinberg angle from the relative cross sections of neutral current ($\nu_\mu + p \rightarrow \nu_\mu + X$) and charge current ($\nu_\mu + p \rightarrow \mu + X$) processes it was possible to predict the masses of the vector bosons. Their discovery at the UA1 and UA2 experiments at the CERN S$p\bar{p}$S was a great victory for the electroweak theory.

The vacuum expectation value is easily extracted as

$$v = \frac{2m_W}{g} = 246 \text{ GeV}, \tag{2.27}$$

but there is no way to measure the value of λ before a discovery of the Higgs.

For reference the full electroweak and Higgs sector part of the Standard Model Lagrangian is given. It takes the form

$$L = L_0 + L_{FB} + L_{FH} + L_{BB} + L_{BH} + L_{HH} \tag{2.28}$$

where L_0 is the Lagrangian of the free fields

$$\begin{aligned} L_0 = &\bar{\psi}_f(i\partial\!\!\!/ - m_f)\psi_f \\ &- \frac{1}{4}F_{\mu\nu}F^{\mu}\nu \\ &- \frac{1}{2}F^{\dagger}_{W\mu\nu}F^{\mu\nu}_{W} + m_W^2 W^{\dagger}_{\mu}W^{\mu} \\ &- \frac{1}{4}F_{Z\mu\nu}F^{\mu\nu}_{Z} + \frac{1}{2}m_Z^2 Z_\mu Z^\mu \\ &+ \frac{1}{2}\partial^\mu\sigma\partial_\mu\sigma - \frac{1}{2}m_H^2\sigma^2, \end{aligned} \tag{2.29}$$

and the remaining terms the interaction between fermions and bosons, fermions and the Higgs, bosons and bosons, bosons and the Higgs and finally Higgs self interactions. Only the fermion Higgs interaction term

$$L_{FH} = -\frac{1}{v}m_f\bar{\psi}_f\psi_f\sigma \tag{2.30}$$

which will be important later is given here. A sum over all fermions is implicitly assumed in (2.29) and (2.30) with some terms disappearing if we consider neutrinos to be massless.

A remarkable feature of introducing massive fermions in the theory is that their interaction terms in the Lagrangian become proportional to their mass as seen in (2.30). While this makes it impossible to put constraints on the Higgs mass and the fermion masses, it has the consequence that the Higgs particle will couple to the fermions in proportion to their mass. The supersymmetric extensions of the Standard Model have different predictions for the coupling constants and hence a measurement of several coupling constants can be used to look into the theory behind the Higgs mechanism [4].

2.5 Experimental Verification of Standard Model

The Standard Model is a very successful description of the interactions of the components of matter at the smallest scales ($\leq 10^{-18}m$) and highest energies (~ 200 GeV) accessible to current experiments. After proposing basic elements of the Standard Model, correctness of the model is accumulated through increasing experimental evidence:

- observation of (approximate) scaling in deep inelastic scattering experiments, showing the existence of point-like scattering centers inside nucleons, later identified with quarks.
- observation of the c and b quarks.
- observation of neutral weak currents from Z exchange.
- observation of jet structure and three-jet final states resulting from gluon radiation in e^+e^- and hadron-hadron collisions.
- direct observation of the $W^\pm$ and Z^0 at the CERN $Sp\bar{p}S$ collider. Following these discoveries, ever more precise experiments at LEP has provided verification of the couplings of quarks and leptons to the gauge bosons at the level of 1-loop radiative corrections ($\sim O(10^{-3})$). Also, the top quark has been discovered with heavy mass of ($\sim 174GeV$).

With the recent direct observation of the ν_τ, only one particle from the Standard Model has yet to be discovered, the Higgs boson. The Higgs is very important because it holds the key to the generation of $W^\pm, Z^0$, quark and lepton masses.

2.6 Higgs Profile

One of the main challenges in high-energy physics is to understand electroweak symmetry breaking. In the Standard Model (SM), the electroweak interaction is described by a gauge field theory based on the $SU(2)_L \times U(1)_Y$ symmetry group. Masses can be introduced by the Higgs mechanism. In the simplest form, fundamental scalar Higgs fields fill the vacuum and acquire non-zero vacuum expectation values, and the $SU(2)_L \times U(1)_Y$ symmetry is spontaneously broken down to the electromagnetic $U(1)_{EM}$ symmetry. Gauge bosons and fermions obtain their masses by interacting with the vacuum Higgs fields. Associated with this description is the existence of massive scalar particles, Higgs bosons. The Higgs couplings to the electroweak gauge bosons and all fermions grow with their masses. The only unknown parameter of the Higgs boson itself is the value of its mass m_H.Once this is known, all production and decay properties of the SM Higgs boson will be fixed.

The mass of the SM Higgs boson is given by $m_H = \sqrt{2\lambda}v$. While the vacuum expectation value of the Higgs field, $v = (\sqrt{2}G_F)^{-1/2} = 246$ GeV, is fixed by the Fermi Coupling G_F, the quartic Higgs self-coupling λ is a free parameter, thus the mass m_H is not predicted by the SM. However, arguments based on the perturbativity of the theory can be used to place approximate upper and lower bounds upon the mass. Indirect experimental bounds for the SM Higgs boson mass are obtained from fits to precision measurements of the electroweak observables, and to the measured top quark and $W^{\pm}$ masses.

2.7 Theoretical Bounds on M_H

Theoretical bounds on the Higgs mass arise, even in the Standard Model, from two consistency requirements: (Non-)Triviality and vacuum stability. In the minimal supersymmetric Standard Model (MSSM), on the other hand, the Higgs self-coupling is given by the gauge couplings, which implies the upper bound $m_H \lesssim 135$ GeV. The mass bounds in the Standard Model arise from the scale dependence of couplings. Most relevant are the Higgs self-coupling λ and the top quark Yukawa coupling h_t which gives the top mass via $m_t = h_t v$. Other Yukawa couplings are much smaller and can be ignored. The renormalisation group equations for the couplings $\lambda(\mu)$ and $h_t(\mu)$ are

$$\mu\frac{\partial}{\partial\mu}\lambda(\mu) = \beta_\lambda(\lambda, h_t) = \frac{1}{(4\pi)^2}\left(12\lambda^2 - 12h_t^4 + \ldots\right) , \tag{2.31}$$

$$\mu\frac{\partial}{\partial\mu}h_t(\mu) = \beta_\lambda(\lambda, h_t) = \frac{h_t}{(4\pi)^2}\left(\frac{9}{2}h_t^2 - 8g_s^2 + \ldots\right) . \tag{2.32}$$

These equations imply that h_t decreases with increasing μ whereas the behavior of $\lambda(\mu)$ depends on the initial condition $\lambda(v)$, i.e., on the Higgs mass. For the Standard Model to be a consistent theory from the electroweak scale v up to some high-energy cutoff Λ, one needs to satisfy the following two conditions in the range $v < \mu < \Lambda$:

- The triviality bound: $\lambda(\mu) < \infty$. If λ would hit the Landau pole at some scale $\mu_L < \Lambda$, a finite value $\lambda(\mu_L)$ would require $\lambda(v) = 0$, i.e., the theory would be "trivial".

- The vacuum stability bound: $\lambda(\mu) > 0$. If λ would become negative, the Higgs potential would not be bounded from below anymore, and the electroweak vacuum would no longer be the ground state of the theory.

These two requirements define allowed regions in the $m_H - m_t$ plane as function of the cutoff Λ as shown in Fig. 2.2. For a given top mass, this translates into an upper and lower bound on the Higgs mass. For increasing Λ, the allowed region shrinks, and for the known top quark mass and $\Lambda \sim \Lambda_{GUT} \sim 10^{16}$ GeV, the Higgs mass is constrained to lie in a narrow region, 130 GeV $< m_H <$ 180 GeV as shown in Fig. 2.3.

The impressively narrow band of allowed Higgs masses, which one obtains from the triviality and vacuum stability bounds, assumes that the Standard Model is valid up to Λ_{GUT}, the scale of grand unification.

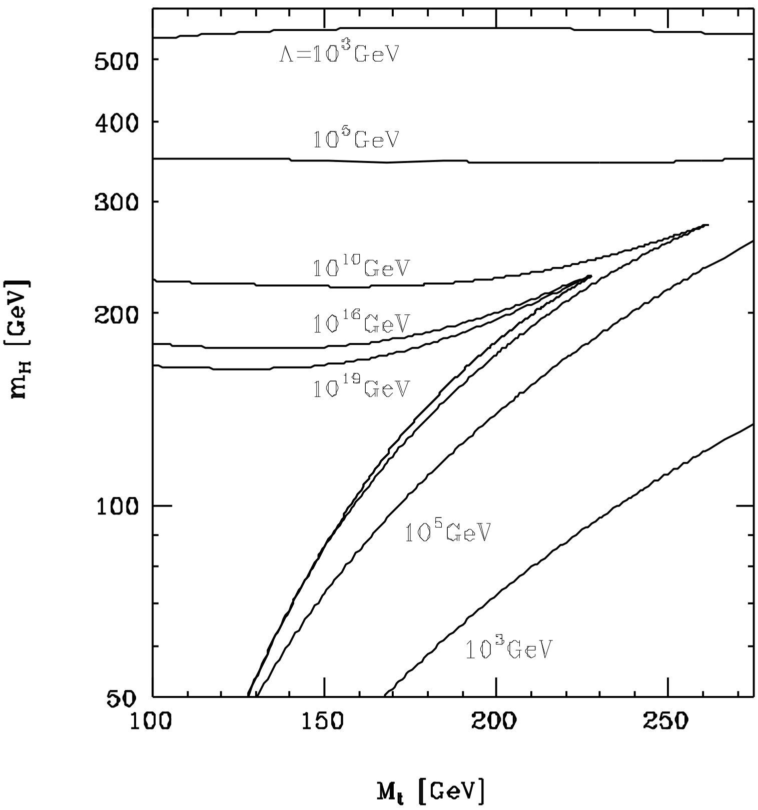

Figure 2.2: Bounds on the Higgs and top mass from triviality and vacuum stability. This plot shows the combined bounds for different values of Λ [6].

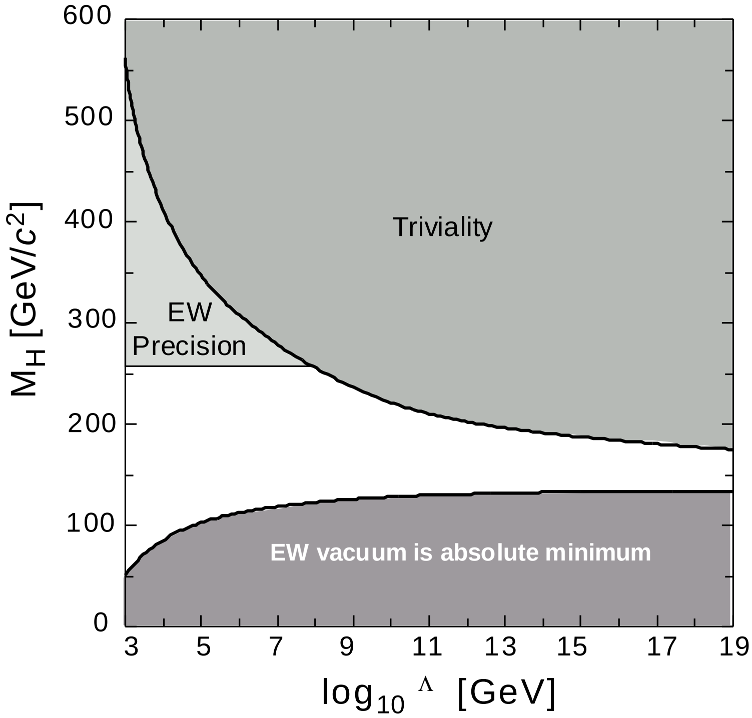

Figure 2.3: This plot gives the bounds on the Higgs mass for the known top mass [7].

2.8 Experimental Bounds on M_H

The SM Higgs boson has been searched for at LEP in the Higgs-strahlung process $e^+e^- \rightarrow HZ$ for center of mass energies up to $\sqrt{s} = 209$ GeV and with a large collected luminosity. By including more statistics, revision of backgrounds and reassessment of systematic errors, an lower bound $M_H \geq 114.4$ GeV is established at the 95% level [5].

The Higgs contributes to radiative corrections, in particular for the ρ parameter. Hence, precision measurements yield indirect constraints on the Higgs mass. The result of a global fit is shown in Fig. 2.4. The current 95% confidence level upper bound is $m_H < 185$ GeV, one should keep in mind, however, that the loop corrections used to determine the Higgs mass strongly depend on the top mass as well. A shift of a few GeV in the top mass, well within the current uncertainties, can shift the Higgs mass best fit by several tens of GeV.

2.9 Higgs Production at LHC

In the Standard Model, the main production mechanisms for Higgs particles at hadron colliders make use of the fact that the Higgs boson couples preferentially to the heavy particles, that is the massive $W^\pm$ and Z^0 vector bosons, the top quark, and to a lesser extent, the bottom quark. At LHC, four main Higgs production processes, as shown in Fig. 2.5, are, the gluon–gluon fusion mechanism (a), the weak vector boson fusion (WBF) processes (b), the associated production with $W^\pm/Z^0$ bosons (c), and the associated Higgs production with heavy top or bottom quarks (d):

The main production mechanism for a SM Higgs will be direct production via gluon-gluon fusion. The second largest cross-section is $\approx 20\%$ of the direct production for $m_H < 2m_Z$. In this process the initial state quarks will radiate W^0 or $Z^\pm$ bosons, which subsequently will produce the Higgs. The signature for this process are two jets in the forward region from the scattered incoming quarks and low hadronic activity in the

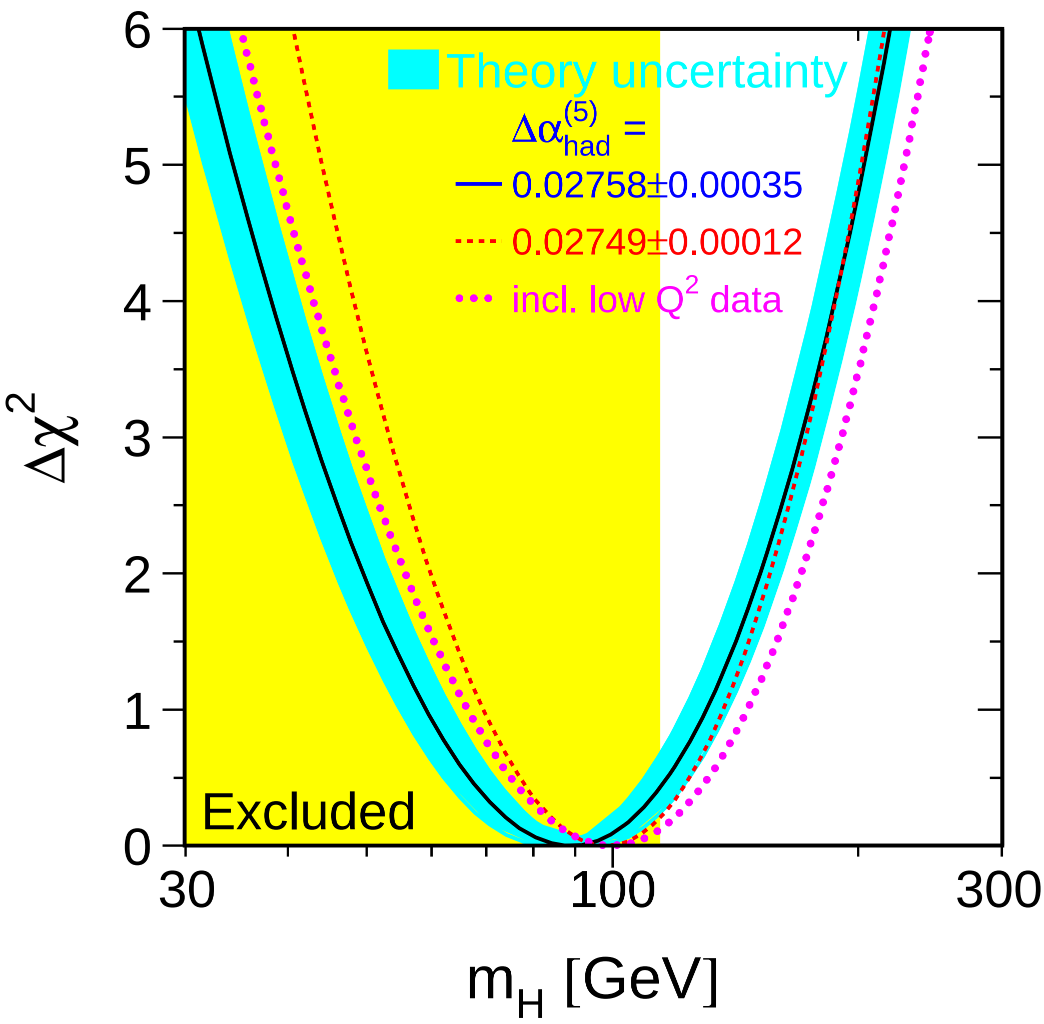

Figure 2.4: The blue-band plot showing the constraints on the Higgs mass from precision measurements [8]. The best fit and the width of the parabola vary, most notable due to shifts in the top mass and its uncertainty.

central region due to lack of color exchange between the quarks. This helps in reducing the backgrounds and thus the WBF processes offer a good discovery potential for Higgs masses below 150 GeV. Another mechanism to produce Higgs bosons at the LHC is its associated production together with a $W^{\pm}, Z^{0}, t\bar{t}$, or $b\bar{b}$. The cross-section of this process is of the order of 1-10% of the direct production and is sizeable for a Higgs mass below 200 GeV. These four different production will be the key to measure the Higgs boson parameters.

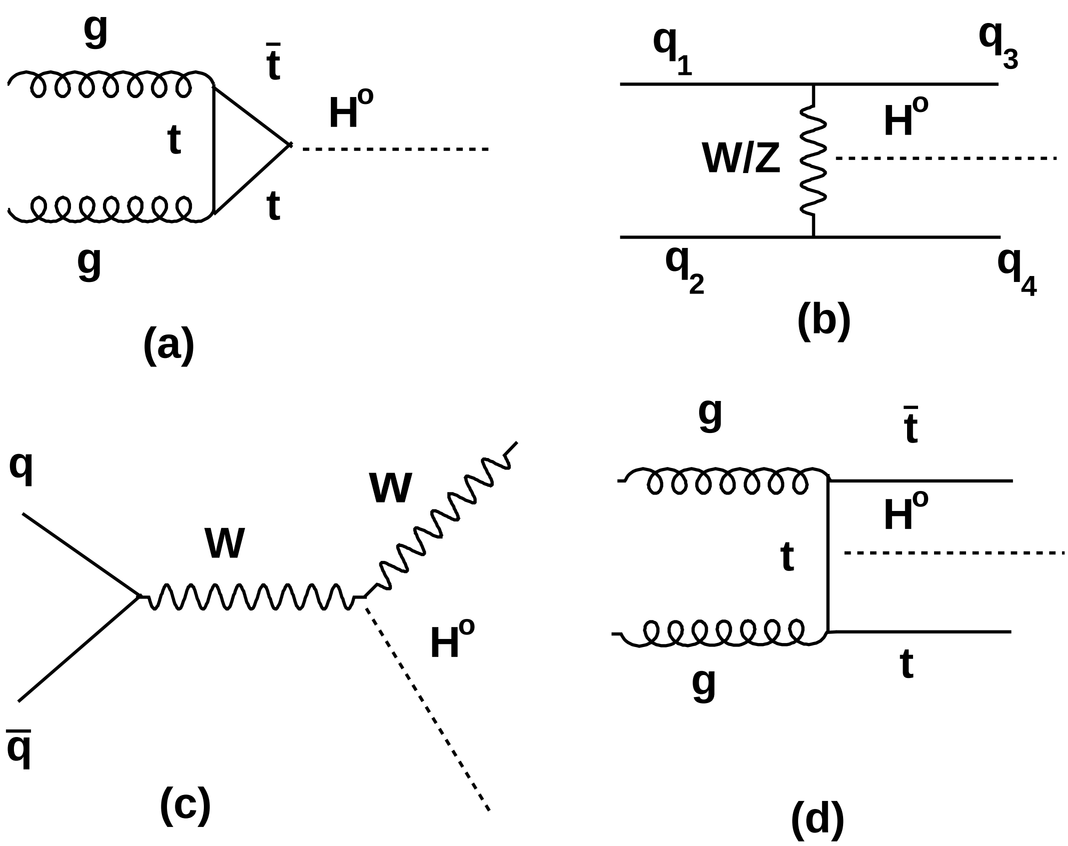

Figure 2.5: The dominant SM Higgs boson production mechanisms at LHC.

2.10 Higgs Search in Different Mass Regions

The SM Higgs boson will be searched at the LHC in various decay channels. Branching ratio of decay channels as a function of Higgs mass i.e. M_H is shown in Fig. 6.4. The choice on the decay channel depends on the signal rates and the signal-to-background ratios in the various mass regions. Three different mass regions can be distinguished, which will be discussed below.

Low mass region, $M_H < 130 GeV$

The most clean decay channel is the rare decay mode $H \rightarrow \gamma\gamma$ with a branching ratio of $\approx 10^{-3}$. The signal needs to be observed above a huge background. A powerful

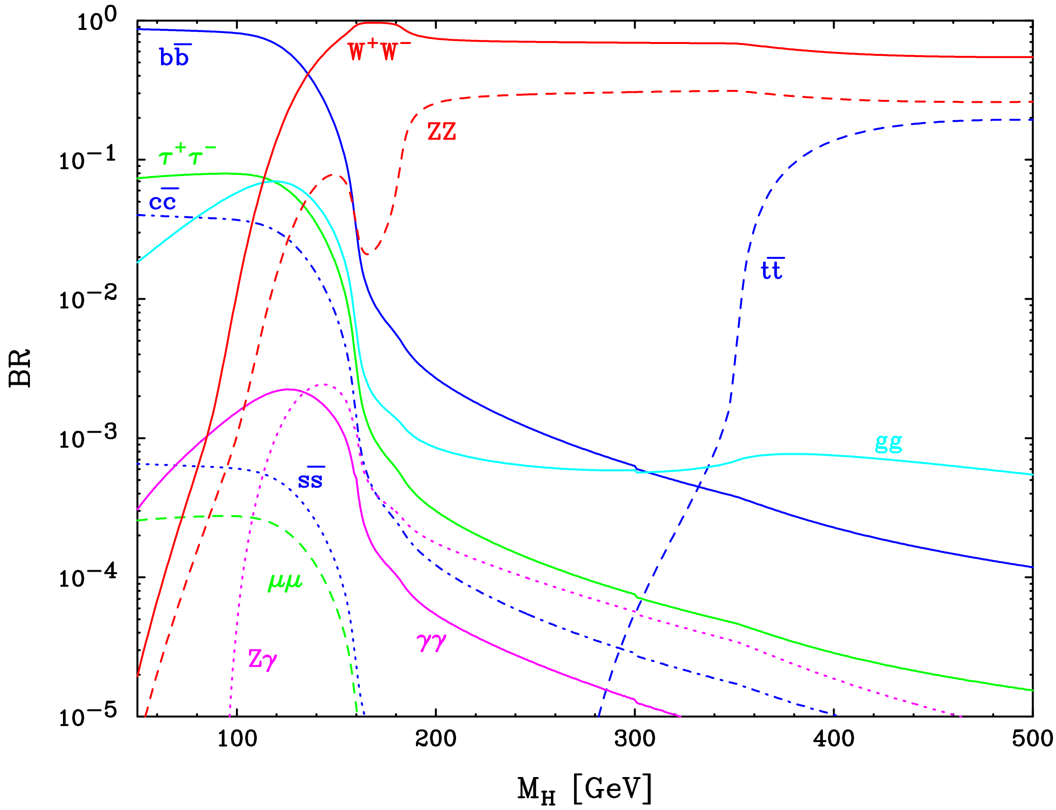

Figure 2.6: Standard Model Higgs boson branching ratios as a function of mass, M_H. The Higgs prefers to decay to the most massive possible final state [9].

particle identification, and an excellent energy and angular resolution are required form the electromagnetic calorimeter system. A complimentary channel in the $t\bar{t}H$ channel, with $H \to b\bar{b}$, leading to two W-bosons and four b-jets in the final state. For trigger purposes one of the $W's$ needs to decay to leptons. A good tagging of the b-jets is required in this mode. Another promising channel, which has been studied recently, is the WBF $qqH \to qq\tau\tau$. The Z+jet production followed by the $Z \to \tau\tau$ decay constitutes the principal background.

Intermediate mass region, $130GeV < M_H < 2M_Z$

The $H \to$ ZZ$^{(*)} \to 4\ \ell$ channel provides a rather clean signature. In addition to the irreducible background from $ZZ^{(*)}$ and $Z\gamma^{(*)}$ continuum production, there are large reducible backgrounds from $t\bar{t}$ and $Zb\bar{b}$ production. The decay mode $H \to ZZ^{(*)}$ is suppressed for

$150 < m_H < 180$ GeV because of the opening of the $H \rightarrow \mathrm{WW}^{(*)}$ channel. Therefore, the $H \rightarrow WW^{(*)} \rightarrow \ell\nu\ell\nu$ channel will help to increase the significance in this mass region, where direct or WBF production gives accessible rates. Due to the decay in ν's no mass peak can be reconstructed and the Higgs boson has to be observed from a excess events above the backgrounds in the transverse mass spectrum. Analysis which explore the WBF topology lead to a better signal-to-background ratio but is much more demanding for the understanding of the detector performance (methods like forward tagging jets and central jet veto has to be exploited).

High mass region, $M_H > 2M_Z$

The $H \rightarrow ZZ \rightarrow 4\ell$ is the most reliable channel for a discovery of the SM Higgs at the LHC. It can be exploited up to a Higgs mass of around 700 GeV. Above this value production cross section becomes too small. The Expected background which is dominated by the continuum production of Z-boson pairs is smaller than the signal. For a very heavy Higgs ($m_H > 500$ GeV), the $H \rightarrow ZZ \rightarrow \ell\ell\nu\nu$ and $H \rightarrow ZZ \rightarrow \ell\nu jj$ can be exploited. Around 25-30% of the production cross-section comes from the WBF channel.

2.11 SM Higgs Parameters

Assuming that a Standard Model Higgs boson has been discovered at the LHC, the potential for the precision measurement of the Higgs parameters (mass, width, production rates, branching ratios) will be the next question. Such measurements should give further insights into the electroweak symmetry-breaking mechanism and into the way Higgs couples to fermions and bosons. We studied $H \rightarrow \mu^+\mu^-$ channel in which we tried to look for Higgs couplings to second generation leptons. In some cases should allow a distinction between a Standard Model and a MSSM Higgs boson.

The Higgs boson width can be experimentally obtained from a measurement of the width of the reconstructed Higgs peak, after unfolding the contribution of the

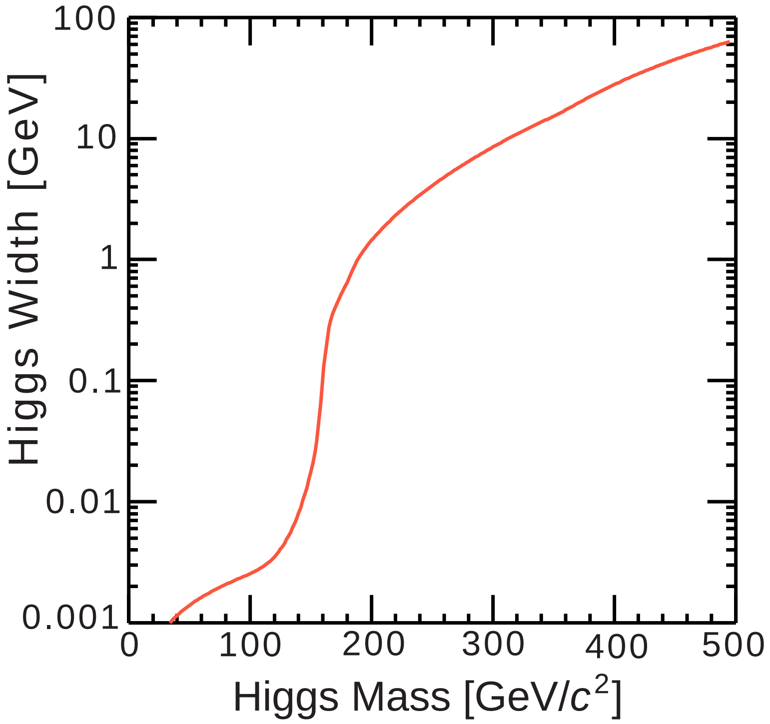

Figure 2.7: Total decay width (in GeV/c^2) of the SM Higgs boson as a function of its mass [10].

detector resolution. Total Higgs width as function of its mass is shown in Fig. 2.7. The measurement of the Higgs boson rate in a given decay channel a measurement of the production cross-section times the decay branching ratio for that channel. If a Standard Model Higgs boson will be observed at the LHC, then ATLAS and CMS should be able to measure its mass with a precision of ≈0.1% and to study its coupling to SM particles with ≈10% precision.

2.12 Extensions of the Standard Model

CP Violation

Matter and antimatter is assumed to be in equal quantities. All current evidence suggest that the universe is made exclusively of matter with little or no antimatter. A process called charge-parity (CP) violation is responsible for the difference between matter and antimatter quantities. CP violation means that the laws of physics change slightly when a particle is replaced by its antiparticle and when all three directions in space are reversed. In direct CP violation, particles and their antiparticles decay in slightly different ways. Standard Model accommodates CP violation through CKM matrix up to some limit. CP violation was first detected in Kaons in 1964, and was also detected in B-mesons at BaBar and Belle experiments. B-meson consists of b or its antiquark along with either of first generation of quarks.

Neutrino Physics

The Standard Model of particle physics assumes that neutrinos are massless, although adding massive neutrinos to the basic framework is not very difficult. Indeed, the experimentally established phenomenon of neutrino oscillation requires neutrinos to have non-zero masses. The strongest upper limit on the masses of neutrinos comes from cosmology: the Big Bang model predicts that there is a fixed ratio between the number of neutrinos and the number of photons in the cosmic microwave background. If the total energy of all three types of neutrinos exceeded an average of 50 electron volts per neutrino, there would be so much mass in the universe that it would collapse. This limit can be circumvented by assuming that the neutrino is unstable, however there are limits within the Standard Model that make this difficult. A much more stringent constraint comes from a careful analysis of cosmological data, such as the Cosmic Microwave Background (CMB), galaxy surveys and the Lyman-alpha forest. These indicate that the sum of the neutrino masses must be less than 0.3 electron volts (Goobar, 2006). In 1998, research results at the Super-Kamiokande neutrino detector determined that neutrinos do indeed flavor oscillate, and therefore have mass. The experiment is only sensitive to the difference in the squares of the masses. These differences are known to be very small, less than 0.05 electron volts (Mohapatra, 2005). Combined, these constraints imply that the heaviest neutrino must be at least 0.05 electron volts, but no more than 0.3 electron volts.

2.13 Beyond the Standard Model

The most common questions still physicists has to answer:-

- Why do we observe matter and almost no antimatter if we believe there is a symmetry between the two in the universe?
- What is this Dark matter that we can't see that has visible gravitational effects in the cosmos?
- What is the mechanism to generate mass for Standard Model particles?
- Are quarks and leptons actually fundamental, or made up of even more fundamental particles?
- Why are there exactly three generations of quarks and leptons? How does gravity fit into all of this?

Following are the different approaches trying to solve the underlying mystery.

2.13.1 Grand Unified Theory

The theory which will unify the strong, weak, and electromagnetic interactions is called the Grand Unified Theory. Physicists can purpose many such theories but more data is needed to tell which version of them describes the real nature. If a Grand Unification of all the interactions is possible then all the interactions we observe are all different aspect of the same unified interaction. However, how can this be the case if strong and weak and electromagnetic interactions are so different in strength and effect? Strangely enough, current theories suggest that these varied forces merge into one force when the particles being affected at very high energy. Contemporary work on GUT also suggests new force-carrier particles that could cause the proton to decay although such decays are rare. Measurement tells us the lifetime of the proton is greater than 10^{32} years.

2.13.2 Supersymmetry

In Supersymmetry or 'SUSY' [11], for each SM particle a supersymmetric partner is introduced having same quantum numbers as the particles but their spin differs by one half. It cancels the quadratic divergence in the Higgs boson mass, thus solving the fine tuning problem, provided the masses of the supersymmetric partners are not beyond 1 TeV scale. To incorporate supersymmetry into particle physics, the Standard Model must be extended to include at least twice as many particles, since there is no way that any of the particles in the Standard Model can be superchargers of each other. The simplest possible supersymmetric model consistent with the Standard Model is the minimal supersymmetric Standard Model (MSSM) [12], which is minimal in the sense that a minimal number, i.e. two, of the Higgs doublets is introduced. The MSSM implies five observable Higgs particles, two neutral CP-even scalars, a light h and a heavy H, a CP-odd A, and charged Higgs H^+ and the H^-. However, the MSSM appears to be unnatural in a number of ways, and many physicists doubt that it will be the correct theory. A possibility in supersymmetry is the existence of very heavy stable particles such as neutralinos which would be weakly interacting massive particles (WIMPs) and could be candidates for the dark matter.

2.13.3 String Theory

Another major effort in theoretical particle physics is string theory. String theorists attempt to construct a unified description of quantum mechanics and general relativity by building a theory based on small strings and branes rather than particles. String theory is a model of fundamental physics whose building blocks are one-dimensional extended objects (strings) rather than the zero-dimensional points (particles) that are the basis of the Standard Model of particle physics. For this reason, string theories are able to avoid problems associated with the presence of point like particles in a physical theory. Studies of string theories have revealed that they require not just strings, but also higherdimensional objects.

2.14 And if all this is not true

The Standard Model describes the phenomena of physics starting from our everyday electromagnetic interactions down to the scale of strong and weak interactions which have been probed up to energies of 200 GeV. Electromagnetic interactions govern the physical phenomena down to the distances of an atom (10^{-10} m). Then, the strong interaction takes over to hold the protons and neutrons in an atomic nucleus (10^{-14} m) and to keep the quarks in protons and neutrons (10^{-15} m) together. Further down the distance scale (10^{-19} m), the effects of the $W^{\pm}$ and Z^0 vector bosons which are the carriers of the weak interaction become important. This is where we are now. With the LHC we can hope to gain one more scale in the distance ladder, arriving to energies of the order of TeV, and hopefully discovering the origins of the SSB of the electroweak interactions. At much smaller distances - or at much higher energies - we finally arrive to the Planck scale (10^{19} GeV) where the quantum gravity should become comparable and unified to other forces. The Standard Model, however, does not include the description of gravitational force.

The Standard Model combines the color forces and the unified electroweak force which is often notated by $SU(3)_c \times SU(2)_L \times U(1)_Y$. The $SU(3)_c$ of QCD, however, is not included in an unified form. One would like to find a grand unified symmetry group which could contain the electroweak group and the color group. The unification scale M_x can be estimated from the evolution of the running coupling constants of the interactions: the three coupling constants coincide almost at $M_x \approx 10^{15}$ GeV. The symmetry of the unified forces is broken at this value by some mechanism. The Standard Model does not provide a mechanism for this unification. The Standard Model does not provide a mechanism for this unification.

Furthermore, if the Standard Model were to be valid up to this very large mass scale, which are caused by radiative corrections. This is the so called naturalness or hierarchy problem, credible fine-tuning is needed up to the lighted mass scales to keep the Higgs boson mass small. To solve the naturalness problem, one can introduce a new symmetry between bosons and fermions called as SUSY and introduce sparticles that exactly and naturally cancel the divergences. At least two Higgs doublets are required resulting in five observable Higgs particles.

2.15 Summary

The experimental data for testing the Standard Model has achieved an impressive accuracy. In the meantime, many theoretical contributions have become available to improve and stabilize the Standard Model predictions and to reach at some better theoretical accuracy. The Higgs particle is the missing piece in the Standard Model, required to complete the picture of particle physics. Therefore the search for this particle is at the forefront of present and proposed research programmes in the High Energy Physics. A comprehensive search for this particle up to the predicted mass limit of ~ 1 TeV will be possible at the LHC, which is on the verge of its completion. Hopefully the LHC will discover this particle and complete the picture of the Standard Model. If Higgs bosons are not discovered at the TeV scale, the LHC will be in a position to test alternative theories of electroweak symmetry breaking or supersymmetric extensions of Standard Model.

Bibliography

[1] S. L. Glashow, Nucl. Phys. 22 (1961), 579;
S. Weinberg, Phys. Rev. Lett. 19 (1967), 1264;
A. Salam in *Elementary Particle Theory*, Nobel Symp. N. 8, ed. by N. Svartholm, Aspenäsgården, Stockholm (1968), 367.

[2] P. Higgs: Phys. Lett. 12 (1964) 132;
Phys. Rev. Lett. 13 (1964) 508; Phys. Rev. 1156 (1966) 145;
F. Englert and R. Brout: Phys. Rev. Lett. 13 (1964) 321;
G. S. Guralnik, C. R. Hagen and T. W. Kibble: Phys. Rev. Lett 13 (1964) 585.

[3] M. Herrero, The Standard Model, hep-ph/9812242;
W. Buchmüller and C. Lüdeling, Field Theory and Standard Model, hep-ph/0609174;
S. F. Novaes, Standard Model: An Introduction, hep-ph/0001283;
W. Hollik, Standard Model Theory, hep-ph/9811313.

[4] U. Egede, The search for a Standard Model Higgs at the LHC and electron identification using transition radiation in the ATLAS tracker, ISBN 91-628-2804-5 LUNFD6/(NFFL-7150) 1997, http://www.hep.lu.se/atlas/thesis/egede/.

[5] G. Abbiendi, et al. (the ALEPH Collaboration, the DELPHI Collaboration, the L3 Collaboration and the OPAL Collaboration, The LEP Working Group for Higgs Boson Searches), Phys. Lett. B 565 (2003) 61, hep-ex/0306033.

[6] C. D. Froggatt, Surveys High Energ. Phys. 18 (2003) 77, hep-ph/0307138.

[7] C. Quigg, Acta Phys. Polon. B 30 (1999) 2145, hep-ph/9905369.

[8] LEP Electroweak Working Group, http://lepewwg.web.cern.ch.

[9] A. Djouadi, J. Kalinowski and M. Spira, Comput. Phys. Commun. 108, 56 (1998).

[10] G. L. Bayatian, A. Kumar, S. B. Beri, J. M. Kohli et al. (The CMS Collaboration), J. Phys. G: Nucl. Part. Phys. 34 (2007) 995-1579.

[11] P. Fayet and S. Ferrara: Phys. Rep. 32 (1977) 249;
H. P. Nilles: Phys. Rep. 110 (1984) 1;
H. Haber and G. Kane: Phys. Rep. 117 (1985) 75;
S. Martin: hep-ph/9709356 (1997).

[12] H. P. Nilles: Phys. Rep. 110 (1984) 1;
S. Dawson: hep-ph/9712464 (1997).

Chapter 3

The LHC and CMS Detector

High energy particle physics is a lifestyle where the mundane and the marvelous meet. When everything is working well, particles and antiparticles collide with nearly the speed of light and so recreate conditions similar to the fraction of second after the big bang. At this moment, discoveries that revolutionize human understanding of the subatomic world can happen to large extent.

3.1 Large Hadron Collider

The Large Hadron Collider (LHC) and its experiments will enhance our understanding of the last unsolved issue in the Standard Model, that of the mechanism via which the underlying Electroweak Symmetry is broken, resulting in two visible forces, the weak interaction and electromagnetism, which are different at low energy scales. In doing so, the LHC experiments may well uncover fundamental new physics, with wide-ranging implications in the understanding of the universe. The 26.7 km long ring tunnel, as shown in Fig. 3.1, lined with concrete and lying in the limestone strata for about 10% of its length and in the molasse for about 90% buried around 50 to 175 m underground. It straddles the Swiss and French borders on the outskirts of Geneva. A luminosity of 10^{34} cm^{-2} sec^{-1} will produce on average 19 collisions in one single bunch crossing for nominal LHC operation [1]. The LHC will provide protons accelerated in bunches with bunch spacing of 25 ns and the collision rate of 40 MHz. The counter rotating beams of protons used will have an energy of 7 TeV each with center of mass energy $\sqrt{s} = 14$ TeV. Heavy ions are also accelerated for some experiments with bunch spacing of 125 ns and center of mass energy 1150 TeV. The first *pp* collision is expected in mid 2008.

The LHC consists of two interleaved synchrotron rings, 26.7 km in circumference. The main elements of the rings are 2-in-1 superconducting dipole and quadrupole magnets interleaved to focus the beams operating in superfluid helium at 1.9 K. The total number of cryogenic magnet assemblies - or cryogenics - includes 1232 dipoles with correctors, 360 short straight sections (SSS) for the arcs with quadrupoles and integrated high-order poles, and 114 special SSS for the insertion regions (IR-SSS) with magnets for matching and dispersion suppression [2]. The construction of these magnets is a major technological challenge, since a flux density of more than 8 Tesla has to be achieved. In brief,

- High energy beams move around the LHC ring inside a continuous vacuum guided by superconducting magnets.
- The superconducting magnets are cooled by a huge cryogenics system. The cables conduct current without resistance in their superconducting state.
- The beams will be stored at high energy for hours. During this time, collisions take place inside the main LHC experiments.

Prior to being injected into the main accelerator, the particles are prepared through a series of systems that successively drive up the particle energy levels. The LHC relies on a chain of particle accelerators, the oldest of which was constructed in the 1950s. The acceleration chain starts with the Linear Accelerator (LINAC) accelerating protons to an energies of 50 MeV. The particles are then injected in to Proton Synchrotron Booster (PSB) for energies up to 1.4 GeV and later into the Proton Synchrotron Ring (PSR) to have 26 GeV. Finally the Super Proton Synchrotron (SPS) can be used to increase the energy of protons up to 450 GeV and injects them into the LHC ring where

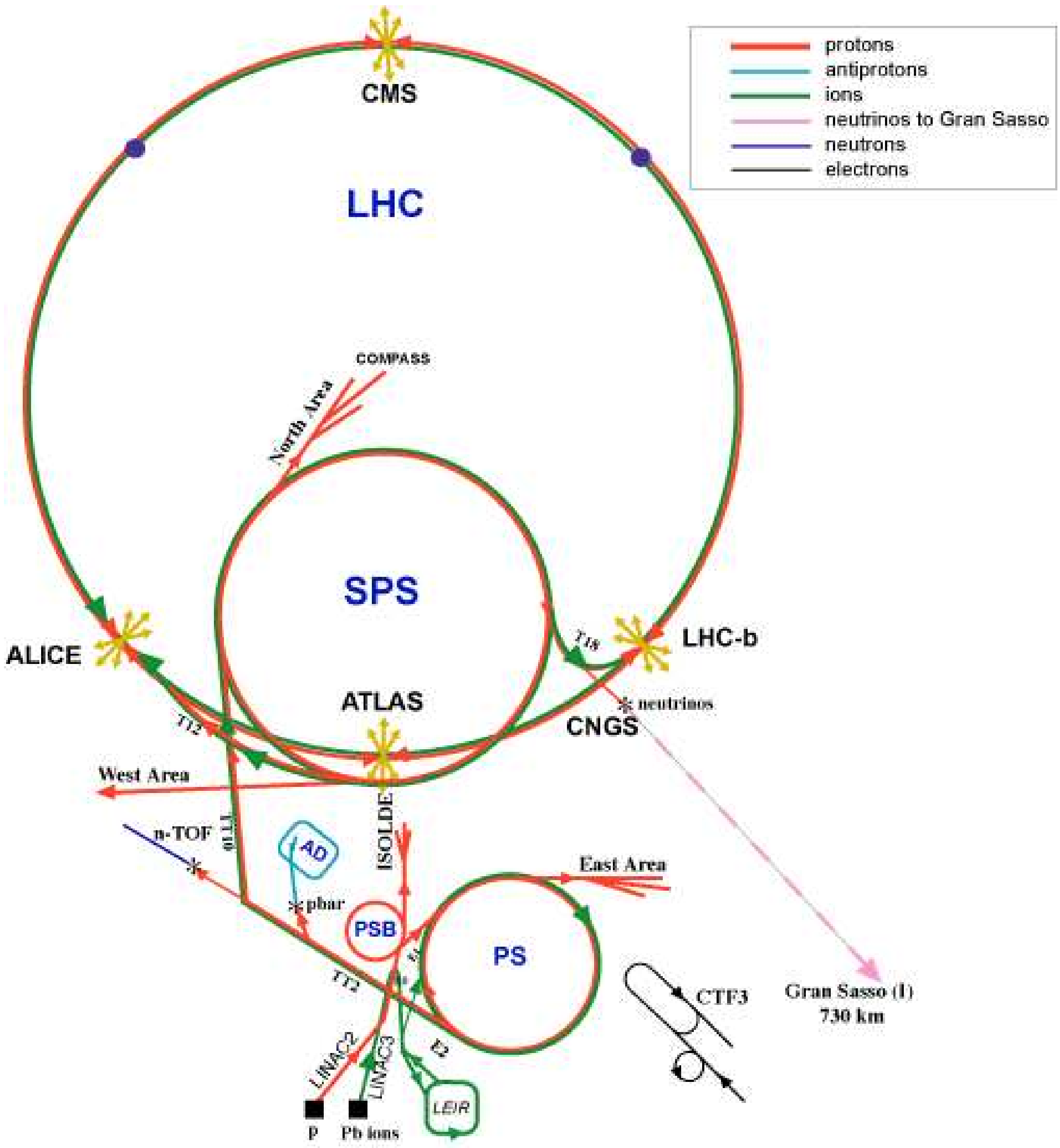

Figure 3.1: The Large Hadron Collider (LHC).

the energy of the protons will touch 7 TeV scale as shown in Fig.3.1.

The total amount of time taken by the injection system to fill the LHC accelerator is estimated to be approximately 16 minutes. The minimal time required for ramping up the LHC magnets from 450 GeV to the collision energy of 7 TeV is approximately 20 minutes. The same amount of time is required to ramp the magnets down after the beam stop. The total LHC turnaround time can therefore be estimated to be approximately 70 minutes. The integrated luminosity per run can be then calculated using the following relation:

$$L_{int/run} = L_0 \tau_L [1 - e^{-T_{run}/\tau_L}],$$

where T_{run} is the total length of the luminosity run, L_0 is the peak luminosity value and τ_L is the luminosity lifetime. Assuming that the machine can be operated 200 days a year, the total integrated luminosity between 80 and 120 fb^{-1} can be achieved, depending on the actual turnaround time.

3.2 Experiments at LHC

Five experiments will be built to utilize the LHC energy. Two of them, **ATLAS** (A Toroidal LHC ApparatuS) and **CMS** (Compact Muon Solenoid) designed to work at the peak luminosities of the order of 100 fb^{-1}. The main goals of these experiments is the exploration of the limits of the Standard Model in the searches of Standard Model and supersymmetric Higgs bosons, supersymmetric partners related to Standard Model particles and high precision level study of Top and Beauty physics. Other special purpose experiments, **LHCb** is designed for B-physics, **ALICE** (A Large Ion Collider Experiment) will study matter at extremely high energy densities in Lead-Lead collisions having energy up to 1150 TeV, which may produce a quark gluon plasma (QGP), and **TOTEM** (Total Cross Section, Elastic Scattering and Diffraction Dissociation) is located on the both sides of the CMS detector, close to LHC beam axis, and is designed for elastic low-angle scattering of protons.

3.3 Compact Muon Solenoid

The LHC will address one of the main questions in the particle physics today i.e. the origin of the spontaneous symmetry breaking in the electroweak sector of the Standard Model. The observable consequence could be a scalar particle, the Higgs boson, or if the Standard Model is not the complete description of nature, it may also include a variety of new particles like several Higgs bosons, supersymmetric particles, new gauge bosons, technicolor states or leptoquarks. The Compact Muon Solenoid (CMS) experiment is designed to enable the discovery and investigation of all possibilities, the Higgs sector is one of them. The CMS is one of the detectors that will be installed at 'SX5' point of the LHC tunnel. It is a 12,500 ton detector with over 10 million electronic channels, not including the 65 million pixel detector channels - in brief, a technological marvel which is expected to break new ground in Particle Physics.

The CMS detector has been designed to detect cleanly the diverse signatures of new physics at the LHC. The majority of proton-proton collisions are due to soft reactions between the proton constituents, the quarks and gluons. Many processes associated with new physics are expected to be due to very high-energy collisions between constituents and to occur infrequently. According to current theoretical models, the new particles produced in such interactions decay to energetic, mostly already known particles. Their properties can be studied by experiments at CMS. It will do so by identifying and precisely measuring muons, electrons and photons over a large energy range, by determining the signatures of quarks and gluons through the measurement of jets of charged and neutral particles (hadrons) with moderate precision, and by measuring missing transverse energy flow, which will enable the signatures of non-interacting new particles as well as neutrinos to be identified.

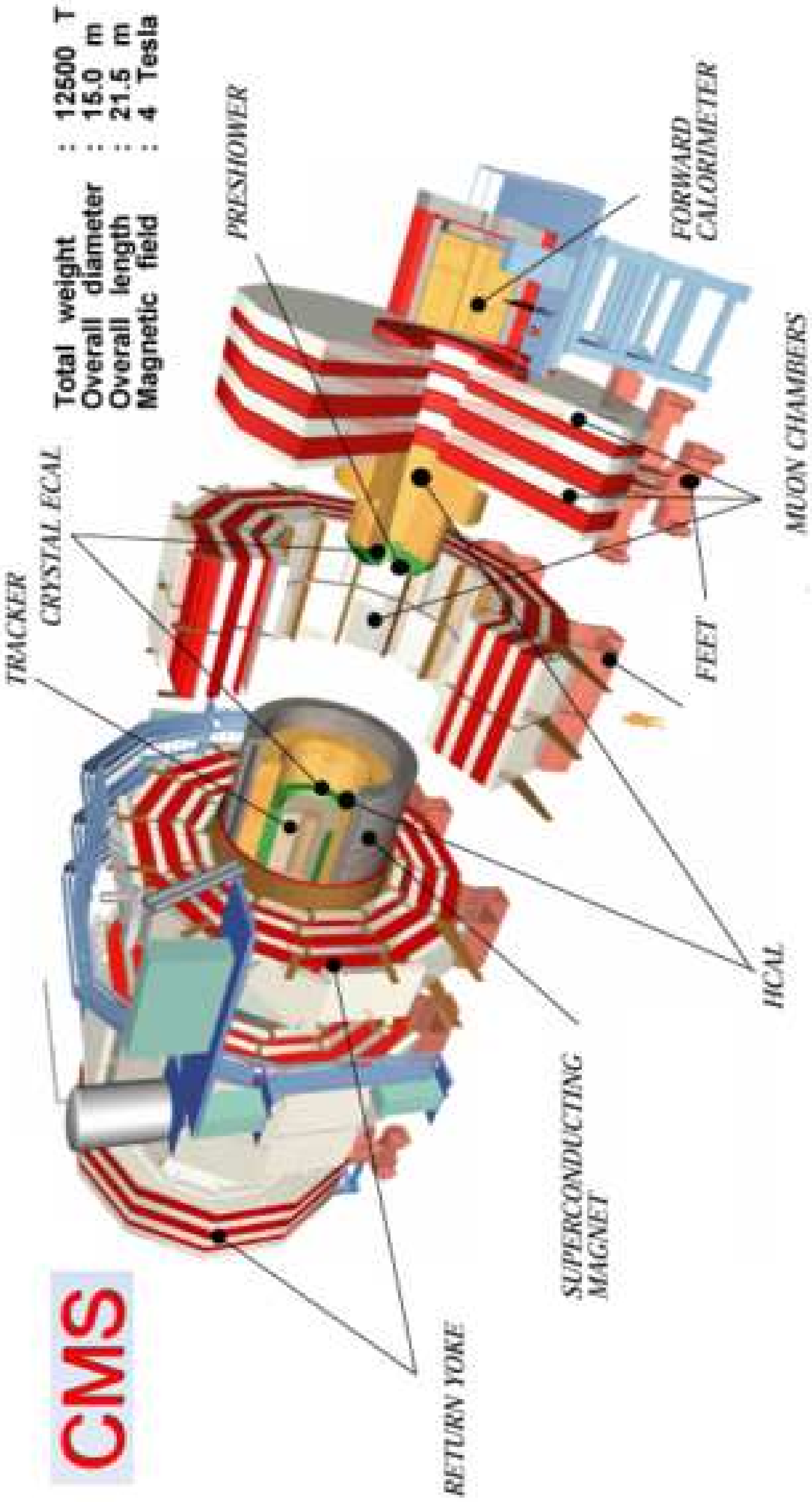

Figure 3.2: The set up of the CMS detector (HCAL=hadron calorimeter, ECAL=electromagnetic calorimeter).

3.4 Overview of Detector Elements

The CMS detector will identify particles and measure their energies and momenta. No single device is capable to fulfill this goal by itself, therefore a complex apparatus of several subsystems has been designed. The interaction point or main vertex is located at the center of CMS. Fig. 3.2 shows that subdetectors are arranged in an onion-like structure in the CMS detectors. It consists of a precise and compact muon spectrometer having 5 rings or wheels and 2 endcap disks of muon absorber and muon tracking chambers with a stand-alone resolution of $\delta p_{\perp}/p_{\perp} \approx 10\%$ at 10 GeV, a sampling brass hadron calorimeter, a electromagnetic lead-tungstate ($PbWO_4$) crystal calorimeter with $\delta E/E < 1\%$ for E > 30 GeV, a superconducting coil that provides a solenoidal 4 Tesla magnetic field for momentum measurements, a full silicon inner tracker with embedded precision vertex detector and detectors for the forward regions close to the beam axis of the accelerator. CMS includes CASTOR [3] calorimeter and two zero degree calorimeters (ZDCs) [4]. The CASTOR detector will extend the acceptance out to very large rapidity up to $|\eta| = 7$.

3.4.1 Silicon Tracker

The tracker is the first system that a particle coming from the interaction point traverses. It determines trajectories of charged particles, which are curved by the magnetic field. The primary purpose of the CMS tracking system [5] is to determine the momenta of charged particles as they spiral in the 4 Tesla magnetic field by accurately measuring their trajectories as they cross layers of silicon microstrip and pixel detectors. The CMS tracking system is designed to reconstruct high p_T muons, isolated electrons and hadrons with high momentum resolution. It will be the largest silicon detector ever built as shown in Fig. 3.3. It contains many technical novelties, in the sensors, electronics, mechanics and cooling system. It also helps in the identification of tracks coming from detached vertices which arise from decays of b quarks which provide useful signatures for new physics.

The tracker occupies a cylindrical volume of 2.4 m diameter and 5.4 m length.

Figure 3.3: Transverse view of CMS Silicon tracker.

It consists of two basic parts, the pixel detector and the inner tracker, Muon chambers serves as the outer tracker. Both are made of silicon and thus operate as ionization detectors. The pixel detector occupies the innermost region, close to the interaction point. It provides high resolution, three-dimensional patterns of space points by means of silicon pads called pixels. Its main purpose is to identify the primary vertex and the secondary vertices, which may arise from the decay of heavy, relatively long-lived particles such as hadrons containing b-quarks. Such particles typically have a flight path of a few 100 μm before they decay. The pixel system also complements the track finding in the inner tracker by providing additional space points. The barrel pixel detector consists of three layers 4 cm , 7 cm and 11 cm radius, respectively. The forward pixel detector is made up of two pairs of layers ± 34 cm and ± 46 cm from the interaction point in the beam direction.

In total the CMS tracker implements 25,000 silicon strip sensors covering an area of 210 m^2. Connected to 75,000 Analogue Pipeline Voltage (APV) intrinsically radiation hard readout chips built in 0.25 μm CMOS technology, one has to control 9,600,000 electronic readout channels, needing about 26 million microbonds. At the smallest radii from the beam line at 4 and 7 cm at low luminosity and at 7 and 11 cm at high luminosity the interaction region is surrounded by two barrel layers of Silicon pixel detectors. Two endcap disks cover radii from 6 cm to 15 cm. Due to the harsh radiation environment and low-noise requirement, the tracker will be operated at a temperature of -10^0C.

3.4.2 Electromagnetic Calorimeter

The electromagnetic calorimeter (ECAL) measures total energy of electrons (e^-), positrons (e^+), and photons. High energy electrons and photons interact with the matter mainly through bremsstrahlung and electron-positron pair production, depositing practically all their energy in an adequately designed calorimeter. These particles produce showers of e^+/e^- pairs in the material. The number of final e-pairs is proportional to the energy of the initiating particle. It consists of 75,000 lead-tungstate ($PbWO_4$) scintillating crystals [6] equipped with vacuum phototriodes and associated electronics which enhances the energy measurement of electrons and photons with high precision. It is composed of a barrel and two end caps. The crystals in the barrel are grouped in 36 supermodules, each divided in 4 modules. The crystal shape varies with η, in particular, there are 17 different types of crystals and for each of them there is a right and left handed version. The $PbWO_4$ was chosen because it is fast and has a short radiation length and a small Moliere radius. Nevertheless, its intrinsic light yield is relatively low, about 100 photons/MeV at 18^{o}C. This fact along with the presence of a very intense magnetic field inside the barrel led to the choice of Avalanche Photodiodes (APDs) as photodetectors. Two APDs, coupled in a capsule, are glued on the teat face of each crystal, five capsules are read out by the same very front end (VFE) board. The VFEs are connected, in groups of five, to the front end (FE) boards, the cards designed to process and store the digitized data while waiting for the trigger decision. The data are transferred to the off-detector electronics via optical fibers.

3.4.3 Hadron Calorimeter

The CMS scintillator tile-fiber hadron calorimeter (HCAL) is required for the discovery potential of Higgs between masses of 100 to 800 GeV. SUSY searches also require hadron calorimeter. In one year of running, with luminosity of 10^{33} cm^{-2} sec^{-1}, various mass limits of supersymmetric particles can extended to about 2 TeV. In addition, the non SUSY dark matter searches require the HCAL to trigger on large missing energy events. Jet physics is not possible without the HCAL. In addition for determining quark, gluon and neutrino directions and energies by measuring the energy and direction of particle jets and of the missing transverse energy flow, HCAL can be used, in conjunction with ECAL and the muon system, for identifying electrons, photons and muons. It is the goal of the CMS experiment to have a working and calibrated hadron calorimeter on the first day of data taking.

Hadrons such as protons, neutrons, pions or kaons are strongly interacting particles, which feel the force that binds nuclei together. Like for electrons or photons, their energy and position can be measured in a calorimeter. Hadronic showers start to develop later and have larger longitudinal and lateral dimensions than ECAL ones. Therefore the hadron calorimeter (HCAL) is thicker than the ECAL, which it surrounds. The hadron barrel (HB) [1] and hadron endcap (HE) calorimeters are sampling calorimeters with absorber and structural elements which are made of cartridge brass (70% Cu and 30% Zn) [8], which is easy to machine, and stainless steel plates, respectively. The active sampling elements are 3.7 mm thick plastic scintillator tiles with wavelength shifting (WLS) fiber readout. HB as shown in Fig. 3.4 covers the η range $0 < |\eta| < 1.3$ and extends radially between r = 1.806 and r = 2.95 meters, while the HCAL endcaps (HE) cover the pseudorapidity range $1.3 < |\eta| < 3.0$. Pseudorapidity coverage is extended up to $\eta = 5$ with two forward calorimeters (HF) [9], made up of steel absorber plates, surround the beam pipe 11 m from the interaction point as shown in Fig. 3.5.

Figure 3.4: Assembled hadron barral (HB) before final installation in to the CMS detector.

Outer Hadron Calorimeter

The outer hadron calorimeter (HO) consists of layers of scintillator tiles (40 cm $\times$ 40 cm) outside HB. Scintillation light is transferred to the readout system using a combination of wave length shifting (WLS) fibers and clear fibers through circular grooves in the scintillator tile. The HO is designed specifically to sample the tails of hadronic showers, in particular for those showers which develop deep inside the calorimeter, to improve the missing E_T resolution and also to achieve the design energy resolution of $(\frac{80-90}{\sqrt{E}} \pm 5)\%$. It ensures the complete energy absorption for high energy hadronic showers. The details of HO are discussed in chapter 4 and is one of the main work of present thesis.

Figure 3.5: Hadron forward detector wedges with quartz fibers as sensitive detectors .

3.4.4 Superconducting Magnet

Electromagnetic forces make the charged particles to travel along a curved path. Radius of curvature and direction indicate the momentum of particle and the sign of the charge (positive or negative). The momentum measurement of charged particles in the detector is based on the bending of their trajectories. High momentum resolution is achievable either through a large bending power or through a very high precision on the spatial resolution and alignment of the detectors. For a similar bending power, the overall size of a solenoidal system [10] is smaller than that of a toroid. The CMS design is thus based on a solenoid providing a very high 4 Tesla magnetic field. The CMS magnet system consists of a superconducting coil, the magnet yoke (barrel and endcap), a vacuum tank and ancillaries such as cryogenics, power supplies and process controls. The main parameters are magnetic field of 4 Tesla, a yoke diameter of 14 m across flats, an axial yoke length including endcaps of 21.6 m and a total weight of about 12,000 tons. It will be the largest superconducting magnet system in the world, the energy stored into it, if liberated, will be large enough to melt 18 tons of gold. As 2007 draws to a close, some 80% of the LHC's magnets, the main components of the new machine, were installed underground and a complete sector of the machine was being prepared for cool-down to its operating temperature of just 1.9 degrees above absolute zero, colder than outer space.

3.4.5 Muon Chambers

Muon detection is of central importance for the Higgs boson searches in the golden discovery channel $H \rightarrow ZZ^{(*)} \rightarrow 4\ell^{\pm}$ where at least two of the leptons are muons. This channel covers most of the Higgs mass range. Possible extensions of the Standard Model provide signatures like new heavy gauge boson $W^{'}$ and $Z^{'}$ decaying in muon and neutrino or two muons. In the supersymmetric extension of the Standard Model, Higgs boson may decay in cascades including several muons. The decay of supersymmetric Higgs bosons into tau leptons can be explored following the muon from the tau decay.

The tasks of the muon system are identification, triggering and momentum measurements of the muons. The choice of the solenoidal magnet and sufficient amount of material in front of the muon system allows muon identification even at highest luminosities. The muon trigger efficiency does not depend on the hadronic activity. Precise momentum measurement is achieved by several points that define the muon track. Only muons and neutrinos traverse the entire detector and get this far. This chamber detects muons, but neutrinos escape without leaving a trace. The presence of neutrinos is inferred by missing energy. Muon system helps in the identification of muons and provide, in association with the tracker, a precise measurement of their momentum. The muon detectors, placed behind the calorimeters and the coil, consist of four muon stations interleaved with the iron return yoke plates as shown in Fig. 3.6 [11]. They are arranged in concentric cylinders around the beam line in the barrel region, and in disks perpendicular to the beam line in the endcaps.

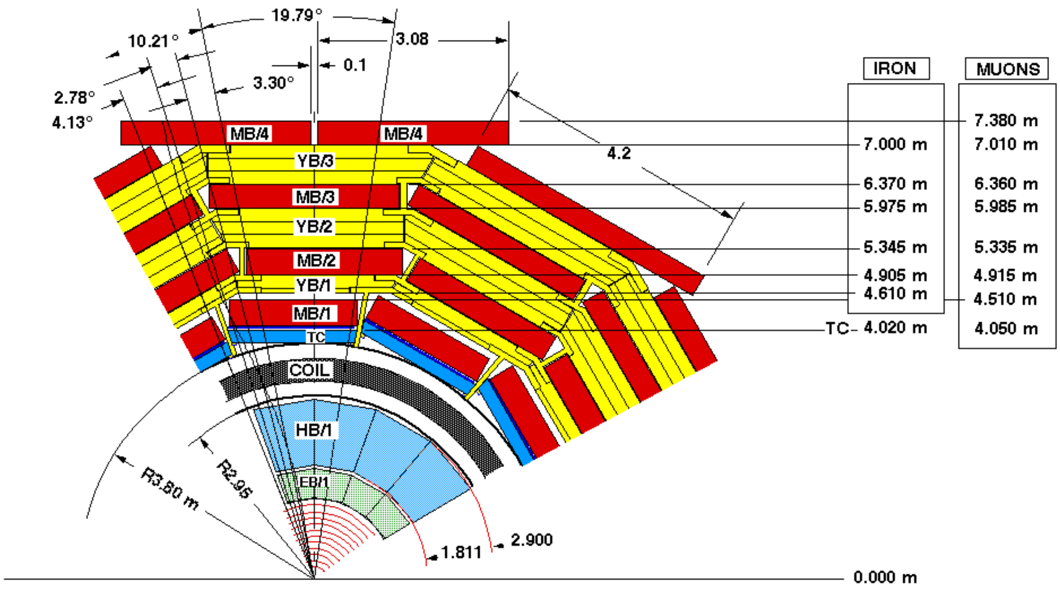

Figure 3.6: Transverse view of the CMS detector, showing clearly the positions of muon chambers and Iron yolks from the central collision point.

CMS will use three types of gaseous particle detectors for muon identification, Drift Tubes (DT) consists of tubes containing wires in the central barrel region, Cathode Strip Chambers (CSC) are Multiwire Proportional Chambers placed in the endcap region and Resistive Parallel Plate Chambers (RPC) in both the barrel and endcaps. The DT and CSC detectors are used to obtain a precise measurement of the position and its bending angle and thus the momentum of the muons. From these segments the precise transverse momentum and the charge of a track can be reconstructed off-line. The RPC's are dedicated trigger chambers, which determines a muon candidate's approximate transverse momentum and the bunch crossing number from which it originated due to excellent timing resolution of 2 and 3 ns.

3.5 Physics Requirements of CMS Detector

The detection and study of new physics at the CMS will rely on good identification of leptons, photons and jets and precise measurement of their momenta and energies. The particle types that needed to be identified in the CMS above listed subdetectors are electrons, photons, hadrons, muons, neutrinos and their supersymmetric partners. Electrons and photons deposit most of their energy in the electromagnetic calorimeter. Due to their charge, electrons produce a trajectory in the tracker whereas the electrically neutral photons do not. Strongly interacting charged or neutral hadrons deposit energy in both electromagnetic and hadron calorimeters. Muons traverse the entire apparatus, but leave little energy in the calorimeters. They can be identified due to signals in the muons chamber planes in the iron yoke as shown in the Fig. 3.7. Neutrinos, and their supersymmteric partners called as neutralinos, can only be observed indirectly because they interact very weakly with the detector . Their presence can be deduced if the so called missing energy differs from zero. It is given by the vector sum of the transverse energy depositions in the calorimeter cells.

The fundamental physics goal of the CMS detector is then to uncover and explore the physics behind electroweak symmetry breaking. This involves the following specific challenges:

- Discover the Standard Model Higgs and/or the multiple Higgs bosons of supersymmetry.

- Discover supersymmetry over the entire theoretically allowed mass range up to a

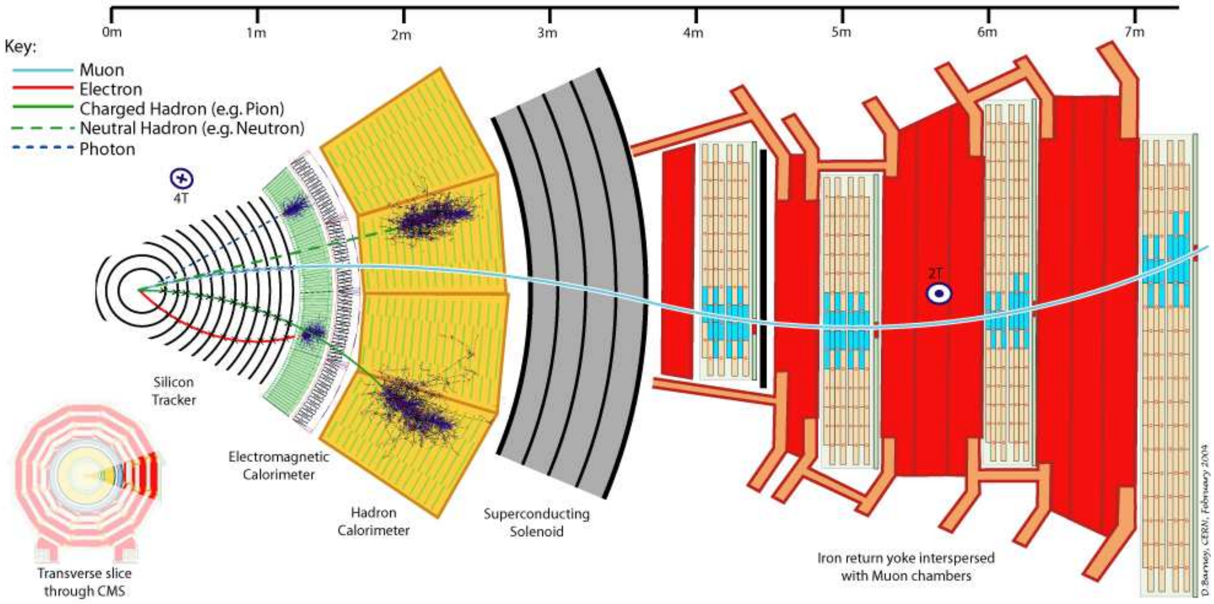

Figure 3.7: Slice through CMS showing particles incident on the different sub-detectors.

few TeV.

- Discover new dynamics at the electroweak scale.

The energy range opened up by the LHC allows us to search for other, perhaps less well motivated objects:

- Discover any new electroweak gauge bosons with masses below several TeV.
- Discover any new quarks or leptons that are kinetimatically accessible.
- Discover extra-dimensions for which the appropriate mass scale is below several TeV.

CMS will have the possibility of exploiting the enormous production rates for Standard Model processes for conducting following studies such as:

- Study the production and decay properties of the top quark and set limits on possible exotic decays.

- Study of b-physics, particularly that of B-baryons and B_s-mesons.

CMS must also have the capability to find the totally unexpected. We can be sure, though, that new phenomena of whatever type will decay into the particles of the Standard Model. The varied physics signatures of these processes require that CMS be able to reconstruct and measure final states involving the following:

- Charged leptons like electrons, muons and taus (via its hadronic decays).
- Jets of energy up to several TeV coming from the production at high transverse momentum of quarks and gluons.
- Jets coming from b-quarks.
- Missing transverse energy (E_T^{miss}) carried off by weakly interacting neutral particles such as neutrinos.
- The electroweak gauge bosons like photons, and $W^{\pm}$ and Z^0 bosons (in both their dijet and lepton plus missing transverse energy modes).

3.6 Summary

The $SU(3)_c \times SU(2)_L \times U(1)_Y$ gauge interactions of the Standard Model provide an elegant and a tremendously successful description of existing data, but they give no explanation of the origin of particle masses. The internal consistency of the Standard Model requires that at least part of the explanation of masses, the origin of electroweak symmetry breaking, must be found at the TeV scale. The LHC under final construction days at CERN, Geneva combines the two most important virtues for high energy physics experiments. It will provide proton-proton collisions at the highest center-of-mass energy of 14 TeV and large luminosities in the range from in the initial phase 10^{33} cm^{-2} sec^{-1} up to 10^{34} cm^{-2} sec^{-1} at a later stage. The CMS detector at LHC is optimized for physics with high energy as well as high luminosity proton-proton collisions. The main design goals of CMS are precision muon measurements up to the highest energies available, the best possible electromagnetic calorimetry, high quality central tracking and hermetic calorimetry. The hermeticity of CMS is an advantage for studies of ultra-peripheral collisions relative to other experiments at the LHC. The largest possible rapidity is important for reducing backgrounds. The detailed simulation studies carried out by CMS collaboration [12] enable one to make the following statements with a high degree of confidence:

- If the minimal Standard Model is correct and the Higgs boson is not discovered previously, it will be found at LHC.
- If supersymmtery is relevant to the breaking of electroweak symmetry, it will be discovered at LHC and many details of the particular supersymmetric model will be distangled.
- If the Higgs sector is that of the minimal supersymmteric model, at least one of the Higgs decay channel will be seen, no matter what the parameters turn out to be. In many cases, several Higgs bosons or decay channels will be seen.
- If the electroweak symmetry breaking proceeds via some new strong interactions, many resonances and new exotic particles will certainly be observed.
- New gauge bosons with masses less than several TeV will be discovered or ruled out.
- Signals for extra-dimensions will be revealed if the relevant scale is in the TeV range.

The LHC represents a great opportunity and promise of vast excitement not only for the collaborators on the LHC experiment but whole field of particle physics.

Bibliography

[1] The LHC Main Ring, CERN-2004-003
http://ab-div.web.cern.ch/ab-div/Publications/LHC-DesignReport.html.

[2] LHC magnet tests: the Indian Connection, CERN Courier, p19 (June 2007).

2000-016.

[3] A. L. S. Anglis and A.D. Panagiotou, J. Phys. G. 23 18 (1997).

[4] C. Adler et al., Nucl. Inst. and Methods A470, 488 (2001).

[5] CMS Tracker Technical Design Report, CERN/LHCC 98-6,
Addendum to CMS Tracker Technical Design Report, CERN/LHCC

[6] CMS Electromagnetic Calorimeter Technical Design Report, CERN/LHCC 97-33.

[7] S. Abdullin, A. Kumar, S. B. Beri, J. M. Kohli et al., Design, Performance, and Calibration of CMS Hadron-Barrel Calorimeter Wedges, CMS NOTE 2006/138.

[8] CMS Hadron Calorimeter Technical Design Report, CERN/LHCC 97-31.

[9] S. Abdullin, A. Kumar, S. B. Beri, J. M. Kohli et al., Design, Performance, and Calibration of CMS Forward Calorimeter Wedges, CMS NOTE 2006/044.

[10] CMS Magnet Technical Design Report, CERN/LHCC 97-10.

[11] CMS Muon Technical Design Report, CERN/LHCC 97-32.

[12] G. L. Bayatian, A. Kumar, S. B. Beri, J. M. Kohli et al. (The CMS Collaboration), J. Phys. G: Nucl. Part. Phys. 34 (2007) 995-1579.

Chapter 4

CMS Outer Hadron Calorimeter

The CMS hadron calorimeter (HCAL) consists of four parts. These are the inner barrel calorimeter (HB), located inside the magnet covering the central rapidity region of up to $|\eta| \leq 1.4$, endcap calorimeters (HE), for $1.4 < |\eta| < 3.0$, and forward calorimeters (HF) for $3.0 < |\eta| < 5.0$ [1]. The space inside the solenoid is not sufficient to contain the hadronic showers completely, it is necessary to extend the barrel hadron calorimeter outside the solenoid. This part of the calorimeter which is located outside the coil is referred to as the outer hadron (HO) calorimeter.

4.1 Overview

The HO consists of scintillator tiles located on either side of CMS return yoke. CMS return yoke acts as the sampling absorber (30 cm thick). There are two layers of scintillator tiles for CMS central ring 0 and one layer each for ring ± 1 and ± 2.The scintillation light produced in the tiles is collected via WLS fibers embedded in grooves in the tiles. These WLS fibers are spliced to clear fibers and the clear fibers transport the light to the photodetectors located at outskirts of HO.

In order to simplify the installation of the HO scintillator layers, scintillator tiles are packed into a single mechanical unit called the scintillator tray. For ease of installation, each tray is chosen to be one slice wide (5^0). However along the Z-direction, they cover the entire span of a muon ring i.e. 2.53 m. The trays are held by light weight honeycomb panels, which also serves purpose of cooling support, are mounted onto the return yoke using 'L' shaped brackets and C-channels.

4.2 Experimental Justification of HO

An extensive study with the test beam was carried out during 1995 and 1996 [13] to define the parameters of the hadron calorimeter. It was noticed that with a configuration of HB alone together with the tracker and the electromagnetic calorimeter, nearly 3% of events having a 300 GeV pion gives rise to missing energy corresponding to 100 GeV. This large fluctuation of the leakage energy can be avoided by adding layers of detectors beyond the solenoid (the solenoid thickness is 1.4 λ_{int}) as shown in Fig. 4.1. This is the primary justification for the HO [14].

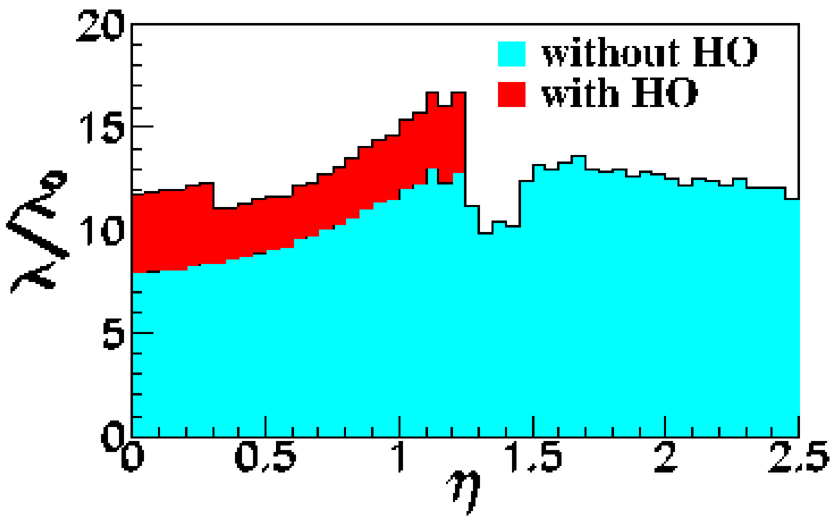

Figure 4.1: Number of interaction lengths till the last sampling layer of the hadron calorimeter as a function of η. The two shaded region correspond with or without (HO) [14] .

4.3 Requirements and Geometrical Constraints

The hadron barrel (HB) calorimeter inside the 4T solenoid is relatively thin (about 7 interaction lengths at $\eta = 0$). To endure adequate sampling depth for $\eta < 1.4$, a hadron calorimeter is extended outside the solenoid and is called HO. The HO utilizes the solenoid coil as an additional absorber equal to 1.4/sinθ interaction lengths and is used to identify late starting showers and to measure the shower energy beyond the reach of HB.

Outside the vacuum tank of the solenoid, the magnetic field is returned through an iron yoke designed in the form of five 2.536 m wide (along Z-axis) rings. HO is placed as the first sensitive layer in each of these five rings. The rings are identified by numbers -2,-1,0,+1,+2. The numbering increases with Z and the nominal central Z positions of the five rings are respectively -5.342 m, -2.686 m, +2.686 m, and +5.342 m. Near $\eta = 0$, HB provides minimum interaction length to the hadrons produced in *pp* collision. Therefore, The central ring (ring 0) has two layers of HO scintillators on either side of a 19.5 mm thick piece of iron. The total depth of the calorimeter system is thus extended to a minimum of 11.8λ_I except at the barrel-endcap boundary region.

The HO is geographically located inside the barrel muon system and hence is constrained by the geometry and construction of the muon system. Fig. 4.2 shows the position of HO layers in the rings of the muon stations in the overall CMS setup. The segmentation of these detectors closely follows that of the barrel muon system. Each ring has the 12 identical ϕ-sectors. The 12 sectors are separated by 75 mm thick stainless steal beams which hold successive layers of iron of the return yoke as well as the muon system. The space between successive muon rings in the η direction and also the space occupied by the 'chimneys' in sector 3 of ring -1, and sector 4 of ring +1 are also not available for HO. The chimneys are used for the cryogenic transfer lines and power cables of the magnet system. Finally, the mechanical structures needed to position the scintillator trays further constrain HO along ϕ. In the radial direction each HO layer has been allocated a total of 40 mm space of which only 16 mm is available for the detector layer, the rest being used

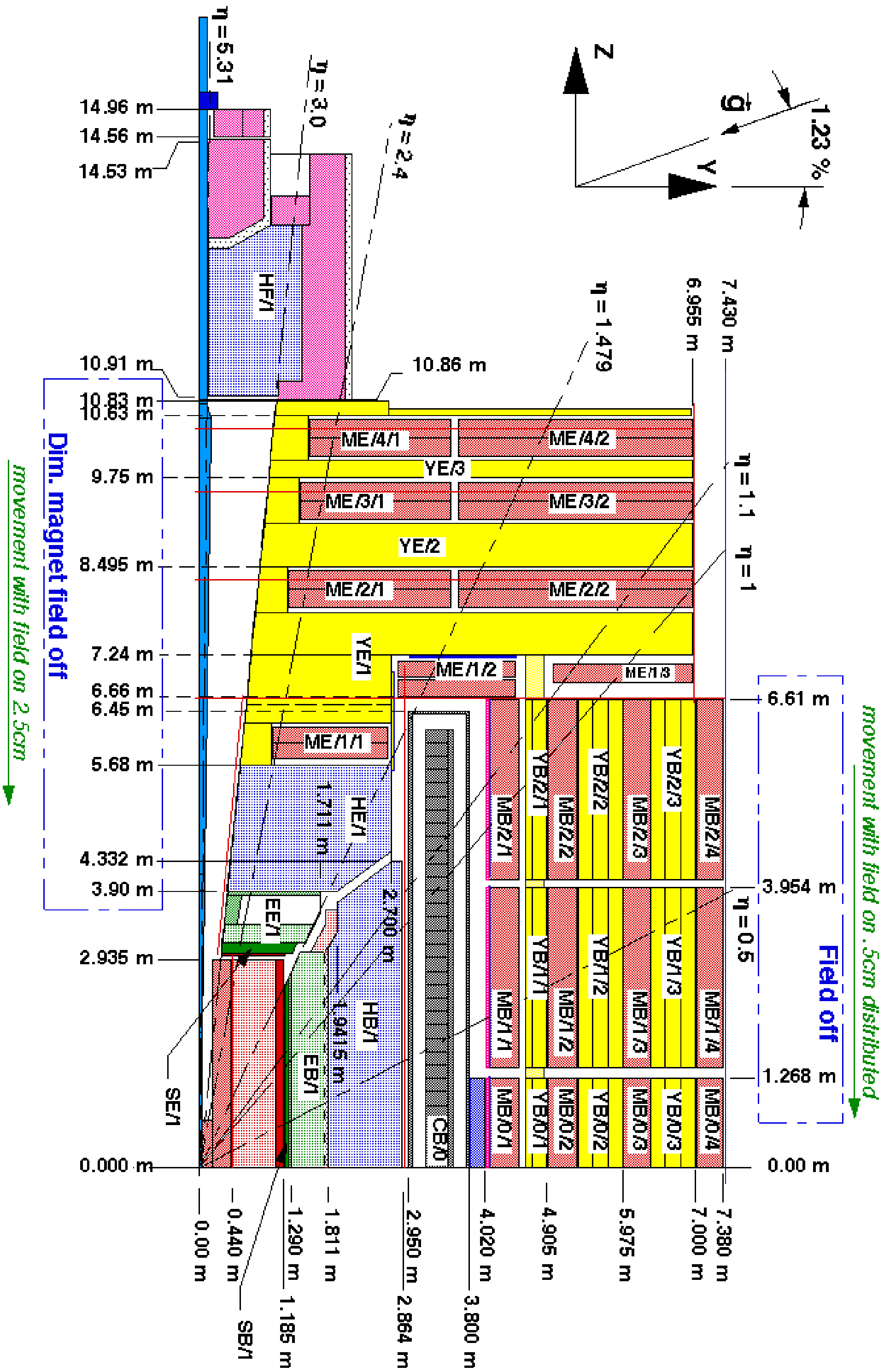

Figure 4.2: HO layers at 3.800m and 4.020m from the CMS collision point.

for the aluminum honey comb support structures on both sides of it. In addition, the HO modules are independently supported from the steel beams on either side of each ϕ-sector. The thickness and position of the iron ribs in the yoke structure further constrains the shape and segmentation of HO.

The scintillator layers of HO should map to the 5 rings of the muon station and the optical fibers have to be taken out through the space between the rings to the photo-detectors placed at the outer end of the ring (at the radius of 7.43 m). The rings are 2.51 m long and are symmetrically positioned (as shown in Fig. 4.3) with respect to the center point.

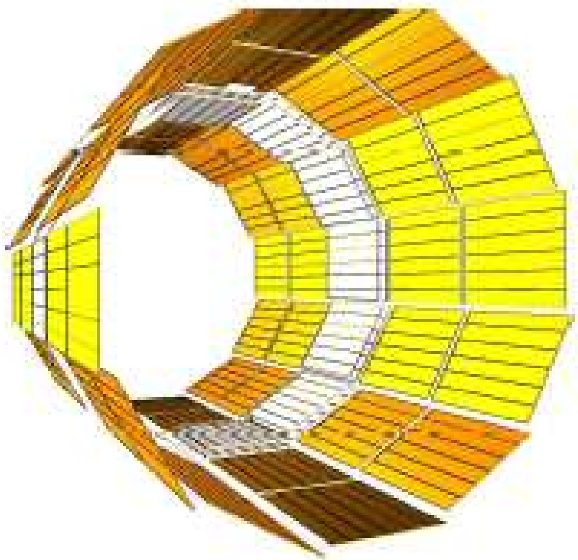

Figure 4.3: All HO trays ordered in 5 parallel rings in the CMS detector.

The sizes and positions of the tiles in HO are supposed to roughly map the layers of HB to make towers of granularity 0.087× 0.087 in η and ϕ as shown in Fig. 4.4. The

HO consists of one (rings ± 1 and ± 2) or two (ring 0) layers of scintillator tiles located in front of the first layer of barrel muon detector. Scintillation light from the tiles is collected using multi-clad Y11 Kuraray wave length shifting (WLS) fibers, of diameter 0.94 mm, transported to the photodetectors located on the surface of return yoke by splicing a multi-clad Kuraray clear fiber (also of 0.94 mm diameter) with the WLS fiber. Each tray corresponds to one ϕ slice (5^o) wide in ϕ. However, along the Z (η) direction, a tray covers the entire span of a muon ring.

4.4 Forces, Stresses and Deflections

The tray is supported along its whole length by Aluminum made honeycomb panels partitioned with the help of C-channels and is anchored to the iron yoke of the magnet. Therefore, there is no bending along the length of the tray weighing a maximum of 30 kg for the widest tray. Along the width (a maximum of 563 mm) of the tray, however there is bending amounting to a maximum of 0.2 mm for the widest tray caused mainly by the 10 mm thick scintillator. Other trays is having less bending due to narrower width. The separate and independent buckling of the 0.3 mm stainless steel plate is controlled by the brass screws and custom made nuts.

- **Static Loads and Constraints** : The weight of individual HO scintillator trays is in the range of 25 to 30 kg only. Each tray is supported by honeycomb Cchannels for the entire length of 2.53 m along the Z direction. Hence the weight per unit length on the tray support structure is less than 15 kg/meter.

- **Dynamic Loads and Constraints** : Since the weight of the trays is less than 30 kg and they are directly hanging from the return yoke, dynamic load is not a serious issue for these trays.

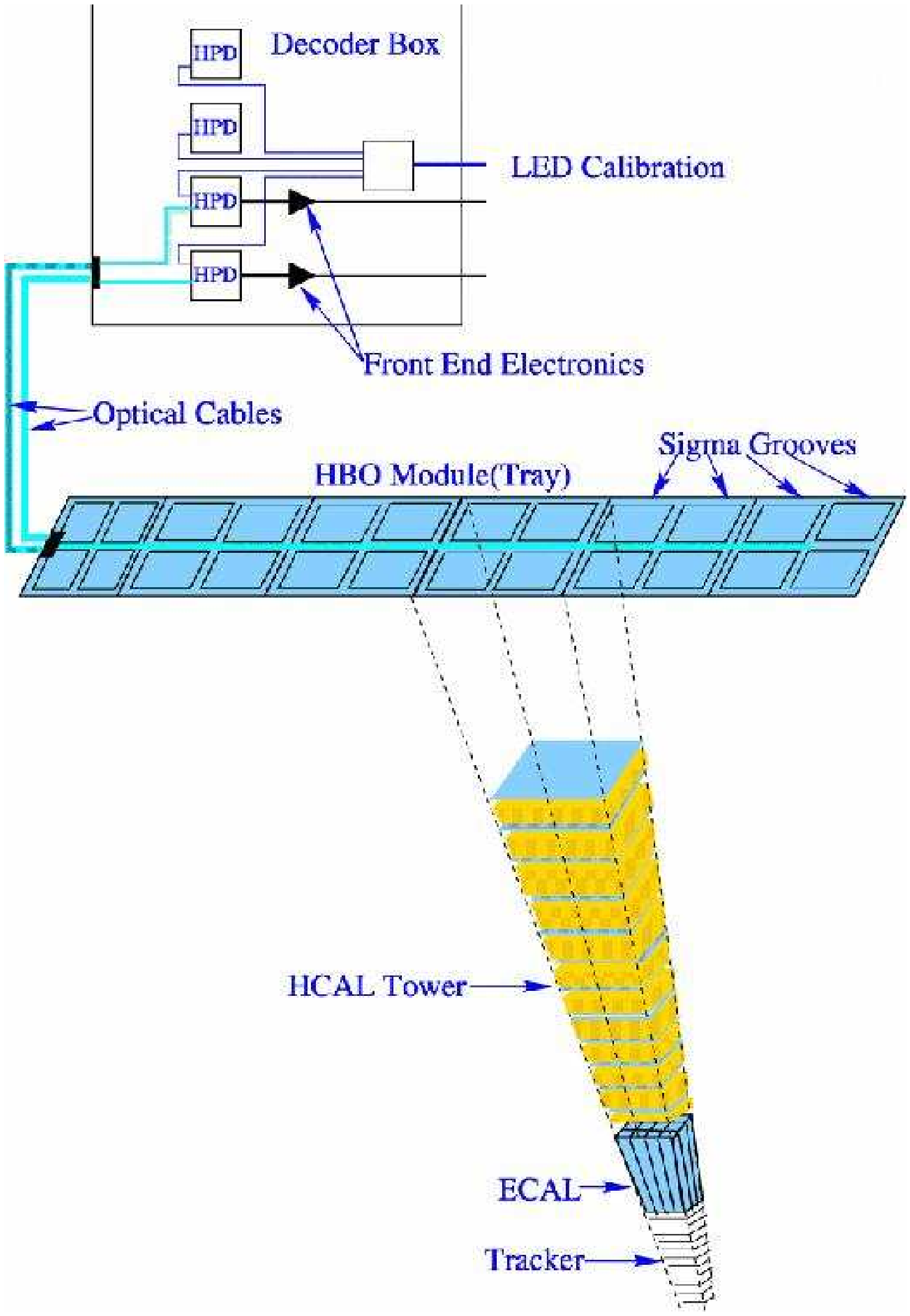

Figure 4.4: The layout of a HO tray in CMS tower.

4.5 HO Fabrication and Assembly

Indian contingent mainly from Panjab University, Chandigarh and Tata Institute of Fundamental Research (TIFR), Mumbai took the complete responsibility for the fabrication of the HO [4]. The HO is physically divided in to 5 rings in η confirming to the muon ring structure. The rings are numbered -2, -1, 0, 1, 2 with increasing η. Each ring of the HO is divided in to 12 identical ϕ sectors (numbered 1 to 12 counting clockwise starting from 9 O'clock position) and each sector has 6 slices (numbered 1 to 6 counting clockwise) in ϕ. The ϕ slices of a layer are identical in all sectors. In each ϕ slice the scintillator is further divided along η. The smallest scintillator unit in HO thus obtained is called a tile. Perpendicular distance of this plane from the Z-axis is 3.82 m for layer 0 and 4.07 for layer 1. The tiles in each ϕ slice of a ring are mechanically held together in the form of tray. Both layers of ring 0 have 8 η-divisions (i.e. 8 tiles in a tray): -4, -3, -2, -1, +1, +2, +3, +4 (as shown in Fig. 4.5). The ring 1 has six divisions: 5...10 and ring 2 has 5 divisions: 11...15. The ring -1 and ring -2 have the same number of divisions as rings 1 and 2 but with -ve indices. The η-dimensions of any tile with -ve tower number is the same as the one with +ve number. Length of the full tray is 2510 mm where as the shorter trays, the size of which are constrained because of the chimney (trays 4 and 5 in sector 4 of ring +1 and trays 3, 4, 5 and 6 in sector 3 of ring -1), are 2119 mm long.

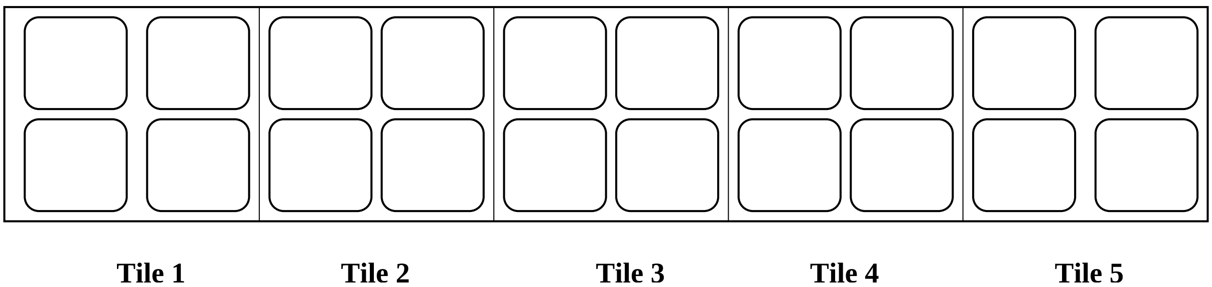

Figure 4.5: Arrangement of scintillator tiles in ring 2.

4.5.1 Scintillator Tile

The plastic scintillator tiles (as shown in Fig. 4.7) are made from BC408 scintillators plates of thickness 10 mm. Fig. 4.8 shows a typical HO scintillator tile. The WLS fibers are held inside the tile in grooves with key hole cross section. Each groove has a circular part (of diameter 1.35 mm) inside the scintillator and a neck of 0.86 mm width as shown in Fig. 4.6. The grooves are 2.05 mm deep. Each tile has 4 identical σ-shaped grooves, one groove in each quadrant of the tile. The grooves closely follow the quadrant boundary. The corners of the grooves are rounded to prevent damage to the fiber at the bend and to ease fiber insertion. The groove design is slightly different for the tile where the optical connector is placed at the end of the tray. Since the tiles are large, 4 grooves ensure good light collection and less attenuation of light. Machining of the individual tiles is done in the following steps:

- Bicron Scintillator plates are cut according to the size of the respective tile keeping 3 mm extra on each side.

- The edges are trimmed to the exact dimension of the tile using a conventional milling machine.

- Grooves and screw holes are made with Computer Numerical Control (CNC) machine.

- σ grooves are done in two steps, first a 'straight cutter' making 0.86 mm wide 'neck' and then a 'ball cutter' making the inner circular part of the groove.

  The HO has 95 different tile dimensions, 75 for layer 1 and 20 for layer 0 and total number of tiles is 2730 (2154 for layer 1 and 576 for layer 0).

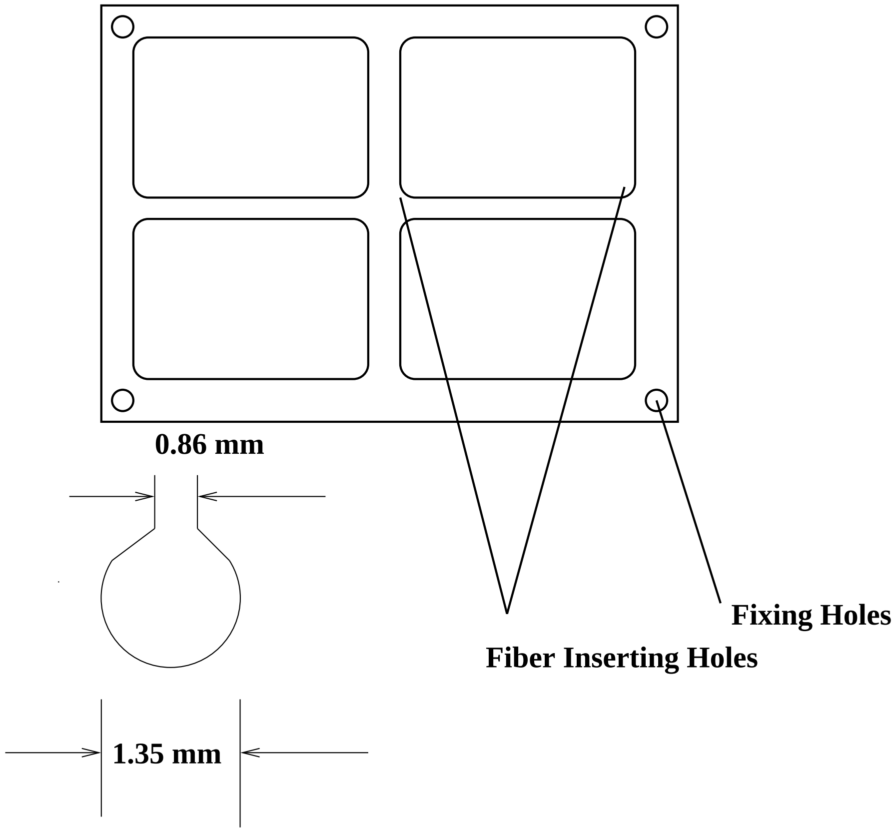

Figure 4.6: A typical HO scintillator tile with 4 grooves and neck dimensions.

4.5.2 Assembled Tray

HO detector module includes the assembly of scintillator tiles in to which WLS fibers are embedded through key-hole type grooves for taking out the scintillation light to the photodetectors [5]. Each tray contains 5 tiles in rings ± 2; 6 tiles in rings ± 1 and 8 tiles in ring 0. In order to simplify the installation of the HO layers, all the tiles in the same ϕ slice of a ring of the same layer are packed into a single unit called the 'tray'. A scintillator tray covers the entire length of a muon ring along Z (2.536 m). In the ϕ-direction, it is only one tile wide(5^0). The edges of tiles are painted with Bicron reflecting white paint for better collection of light as well as isolating the individual tiles of a tray. Further isolation of tiles is achieved by inserting a piece of black Tedler strip in between the adjacent tiles. The tiles in tray are covered with single piece of white, reflective Tyvec paper cut to the

Figure 4.7: A scintillator tile.

size of the tray. Then they are covered with black Tedlar paper to prevent light leakage. Then tray is packed between two plastic plates, with designed holes for fiber insertion, for mechanical stability and ease of handling. The top cover is 2 mm thick and bottom one is 1 mm thick. Fig. 4.8 shows the cross section of the tray to illustrate different components. The plastic covers (top and bottom) have holes matching with the holes in tiles. Specially designed countersunk screws passing through holes fix the tiles with the plastic covers.

The 2 mm plastic sheet on the top has 1.6 mm deep channels grooved on it (on the outer side) to route the fibers from individual tiles to an optical connector placed in groove at the edge of the tray. A 1.5 mm wide straight groove runs along the top cover to accommodate a stainless steel tube. This is used for the passage of a radio-active source for calibrating the modules. Each connector has two holes and they are fixed to the scintillator - plastic assembly. Each ϕ sector of each ring has 6 trays. There are 360 trays for layer 1 and 72 trays for layer 0. The certified fiber assembly called 'pigtail' has to be inserted with utmost care so that no fiber breaks in the σ-type grooves. After adjusting the source tube with the source coupler (at the front edge of the tray), an aluminum carrier is used for transportation.

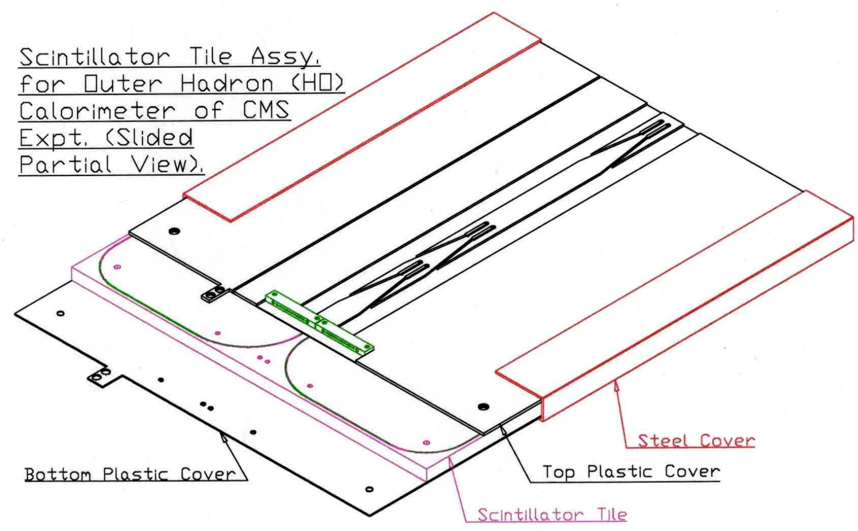

Figure 4.8: HO detector scintillator module called ‘tray’.

4.5.3 Pigtail

A pigtail consists of the WLS fiber which goes in the tile spliced to a clear fiber. A pigtail contains all the fibers for 5^0 of a scintillator tray. The light collected by the WLS fibers inserted in the tiles needs to be transported to photodetectors located far away on the muon rings. One end of the WLS fiber is mirrored by aluminium sputtering and dipped in a clear coating for protection. The other end is fused to a clear fiber of the same type and diameter. The other end of the spliced clear fibers for one row of tiles in a scintillator tray is inserted in an optical connector and is diamond cut polished. The other end of the WLS fiber comes out of the tile through a slot made on the 2 mm thick black plastic cover sheet. To minimize the loss of light in transportation, the WLS fiber (attenuation length of 1.8 m) is spliced to a clear fiber (attenuation length of 8.0 m) as shown in Fig. 4.9. The splice is a heat fusion splice and is covered by a 2.54 cm long, clear plastic ferrule . A fiber is spliced only if the potential loss using the WLS instead of a clear fiber is larger than the light loss at the spliced joint. Thus depending on tile length (along η) 2-3 fibers in each pigtail are made only of WLS fibers. The clear fibers from each tile follow the guiding grooves on the top plastic to the optical connector at the end. Each tray has two optical connectors mounted on one end of the tray. The fibers from all grooves terminate on these connectors as shown in Fig. 4.9. Optical cables in the form of a flat, light-tight bundle of clear fibers (0.94 mm) carry the light from the tray's connectors to a router box near the hybrid photo diodes (HPDs). The optical cables consist of 18 optical fibers sandwiched by a Tedlar cover. The bundle of these cables (megatile cables) has optical connectors to both sides matching the pigtail connector on one side and HPD connector to the other side which is seen on the readout electronics box.

Figure 4.9: Schematic diagram of the pigtail.

Following steps are followed to make a pigtail:

- WLS fibers are cut according to the size of the groove in the scintillator tile.
- Both ends are properly polished, one end is aluminized (sputtered) and coated with a thin polymer layer.
- Clear fiber is cut with a 1 mm extra length and one end is polished.
- The non-sputtered end of the WLS fiber and the polished end of a clear fiber are put in piece of 3 cm (approximately) heat-shrinking tube and spliced using the special splicing machine.
- Spliced fibers are placed in a jig in proper order and correctly inserted in the connector with the extra length (of the clear fibers), the extra length of 1 mm projecting

is out of the connector.

- Optical cement is prepared using a resin and hardener (Bicron BC600) and poured through socket in the connector.

- The pigtail is removed from the assembly jig after curing for 12-14 hours and the tray connector end is dipped in to the supercooled nitrogen and then polished with a high speed diamond cutter.

4.5.4 Assembly of Trays

The unit begins with a 0.95 mm thick, black polystyrene, bottom cover plate. Then comes a sheet of black, opaque, 0.05 mm Tedlar wrapped around the scintillator to provide an opaque layer of light tightening. Then the 10 mm plastic scintillator is covered on both sides with 0.15 mm thick, white, reflective Tyvek paper as depicted in Fig. 4.10. The surface of the scintillator tiles are grooved to hold the WLS fibers. The black Tedlar sheet is wrapped completely around the scintillator and the top Tyvek. One side of the Tedlar sheet is taped onto the upper Tyvek sheet, and the other is taped to the Tedlar thus completing the wrap. Above the scintillator plastic is a 1.9 mm thick, black polystyrene, top cover plate (fiber routing plate). Both the top and bottom plastic plates have the same transverse size as the scintillator. The fibers rise out of the scintillator through a 3.2 mm $\times$ 25.4 mm slot in the fiber routing plate into 1.6 mm deep grooves on the top side of the same fiber routing plate. The fibers are mass terminated at the edge of the tray into an optical connector. A mass terminated optical cable transports the light from the tray to the photo detector readout. The HO trays are fabricated in the following steps:

- The scintillator tiles are cleaned and their sides are painted with white (Bicron) reflecting paint for better light collection from all the ends.

- Plastic covers and tray covers are also cleaned with ethanol.

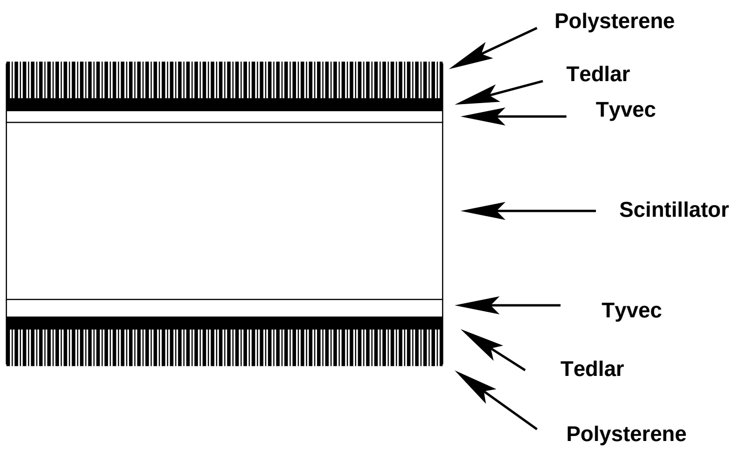

Figure 4.10: Cross sectional view of HO tray with its internal structure.

- Tyvec and Tedlar papers are cut according to criteria that top Tedlar and Tyvec are 2 mm shorter and bottom Tyvec by 22.5 mm and bottom Tedlar 100 mm larger than the tray covering plastic sheet at all the sides. Punching of holes is done while matching with those on the top and bottom plastic covers for insertion of screws.

- The bottom plastic sheet is placed with taped bushes for screws and pigtail connector on the separate table lying in the dust free room.

- The bottom plastic sheet, Tedlar and Tyvec papers are placed on the bottom sheet.

- The tiles are placed as well as adjusted on them. Two adjoin tiles are separated by strips of Tedlar paper, approximately of 9.5 mm, to optically isolate them.

- Upper Tyvec and Tedlar are put while taping them at each and every 5 inch with silver tape.

- Lower Tyvec and Tedlar are folded on top, the top plastic cover is then placed and countersunk screws are used to fix the assembly of plastic covers and tiles.

- Each fiber of a certified pigtail is cleaned and the WLS part of the fiber is inserted carefully into the groove through the slots in top plastic cover, Tedlar and Tyvec.

The clear fiber is routed along the groove on the top plastic cover and fixed at several places with adhesive aluminum tape.

- The optical connector sit in their appropriate slots on the top plastic cover and are anchored with screws through holes in the plastic sheet and scintillator.

- The source tubes are placed in the top of the 2 mm thick black plastic cover plate.

- The whole assembly is then placed inside a tray cover made out of 0.3 mm thick stainless steel sheets. This tray cover is used for transporting the trays to CERN and is removed while assembling inside the hanging structure. The performance of HO depends on the quality of grooving of the tiles, painting on the sides, tightly packed tray assembly, good splicing and fine polishing of the fibers in the pigtail assembly.

A light level of about 7 photo electrons (pe) due to single muon may be necessary to identify muons at 3σ level. Due to the large size of the scintillator tiles for the η - ϕ segmentation as in the HB and the limitation in the number of fibers that can be embedded in the tiles, we opted to use 10 mm thick BC408 scintillators for the HO for higher light yield. An additional 5 mm of space is needed for the two plastic sheets on either side of the scintillators to anchor the individual tiles, to route the fibers and also to accommodate the stainless steel covers for the scintillators. All together the thickness of the individual layers is $\simeq$ 15 mm.

4.6 Testing and Quality Assurance

Testing of the HO components can be classified in 3 major parts:-

- Testing of WLS and clear fibers.

- Testing and quality control of the scintillator tile.

- Testing and quality control of the HO fiber readouts and pigtails.

- Testing and quality control of HO trays.

These tests were performed partially at Panjab University and TIFR.

4.6.1 Testing of Fibers

The WLS optical fibers are used to collect light produced in the scintillator tile. The special property of the WLS fibers is to collect light through its surface, unlike clear fibers' end-to-end absorption and emittance, help in shifting wavelength of collected light to specific value. Using the WLS fibers, one can concentrate the light from the scintillator to the smaller photocathode area. We were involved to test the light output from these fibers with one end fixed near a photocathode and other being sputtered (reflecting material like Aluminium is deposited). The plastic in these fibers has been doped with special dyes that absorb the blue light from the scintillator and re-emit green light. Light produced by an ionizing particle inside the scintillator is absorbed by the WLS fiber and the re-emitted green light is guided by total internal reflection to the photo multiplier tube (PMT). For further transportation of the light to the PMT, a long clear fiber coupled to the WLS fiber by the optical connector. The clear fiber allows transporting the scintillator light to the PMT without significant attenuation. The output light from the fiber falls directly on the photodiodes and further the output is registered on the computer. Finally, we get the output signal voltage as a function of distance of source from the fiber end for which the attenuation has been checked. The intensity pattern is represented by sum of two exponentials of the form

$$I(x) = A_1 \times e^{x/a_1} + A_2 \times e^{x/a_2} \tag{4.1}$$

where A_1, A_2, a_1, a_2 are the fitted parameters.

Fiber Scanning Machine

The fiber scanning machine (FSM) is used for testing WLS and clear fibers and certify them to use for testing scintillator tiles at Panjab University. The block diagram is shown in Fig. 4.11. It shows the basic components of this machine. The stepper motor (SM) drives the pulley. In FSM, two pulleys of 124 mm diameter and having 28 teeth were chosen to drive a timing belt of width 20 mm and 14 mm pitch. The teeth of pulley match with the teeth of belt. One pulley is used as driver and the other is driven. The driver pulley is driven by SM. The pulleys are mounted vertically on a metal brackets and fine ball bearings are used for smooth movement. These two pulleys have belt around them and on the belt ultraviolet (UV) source holder is clamped. The movement of pulley drives the belt and the lamp moves as the belt moves. Motor wires are connected to driver and control circuit (motor driver card) and also to 12V/A power supply unit. A UV lamp is used as input light source (pencil shape) to fiber to supply the fiber's attenuation length and light emission across the spliced region of WLS fiber and clear fiber. The UV lamp procured from the M/S Oriel Instruments is fitted on a lamp holder and is made to move across the length of fiber. The lamp holder is further linked to special power supply provided by same firm. Two tubes of length 2.2 m are being used as guide to help the light source to slide. Two L-shaped brackets are used to hold these tubes and the distance between two is kept 60 mm. The source holder is made in such a way that it slides on the tubes. So the UV source mounted on the source holder moves along the length of the belt. The light source moves continuously across the length of fiber by the SM driven mechanical system.

The motor driver card consists of IC SAA 1027 to drive the motor. It is a 4-stage counter and code converter IC. Power transistors 3055 are used to boost the power. To avoid loading directly on the driver IC 1027 is used. The clock frequency, the direction and the reset pulses are being taken from the PC via interface card. In the fiber readout card, Light from the fibers is collected by photodiodes (S1336 - 5BK from Hamamatsu

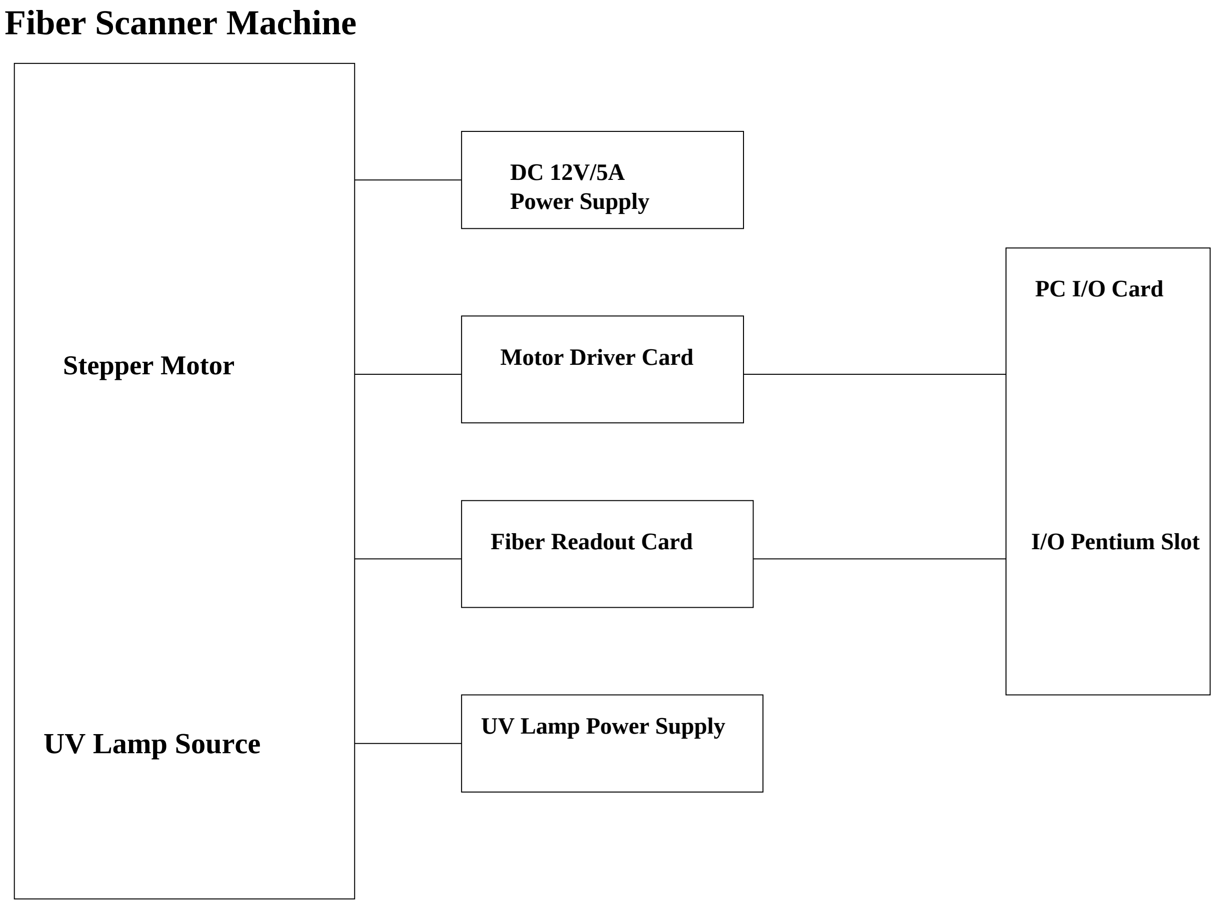

Figure 4.11: Block diagram of fiber scanner machine at Panjab University.

KK Japan) and a proportional voltage is generated by photodiode amplifiers.

The whole assembly, fabrication and testing of this scanner has been done at Panjab University. One metallic platform was made to hold 16 fibers at a time and was mounted on the machine at a reasonable height, so that the distance between the UV source and fiber is kept constant. Whole assembly of this scanner was installed in light tight black box so that there is no interference of external light.

Results

A number of fibers has been tested and checked for their quality. The fitted intensity of the fibers is shown in Fig. 4.12. It shows that the intensity pattern is represented by the sum of two exponentials as given in equation 4.1.

4.6.2 Testing of Scintillator Tiles

For testing scintillator tile it is needed that no light other than cosmic muon signal enter in to the scintillator material. The packing of the scintillator tile as tight packed unit is done in various steps. The scintillator tile is attached with light guide (which helps in collecting light from scintillator through different tested fibers) with the help of special optical glue. The cookie is attached with light guide with the help of optical optical glue. Tyvec is wrapped to all the sides of the scintillator as well as light guide. This Tyvec helps in reflecting back the light into the scintillator and further to photo multiplier tube (PMT) through the light guide. Now wrap the whole detector neatly in Tyvek (reflecting paper). Special care is taken that the detector is covered properly as the corners and sharp bends where light leaks might likely occur . Another wrapping of the whole detector is to be done by using black Tedler paper and black tape in the same fashion as in the previous step. The optical grease is applied to the face of PMT and attached it with cookie of the wrapped scintillator with the help of aluminum coupling provided for the purpose. Black tape is used to fix cookie and PMT with coupling [6].

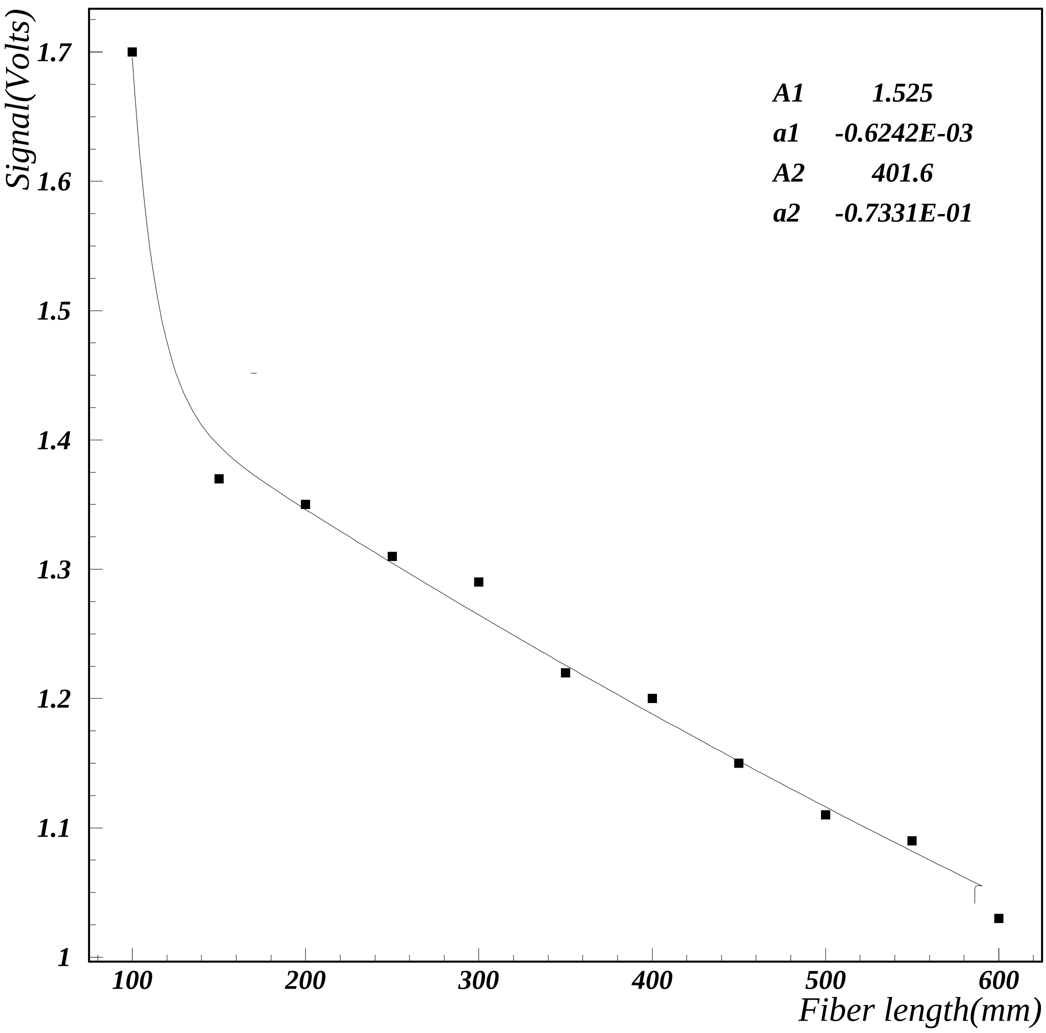

Figure 4.12: Output of fiber scanner for single WLS fiber.

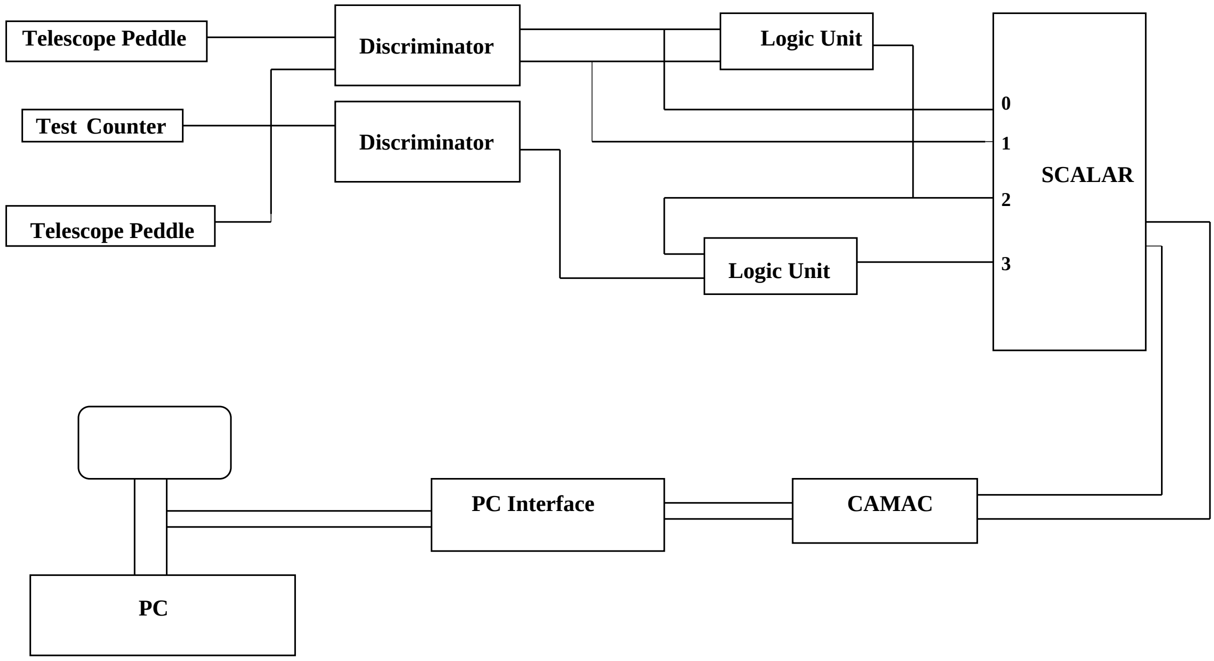

Figure 4.13: Block diagram of data acquisition system (DAQ) used for cosmic MIP testing of a scintillator tile at Panjab University.

Testing Procedure

The test counter (scintillator tile in our case) is placed between the two master paddles and cosmic muons are allowed to pass through all the three. The geometrical arrangement of the two master peddles and the counter is so done that surface area of the three overlaps each other. The block diagram of data acquisition system (DAQ) used for cosmic MIP testing of a scintillator tile is shown in Fig. 4.6.2. This is important to have maximum number of counts in coincidence. The counter under test is given the required high voltage and the signal is observed on the oscilloscope for its height, amplitude and noises etc. After studying the signal on oscilloscope we know the threshold voltage to be set at the discriminator channel to which the counter signal is to be attached for discriminating and converting into NIM signals at the output. The two signals from the master peddles are fed to the logic unit after discriminating independently. If the particle triggers both the scintillators the signal in both the photomultipliers shall be time coincident. We get

2-fold coincidence at the output of the logic unit. This two fold output is formed only when signal is accepted by both the master peddles. This 2-fold signal is now fed to another input channel of the logic unit. Similarly the signal from the counter is also fed to the same channel of the logic unit where the 2- fold signal is fed. The output of this logic unit channel then gives us the 3-fold coincidence. For checking the efficiency of the counter under test we use a scalar module for counting 2-fold and 3-fold counts. In our system we connect the independent counts of the two master peddles to channel 0 and 1 and 2-fold, 3-fold counts to the channel 2 and 3 of the scalar unit respectively. Since Scalar has no display of its own and is a CAMAC module, it is wired to a computer through CAMAC controller and PC interface. A simple software is provided in the PC with which help we can have reading of each channel of the scalar. The efficiency of the counter is calculated as below

$$Efficiency = \frac{Number\ of\ 3-fold\ counts}{Number\ of\ 2-fold\ counts} \tag{4.2}$$

Observations

The top and the bottom peddles are standard peddles with EMI photomultiplier numbers 66264 and 66272 respectively. The third photomultiplier tube number 66265 is used for the test counter X. The optimum operating voltage for all the tubes is given as HV = 1550 V. The threshold voltage all the three counters is 40 mV. The following tables gives the record of reading taken on the scalar and the calculated efficiency of the counter X.

CHANNEL	COUNTS	FREQUENCY
0 (Peddle A)	21553	35.9
1(Peddle B)	19279	32.1
2 (2-fold Coincidence counts)	523	0.9
3 (3-fold Coincidence)	507	0.8

Table 4.1: Efficiency of the counter X is 96.94% (rate/10 minute).

CHANNEL	COUNTS	FREQUENCY
0 (Peddle A)	22434	36.2
1(Peddle B)	20171	32.5
2 (2-fold Coincidence counts)	519	0.9
3 (3-fold Coincidence)	504	0.8

Table 4.2: Efficiency of the counter X is 97.10% (rate/10 minute).

CHANNEL	COUNTS	FREQUENCY
0 (Peddle A)	22628	36.0
1(Peddle B)	20752	32.9
2 (2-fold Coincidence counts)	514	0.9
3 (3-fold Coincidence)	498	0.8

Table 4.3: Efficiency of the counter X is 96.88% (rate/10 minute).

The above three tables are the repetition of the reading taken on Counter X. We normally let the counter test for more time and take repeated readings. The average efficiency of the readings given in three tables of counter X comes out to be above 96%.

4.6.3 Testing of Pigtails

Pigtails are the optical fiber assemblies. They are tested using a pigtail scanner [7] in order to ascertain their production quality as well as to decide about their acceptance as a signal-readouts of the HO detector trays in the CMS detector. The pigtail scanner is shown in Fig. 4.14. It uses an ultraviolet lamp controlled by electromagnetic shutter to excite pigtail fibers. A special cable made up of WLS fibers is used to normalize the light output of individual photodiode readout channels. While one end of the fibers of this cable are terminated on a connector, the other end of the fibers are coupled to the photodiodes. The pigtail is mounted on the scanner with a grooved plastic template with its connector coupled to the WLS cable. While the ultraviolet lamp moves in controlled steps, starting from one end of the WLS cable (called home) to the other end of pigtail, re-emitted light from pigtail fibers is readout at each step. The quality of each fiber is then assessed by using intensity with respect to fiber length. The photo-diode signals are then digitized and stored in a data file. The combined transmission loss due to the spliced junctions, connector interface and attenuation offered can be estimated by analyzing these data.

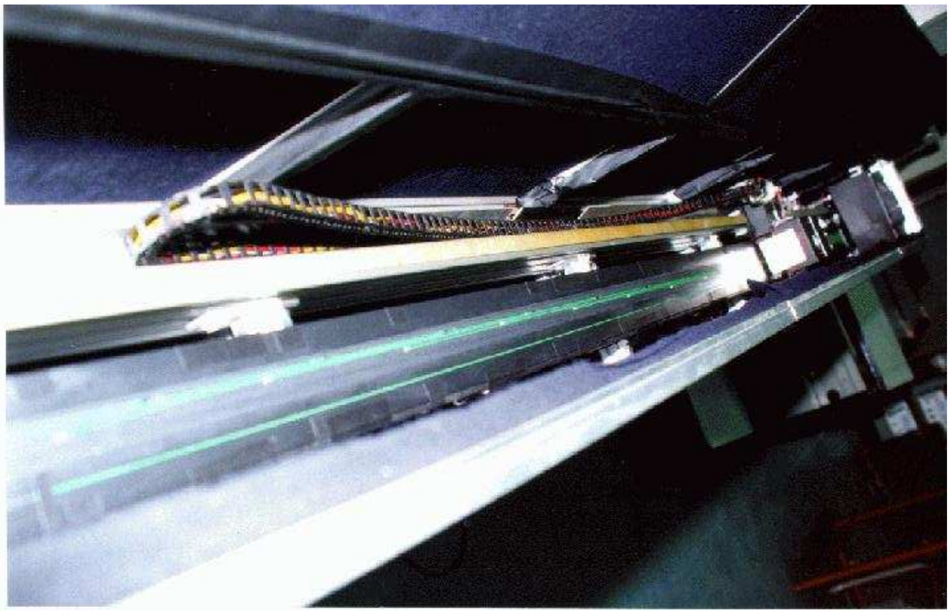

Figure 4.14: Pigtail scanner.

Data taking, Analysis and Acceptance procedure

- **Data Taking:** It is noted that we can record the intensity only when UV lamp is exciting the WLS fiber regions. So absolute measurements are not possible, we make relative comparison of light output from fibers of all the pigtails having identical lengths of optical and WLS fibers. Scan of the each pigtail is referred as pigtail run. A pigtail run starts from connector side and goes till end of the pigtail. The relative light output from each fiber of the pigtail is recorded and then studied. If a particular fiber shows large deviation from the mean intensity of twelve fibers, then it can be a candidate for a rejected fiber. For avoiding systematic variations in the scanner, intensity can be normalized for each fiber.

- **Analysis and Acceptance procedure:** A pigtail run is accepted if the average normalized intensity of all the fibers in that pigtail is within 10% of the global average of this value across all the pigtails in a single test group. The lengths of WLS and clear fibers at different positions on the pigtail need not be same and hence they have varying light losses. Therefor we do not expect the normalized intensity to be the same for all fibers in a given pigtail. In order to obtain this intensity distribution, the normalized intensity needs to be re-scaled so that this data across all fibers and pigtails can be combined and compared. The re-scaled normalized intensity of a fiber should be more than (1σ). The splicing quality of the fibers over the period of production is monitored by measuring the transmission efficiency between several bunches of two WLS fibers, before starting actual splice session on each day. The mean transmission efficiency and its spread over the entire production was found to be about 95% and 3% respectively.

4.6.4 Testing of HO Trays

The performance of HO is checked for its sensitivity, to produce a usable signal for a given radiation and relation between the amount of scintillation light and the charge contained in the output signal i.e integral of the pulse with respect to time achieved by using photo-sensor and charge sensitive ADC. Testing and quality control of the HO detector trays is done using cosmic-muon test, open radioactive wire source test and collimated radioactive X-Y scanning [8].

Cosmic-Muon Test

The HO is expected to supply at least 10 photo electrons per minimum ionizing particle (MIP) if a photo multiplier tube (PMT) were used. The completed modules are tested for its response to MIPs using cosmic rays in a special stand designed for this purpose (Fig. 4.15). The tray is placed in a black box equipped with a set of 8 telescopes. Each telescope has 4 scintillators with photo multiplier read out. The muons are selected using 4-fold coincidence trigger logic.

Figure 4.15: The Cosmic test set up.

Signal from the tiles are grouped into two bunches (alternate tiles) and the two bunches are then led to two fully calibrated green extended PMT. The electronic signal sent to a charge-sensitive ADC for converting it into the digital one. Online data is acquired in a PC via GPIB-CAMAC interface. These PMT's are calibrated using a precisely controlled LED source to get the factor for ADC count per photo electron. Using the calibration factor of ADC (here is 5.5/photo electron), we can calculate the number of photo electrons produced in the particular tile. Data are monitored online and there is a calibration tile equipped with fiber readout which is placed separately and is always read out to monitor PMT gains. The pulse height spectrum is analyzed offline to determine the number of primary photoelectrons produced. This yield incorporates the light attenuation due to pigtails and reduction due to a number of factors on the way to photo detector. The Fig. 4.16 shows a typical ADC cosmic data spectrum for a ring 0 tray.

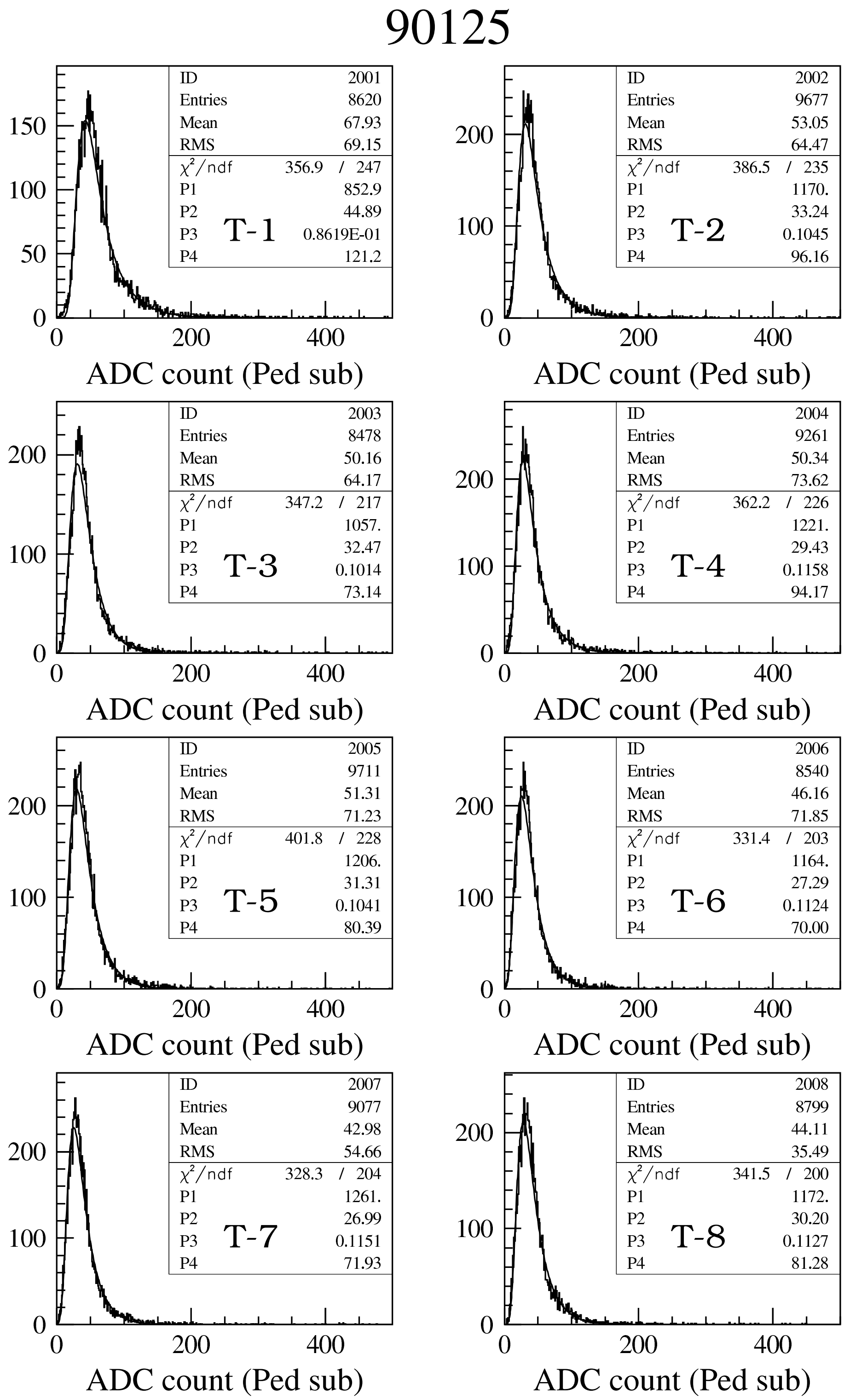

Figure 4.16: The cosmic test data output for 8 scintillator tiles of a ring 0 tray.

Radioactive Wire Source Test

A radioactive source traveling in guide tubes can be moved across each of the scintillators in the central calorimeter and is used to establish the calorimeter absolute energy scale. The wire source test is one of the quick quality control tests of the completely assembled HO trays. The wire-source test [9] is designed to calibrate scintillator tiles with respect to each other. Each tray is equipped with a thin stainless tube which can route a wire carrying radioactive source on tip across the tray. A stainless steel wire with a point-like Co^{60} radioactive source of approximate strength of 3 millicurie is wound as a coil and kept in a garage position inside a lead container as shown in Fig. 4.17. This wire is pushed through the stainless steel attached to the tray by a remotely controlled system of drivers. The DC signal induced by the source traversing one tile of a tower provides an accurate measurement of the response of the entire measuring chain. The change of response due to photo-detector or electronics shows up as a change of the response of all tiles of a given tower and is compensated by an adjustment of the overall calibration factor.

Figure 4.17: Radioactive wire source container.

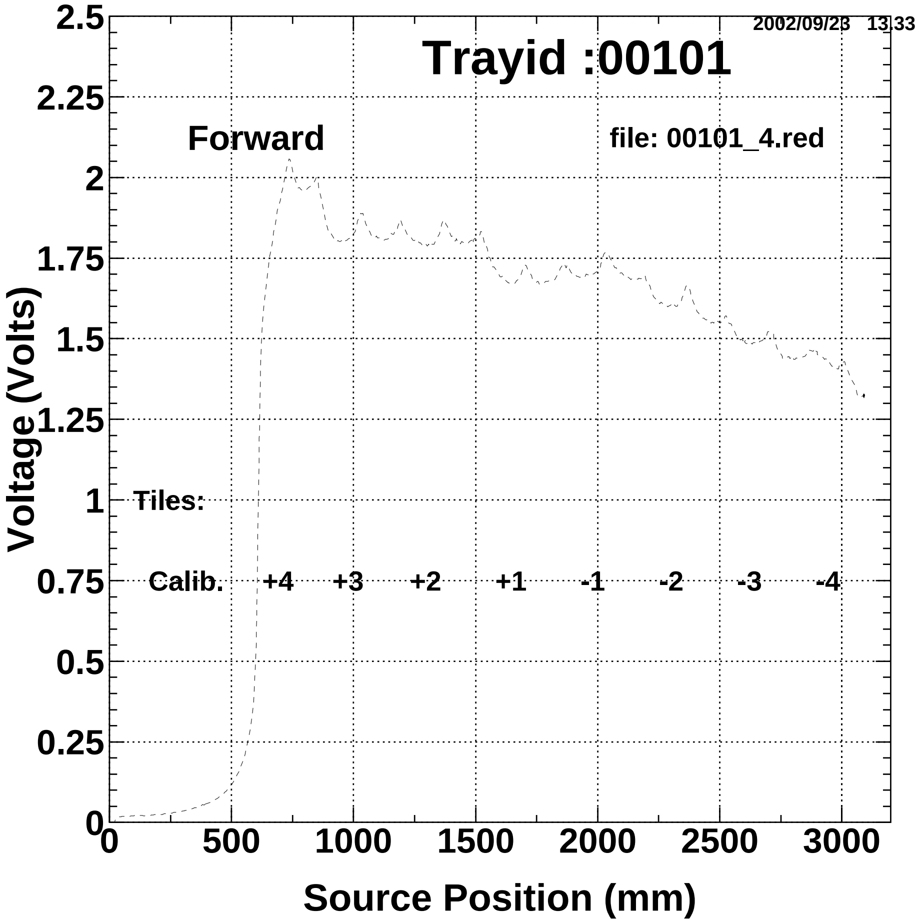

Figure 4.18: Radioactive wire source output for HO ring 0 layer 0 sector 1 tray 1.

The steps involved for doing the wire source test are:

- The tray under test is positioned inside the test shelf after making sure that the wire-source tube and the coupler are properly mounted on the tray.
- The flexible black tube from the wire-source tube driver end is inserted in the brass source coupler fixed to the end of the tube on the tray.
- The high voltage and the signal cables should be connected to the detector at the decoder box end and the two high voltage supplies have to be made on setting them to the values 960 volts and 990 volts for PMT A and PMT B respectively.
- Allow about 15 minutes interval before taking the data.

The voltage output is monitored as a function of the position of a Co^{60} of 3 mCi strength source on the tray. It is monitored twice during a run, once while stretching the wire and again while retreating to the garage position. Fig. 4.18 shows the result from a typical run for the a tray belonging to ring 0 layer 0 position 1. The height of the signal is largest near the connector end (shortest fiber path) and there are several spikes which correspond to source positions where WLS fiber(s) directly see the effect of the source. The wire source response depends on the lateral size of the tile, the location of the source tube, and in a nonlinear way on the thickness of the scintillator.

Radioactive X-Y Scan

X-Y Scanner is another instrument used to test and maintain production quality of the HO detector trays. Each Tray has also been tested with a radioactive source which not only scans along its length but also across its width. This X-Y scanner, as shown in Fig. 4.19, moves a collimated collimated Cs^{137} (10 mCi) radioactive source housed in an appropriate lead container over the entire surface of a HO tray. The light yield is measured with the source placed at different points on the tray. The basic framework as well as the X-Y positioning mechanical sub-system of the scanner is designed using extruded special aluminum channels. The stepper motor driven belt and pulley scheme is used on X and Y drives. The positioning accuracy of the scanner is about 1 mm over a span of about 3000 mm $\times$ 500 mm. The X-Y motion control, its monitoring as well as light readout are implemented in terms of PC based control and driver hardware modules. Fig. 4.20 shows the ADC output at several x and y points over the surfaces of twelve trays of tray type 3 belonging to ring 0 and layer 0.

Steps for X-Y scan of HO tray are:-

- The detector tray is mounted on the aluminum mounting plate while it is being tested. Stoppers and alignment guides have been provided on the mounting plate for this purpose. The detector tray should be mounted such that the connector end

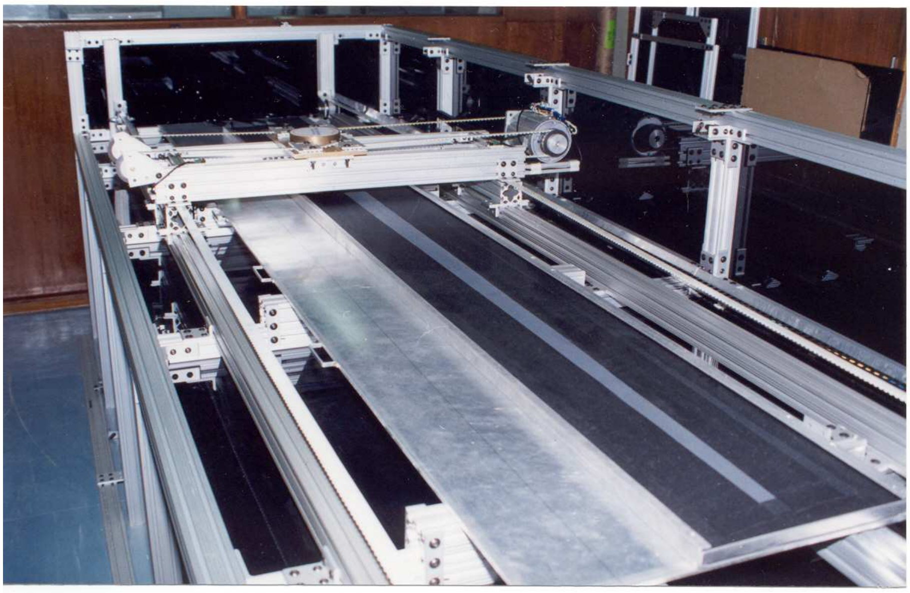

Figure 4.19: Radioactive X-Y scanning unit.

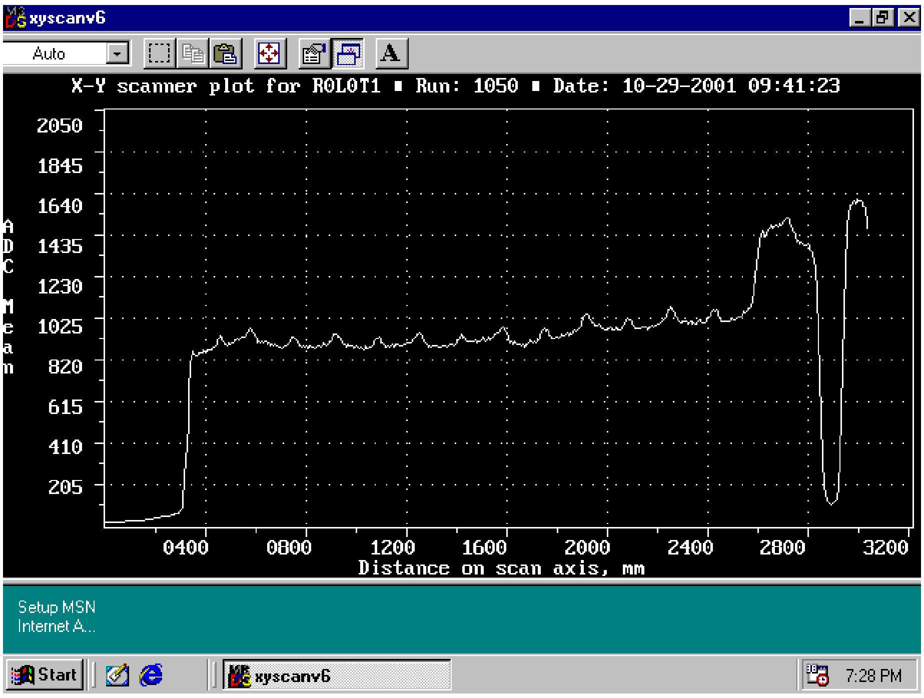

Figure 4.20: Radioactive X-Y scanning output for single HO tray.

of the tray along with its tray carrier are aligned with the L-shaped guide on the mounting plate.

- A pair of cables should be connected to the pigtail connectors on the tray, while the other pair of cables are stored inside a black cloth bag provided for this purpose. Wipe the connector surfaces with a dry tissue paper before connecting.
- Entire tray along with the optical cables and the PMT assembly should be covered with black cloth.
- The PMT is operated at a nominal voltage of 1457 volts. Allow about 20-30 minutes for the PMT supply to stabilize.
- Turn on Current-to-Voltage converter's power supply as well as the stepper motors' power supply. Also turn on the PC monitor.
- The radioactive source moves in the predetermined route on the tray and records the data.

The collimated source excites all tiles in a similar way [10]. With the collimated source, tiles are excited in direct proportion to their dimensions. It is clearly observed that signal size for tiles close to the connector is largest and it slowly decreases for tiles with larger fiber length. A scintillator tile which is permanently fixed on one end of the scanning table is used to cancel out day to day gain variations in the readout system. The little peak at extreme right (near to source position 2900 mm) in Fig. 4.20 is the signal from this tile which is used to normalize signals from the trays of the same sector. This instrument is also used for obtaining the uniform response scan of the entire tray.

Correlation of Calibration Constants

Correlation between all these tests are shown in Fig 4.21. One finds that they are fully correlated. The same set of readout system for cosmic and wire source test, where as a different PMT, optical connectors are used in the XY-scanner. Statistical error on these measured variables are less than 1%.

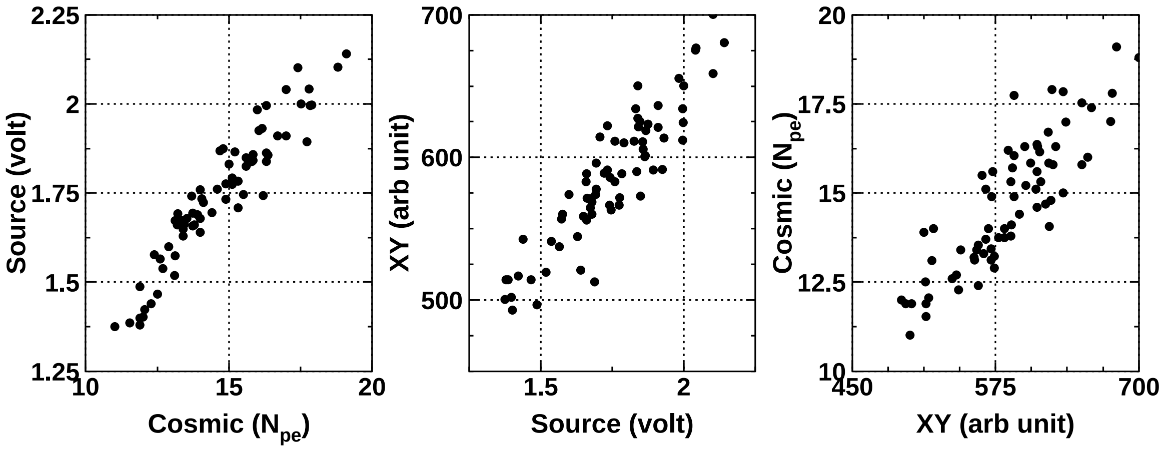

Figure 4.21: Correlations between number of photo-electron in cosmic test and signal peaks in the wire source and XY source test.

4.6.5 Tests at CERN

The open and collimated radioactive source tests were also performed at CERN, for all HO trays after transportation, to rule out any possibility of damage caused during shipment. All trays were found to be good in terms of their signal response at CERN. The two sets of measurements are seen to be fully correlated. Individual radioactive wire source and X-Y scanner plots for set of one full sector trays are shown in Figures 4.22 and Fig. 4.23 respectively. The correlated signal peak values are shown in Fig. 4.24.

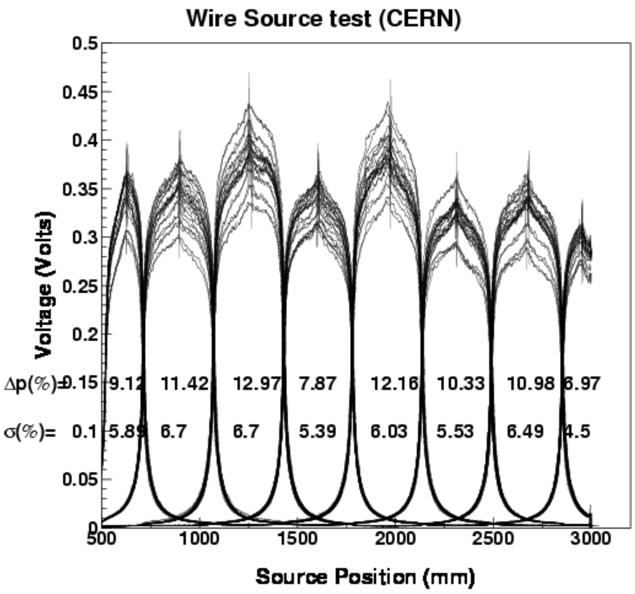

Figure 4.22: The wire source output for all 12 trays of ring 0 sector 1 at CERN. It is clearly observed that signal for bigger scintillator tiles is more than the smaller ones.

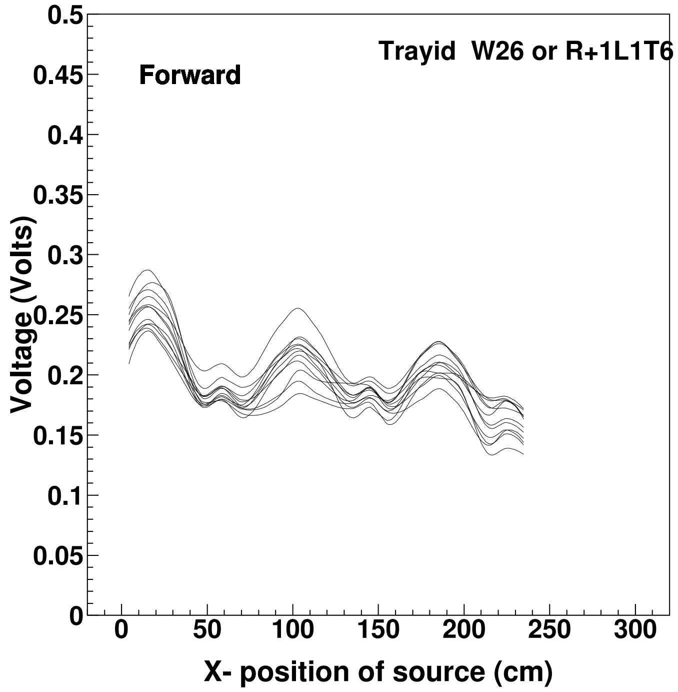

Figure 4.23: The XY scan output for all 12 trays of ring 1 sector 4 at CERN. The peaks in the plot are directly proportional to scintillator tile dimensions.

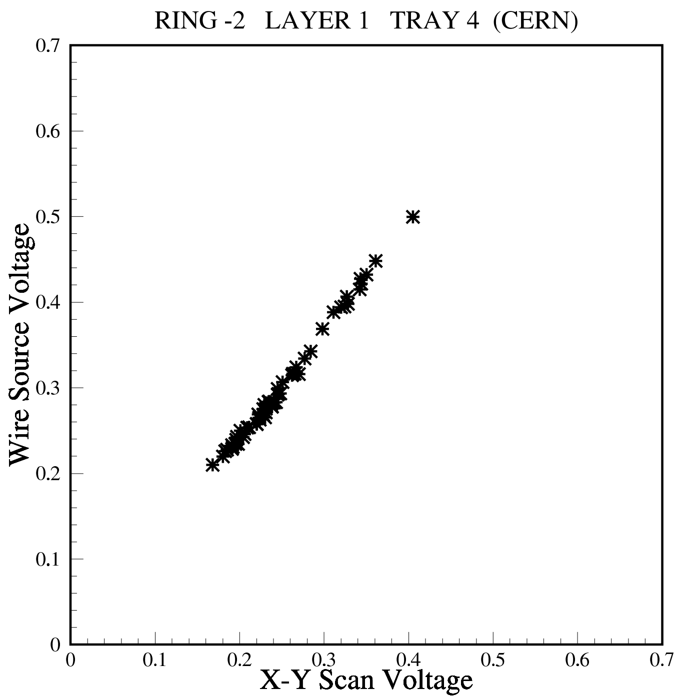

Figure 4.24: Correlations between wire source and XY scan peak values of all 12 trays of sector 1 of ring -2 at CERN.

4.7 HO Front End Electronics

The calorimeter detection elements are scintillators readout with wavelength shifting plastic fibers and hybrid photo diodes (HPD) as photo detector. A path from signal from the detetor to ADC counts in CMS HCAL is shown in Fig. 4.25. The shape of the light pulse produced in an initial step followed by an exponential decay corresponding to the fluorescence characteristics of the combined scintillator-wavelength shifter system. The current produced by the photodetectors is integrated (and digitized) over each 25 ns interval separately. The outer detectors of the central and end cap calorimeters, HO and HE, are required to be sensitive to minimum ionizing particles.

Readout of the CMS hadron calorimeters is realized through a chain of system elements beginning with photodetectors coupled to light produced in the calorimeter detection media and ending with memory storage of digitized results in an online processor farm. Signal processing functions required for the calorimeter readout electronics chain

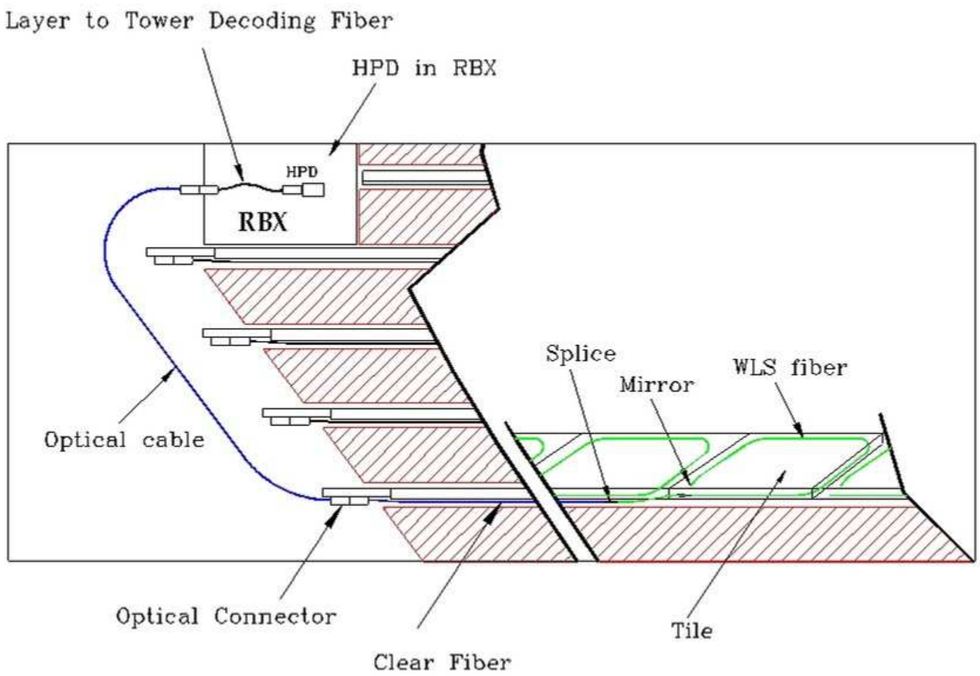

Figure 4.25: A path from signal to ADC counts in CMS HCAL.

during colliding beam operations can be summarized as follows: analog signal conditioning of photo detector responses, digitization of conditioned analog signals, transmission of digitized values, linearization and conversion of front end results into deposited energy values, first and second level triggering. All of the above 40 MHz signal processing operations at the very front end of the system are synchronous with accelerator operations and are phase locked to the beam crossings. The higher levels of the readout system operate at an average "interesting event" rate of 100 kHz and are decoupled from the synchronous, pipelined front ends by a set of derandomizing buffers.

The front end electronics system comprises those components located on the detector in close proximity to the calorimeter photodetectors. These components provide the functions of analog signal conditioning, digitization, synchronization/control, and data transmission. The front end electronics consists of readout boxes (RBXs) mounted on the detector, which receive the optical fiber signals from the HO trays, route the individual tile signals to the HPD pixel which sums the light from each tower, digitizes the tower energies, and transmits the result via digital optical fiber links to the HCAL trigger and readout (HTR) cards in the electronics cavern as shown in Fig. 4.26.

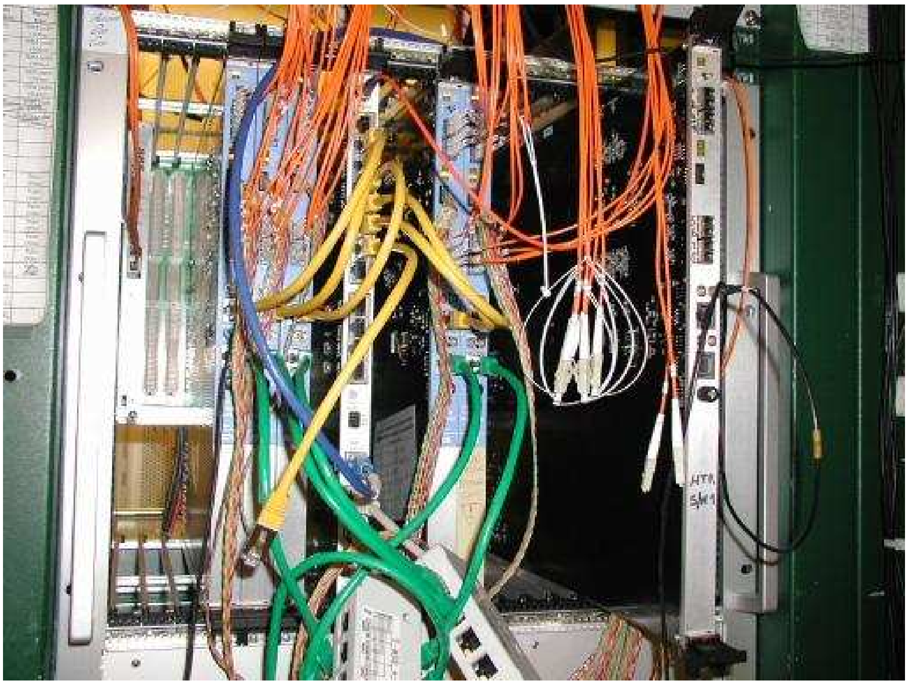

Figure 4.26: The readout crate with 6 HTRs, one trigger timing and control (TTC), a Fan Out, and a data concentrator card (DCC).

The precision of measurement requirement, or the granularity of digitization, is set by the energy resolution performance of the calorimeter systems themselves. Resolution is an energy dependent characteristic resulting from statistical fluctuations in shower development and measurement sampling coupled with energy independent effects due to systematic variations in calorimeter response as a function of point of impact or depth of shower initiation. A special case occurs, the granularity of digitization requirement is determined by a need to measure signal-to-noise values with precision at the low end of the scale. Light emitting diodes are included in each photo detector enclosure for calibrating the readout modules (RMs). The frequency of pulsing is arbitrary and could be set high enough to verify the readout capability at the beam crossing rate. QIE is an acronym for the functions of the ASIC, Q (charge) I (integration) and E (encode). A large dynamic range is accomplished through a multi-range technique. The input current is simultaneously integrated on all ranges, and comparators are used to select the lowest range that is not at full scale. The outputs are a voltage representing the integrated charge plus a three-bit gray code indicating the range. Operations are time multiplexed and pipelined to allow signals to settle and to make the reset interval the same as the integration interval.

4.7.1 Readout Box

Each readout box (RBX) as shown in Fig. 4.27 is an aluminum shell with copper pipe for cooling water, high voltage and bias voltage distribution system, electrical backplane, 4 readout modules (RMs) which receive the tile fiber signals and transmit the digitized tower energies, calibration module (CM) having light emitting diode (LED) which illuminates 18 pixels of each HPD in calibration mode. 4 optical output connectors (18 optical fibers per connector) on the front face of the calibration unit connected by 4 optical input connectors of each RMs. One clock and control module (CCM) installed in each RBX conditions and digitize data from calorimeter and functions in receiving and distributing a 40 MHz clock, monitor the temperature at the FE cards and the power supply voltages present on the black plane, provide a means for main control system to communicate with ASIC's located on the FE (slow control system). The HF houses similar functionality in a VME (versa module eurocard) crate which receives the electrical signals from PMTs housed in the Rho-boxes.

4.7.2 Readout Module

The readout module (RM) as part of CMS HCAL readout system consist of aluminum shell, optical decoder unit (ODU), hybrid photodiode (HPD) with interface card (IC), high voltage (HV) and bias voltage (BV) part, electronic compartment and optical output. Electronic compartment composed of 3 QIE card (6 channels per card), separated by

Figure 4.27: Complete RBX with 4 RMs, calibration module, CCM, and HV and LV supply link.

cooling extrusion aluminum plates. The front end electronics requires external services like high voltage (HV), low voltage (LV), slow controls. Light is delivered to the ODUs from the megatiles by optical cables. ODU encoded the light into tower structure. Each single tower corresponds to single HPD pixel after decoding.

4.7.3 Photodetectors

HCAL photodetectors should stand against CMS strong 4 Tesla magnet field and linear response over a range of signals from minimum ionizing to 3 TeV hadron showers. The photo detector must operate adequately for at least 10 years of LHC operation. The HPD consists of a photocathode followed by a gap of several millimeters over which a large applied electric field accelerates the photoelectrons onto a silicon target. The gain of such a device is therefore given by the acquired kinetic energy of the photoelectrons (above some threshold energy which depends on the surface treatment of the diode) divided by the 3.6 eV required to release an electron-hole pair in the diode. For an applied voltage of 15 kV, a gain of approximately 3000 is realized.

The HO trays are expected to supply approximately 10 p.e./MIP if a PMT were used. Since the function of the HO detectors is to tag muons and to tag and measure late developing showers, there are not very stringent requirements on the photo-transducer. Indeed, since the HPD has sufficient performance to meet these requirements, and since the commonality argument is compelling, we also chose HPDs for the HO detectors as the baseline.

4.7.4 Testing Setup for Readout Modules

RBX is used to read data from the HO trays. The set up to test readout modules (RMs) includes:

- Two PC's used (one Lynx based for data acquisition (DAQ) system and analysis, and one with window based for monitoring and control) and are interfaced to the RBX via a VME system.
- HV unit has separate interface and control from moniter PC. Four modules are used (one for Quality Control (QC) and three for Burn-in test).
- RBX box consists of 4 RMs, CCM, CM, HV supply module, LV supply (7.5V and 5V) modules, temperature sensor on all modules etc.
- Cables connecting the RBX are
  1. Four Signal (Orange color) cables (each one from RMs)
  2. TTC clock and calibration cable (PIN diode)
  3. Unshielded twisted pair (UTP) cable from CCM to HUB.
  4. Two LV and one HV cable.
  5. Detector control system to HV unit.

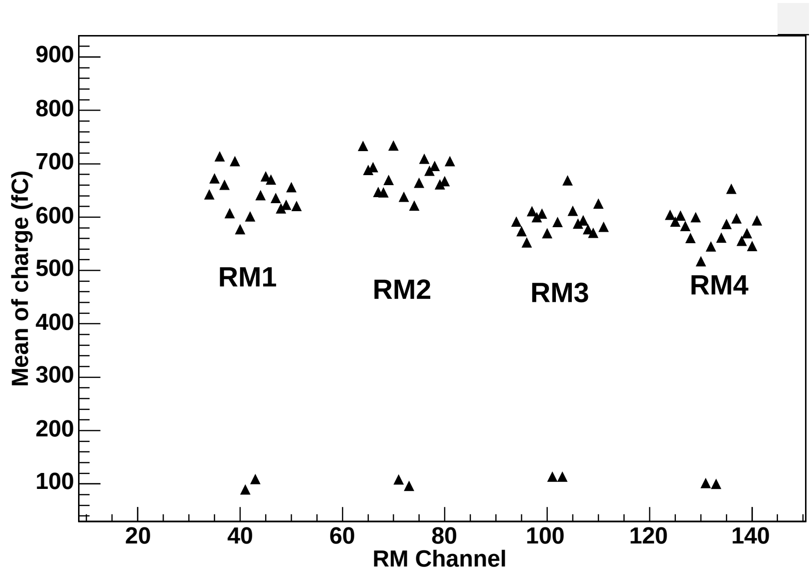

Figure 4.28: Output of Burn-in test for the HO RMs.

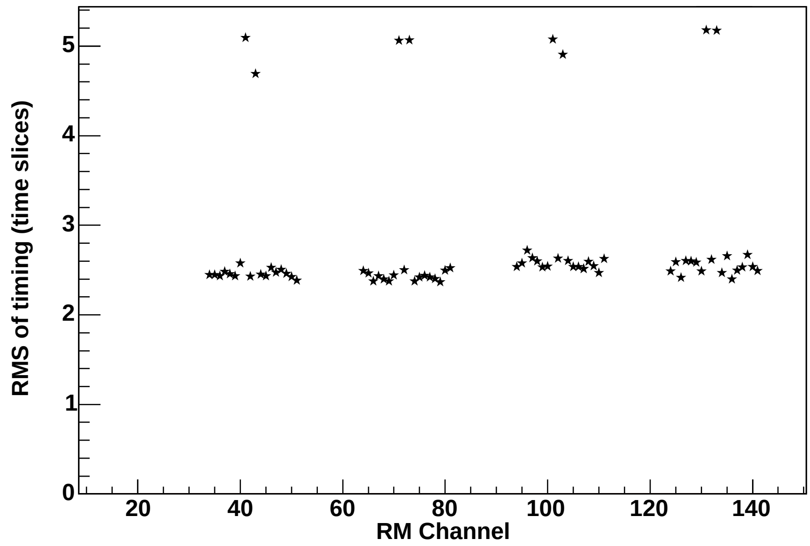

Figure 4.29: The root mean square (RMS) values for the signal mean charge.

4.7.5 Quality Control and Assurance

The response of RM's are checked for its consistent response on a single RBX shell with actual lengths of HV, LV and calibration cables. The light source chosen for this purpose is LED which can have different intensities. The bias current and voltage of each RM of the particular RBX are checked.

4.7.6 Burn-in Test

It is essentially to check the long term operation stability of the RBX, bias current, voltages and temperatures (CCM, CM, RM etc.) are monitored as shown in Figures 4.28 and 4.29 for about a week at HV=10 KV and each day the LED run was acquired.

4.8 Honeycomb Support for HO

There is maximum of 40 mm of clearance for placing the HO trays together with the hanging support for HO. Each tray with all its packing is expected to have a thickness of 15.44 mm. This necessitated a space of $17.0^{+0.2}_{-0.0}$ mm for inserting trays. The total weight of a ϕ sector (six trays) is expected to be 30.0 kg. To support the weight , a possible design was to have a pair of aluminum honeycomb supporting panels clamped between these C-channels on the two sides and one end keeping the other end open for inserting the trays.

The hanging structure is made of aluminum honeycomb panels of thickness 10 mm for the bottom and 6 mm for the top. The top and bottom panels are put together with 20 mm $\times$ 40 mm aluminum C-channels glued by araldite in the 3 sides from outside and a set of twelve 20 mm $\times$ 20 mm aluminum C-channels glued on the inner side screwed using countersunk screws at the separation of trays. The trays can be inserted with utmost care at these separations. The panels of rings ± 1 and ± 2 also carry cooling tubes on one side. These serve as thermal screens to prevent heat percolation to the RPC/muon chamber

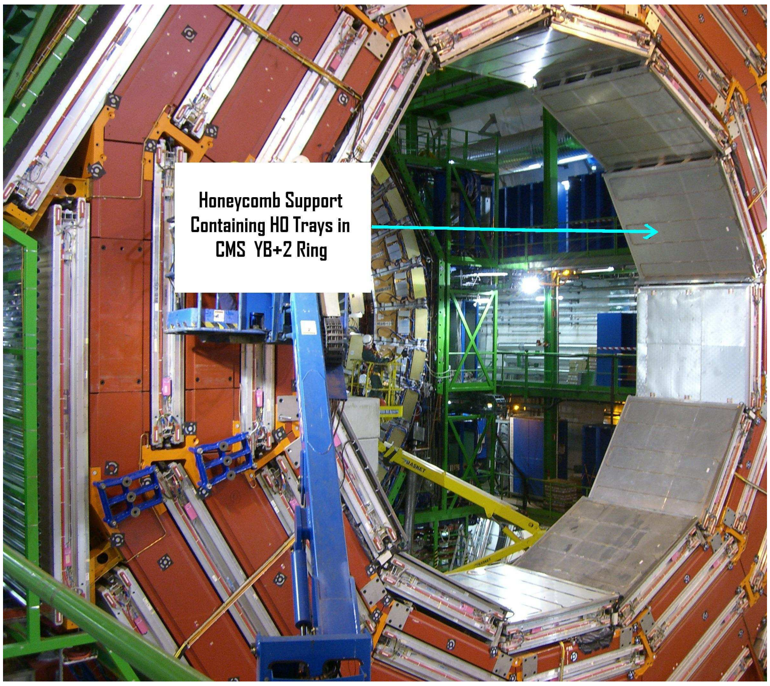

Figure 4.30: Honeycomb panels being installed in the CMS detector with fully loaded HO ring +2 trays.

assembly. The cooling tubes are made of copper and have inner and outer diameter of 6 mm and 8 mm. These are glued to the 6 mm thick honeycomb surface using araldite and fixed with copper collars. For ring $\pm$ 1 a special panel is built to accommodate the short trays due to the chimneys. These panels have been tested for with standing a much higher pressure than they are expected to hold. Fig. 4.30 shows ring +2 honeycomb panel with fully loaded HO trays.

4.9 Summary

CMS HCAL is a sampling calorimeter with brass absorber and plastic scintillator tiles. The HB is complimented with HO to ensure high energy shower containment in CMS HCAL. The light produced in the scintillator is carried out primarily by wavelength shifting fibers (WLSs). Clear fibers are spliced to the WLS fibers and used to guide the captured light to HPDs, where the light is transformed into electric pulses. Pulses are then amplified and converted into digital signals and sent through optical links to know the $\eta - \phi$ distribution of energy. The HPD's, preamplifiers and charge integrating ADC's (QIE) are all situated in readout boxes (RBXs) on the outskirts of HO detector layer. Panjab University, Chandigarh and TIFR, Mumbai took independent responsibility for the complete HO detector fabrication. Testing of the assembled HO scintillator modules was done using cosmic test for the output in terms of number of photoelectrons. Radioactive wire sourcing and X-Y scanning was done to inter-calibrate scintillator tiles of the assembled HO module with respect to each other. Installation of HO in to the CMS detector is done after HO Modules were tested at CERN for cross checking any damage during shipment from India to CERN. The HO readout boxes were also tested using Burn-in test. An active participation and significant contribution was made in all above mentioned activities including complete fabrication, testing and installation of HO in to the CMS detector.

Bibliography

[1] CMS Hadron Calorimeter Technical Design Report, CERN/LHCC 97-31.

[2] V. V. Abramov et al., Studies of the Response of the Prototype CMS HAdron Calorimeter, Including Magnetic Field Effects, to Pion, Electron, and Muon Beams, CMS NOTE 2000/003, Nucl. Instrum. Methods Phys. Res., A 457 (2001) 75-100, hep-ex/0007045.

[3] Sunanda Banerjee and Sudeshna Banerjee, Performance of Hadron Calorimeter with and without HO, CMS NOTE 1999/063.

[4] B. S. Acharya, A. Kumar, S. B. Beri, J. M. Kohli et al., The CMS Outer Hadron Calorimeter, CMS NOTE 2006/127.

TIFR/CMS-99-01.

[5] Ashok Kumar, Suman Beri, J. M. Kohli et al., (India CMS Collaboration), Fabrication of outer hadron calorimeter scintillator module for CMS detector, proceedings of XV DAE HEP symposium, Nov. 2002, University of Jammu, Jammu, India.

[6] V. K. Bhandari, Suman Beri, J. B. Singh, Fabrication of Scintillation Counters and Testing Techniques using Cosmic Ray set up and Data Acquisition, Concepts and Methods of High Energy and Nuclear Physics, p. 174, proceedings of V SERC school on Experimental High Energy Physics, March 2005, Panjab University, Chandigarh, India.

[7] B. S. Acharya et al., Optical fiber scanning apparatus, TIFR/CMS/97-2.

[8] Outer Hadron Calorimeter (HO) Engineering Design Review Note,

[9] E. Hazen et al.,Radioactive source calibration technique for the CMS hadron calorimeter, Nucl. Instrum. Methods Phys. Res., A 51 1 (2003) 311-327.

[10] Ashok Kumar, Suman Beri, J. M. Kohli et al., (India CMS Collaboration), Quality Control Check and Testing of Outer hadron calorimeter Scintillator Module for CMS detector, proceedings of XV DAE HEP symposium, Nov. 2002, University of Jammu, Jammu, India.

Chapter 5

CMS HCAL Test Beam

The scintillators with the WLS fibers are the active medium of the hadron calorimeter (HCAL). In order to attain the required HCAL resolution and maintain this value over the 10 year lifetime of the detector, the scintillators and WLS fibers have to meet stringent material specifications. The energy of the particles in the calorimeter is measured by the amount of light that reaches the photo detector. The criteria are developed so that a minimum ionizing particle (MIP) produce nearly the same amount of light no matter where it crosses the scintillator in a tower. The baseline for the HB/HE detectors is the Kuraray SCSN81 scintillator (polystyrene based plastic) and the Kuraray Y11-250 double clad (WLS) fiber. The HB and HE tiles are substantially larger in size with the lower light yield. For these tiles, a higher light yield is required so that minimum ionizing particles can be observed. The baseline is Bicron BC408, for which the plastic base is polyvinyl toluene (PVT), produces more light than SCSN81 with 10 mm thickness. The WLS fibers are the same as for the HB/HE calorimeters. HO is also made up of Bicron BC408 scintillator and WLS fibers spliced with clear fibers are used as readouts.

The HCAL test beam study helps to understand the performance of the CMS hadronic calorimeter in measuring energies of single electrons, pions and muons. It helps in calculating preliminary calibration constants which can be used in simulation and reconstruction softwares. It also helps in directing trigger related algorithms for physics analysis. The test beam data allows us to evaluate and study the physics potential of the HCAL detectors including HO as a hadronic tail catcher and muon triggering counter.

5.1 The CMS Calorimeter System

A calorimeter is an experimental apparatus that measures the energy of particles. Most particles enter the calorimeter and initiate a particle shower and the energy of the particle is deposited in the calorimeter, collected and measured. The energy may be measured in its entirety, requiring total containment of the particle shower, or it may be sampled. Typically, calorimeters are segmented transversely to provide information about the direction of the particle or particles, as well as the energy deposited, and longitudinal segmentation can provide information about the identity of the particle based on the shape of the shower as it develops.

The CMS calorimeter system comprises of electromagnetic and hadronic calorimeters. The electromagnetic calorimeter of CMS at the LHC has been designed to measure the energy of electrons and photons with high resolution over a wide energy range. It consists of over 80,000 lead-tungstate $PbWO_4$ crystals equipped with avalanche photodiodes or vacuum phototriodes and associated electronics operating in a CMS environment.

CMS has four kinds of hadronic calorimeters which provide good segmentation and hermeticity, moderate energy resolution, and full angular coverage up to η=5. The barrel hadronic calorimeter (HB) [1] surrounds the electromagnetic calorimeter, and covers the central pseudorapidity region up to η=1.3. The end regions are covered up to η=3 by the two endcap hadron calorimeters (HE) [2]. The pseudorapidity coverage is extended up to η=5 with the two forward calorimeters (HF) [3], which surround the beam pipe 11 m from the interaction point. The HB and HE are located inside a 13 m long 4 T solenoid magnet. The Central shower containment is improved with scintillators added outside the magnet, known as outer hadron (HO) calorimeter.

5.2 HCAL Test Beam Experiment

The hadron calorimeter (HCAL) test beam 2003 and 2004 studied the performance of the CMS hadronic calorimeter in measuring energies of single electrons, pions and muons. One of the goal of a test beam is to acquire beam and calibration data for different energies. The HCAL detectors were exposed to charged particles such as electrons, muons and pions in different configurations. The detectors are also exposed radioactive-source and LASER runs for the calibration purpose. This data set allows the evaluation and study of the physics potential of the HCAL as well as directing the development of trigger-primitive generation algorithms. More than 100 million events were read out with at 29.6 ns period [4], slightly longer than the 25 ns planned for CMS. A total of 144 HB channels (two wedges) and 16 HO (ring 0, 1, and 2 trays) channels were tested in a detector configuration which included an aluminum slab, representing the solenoid material, and a mock-up of the electromagnetic calorimeter (ECAL).

The beam is fixed to the laboratory frame, and a motion table is used to change the relative direction of the beam with respect to the detector. This allows the beam to test different detectors as a function of η and ϕ. The arrangement of the CMS detectors at motion table are shown in Fig. 5.1. The beam line is equipped with wire chambers and scintillator tiles to trigger the events and monitor the beam position. The detector includes a mock-up of the ECAL, consisting of an aluminum box which contains a $PbWO_4$ crystal 7×7 matrix. The front-face dimensions are 2.2×2.2 cm^2 and the crystal length is 23 cm. The box containing ECAL crystals may be translated and rotated for the beam to run along any of the 49 crystals. Two avalanche photodiodes (S8148 from Hamamatsu) are glued to the back of the crystal. The ECAL box is followed by two HB wedges positioned together as in the real CMS setup. The HB calorimeter is a scintillator and brass sandwich calorimeter with a segmentation of $(\Delta\eta, \Delta\phi) = (0.087, 0.087)$. The absorber consists of 40 mm thick front steel plate followed by eight 50.5 mm brass plates, six 56.5 mm additional brass plates and a 75 mm thick steel back plate. In front of the front steel plate, a 9

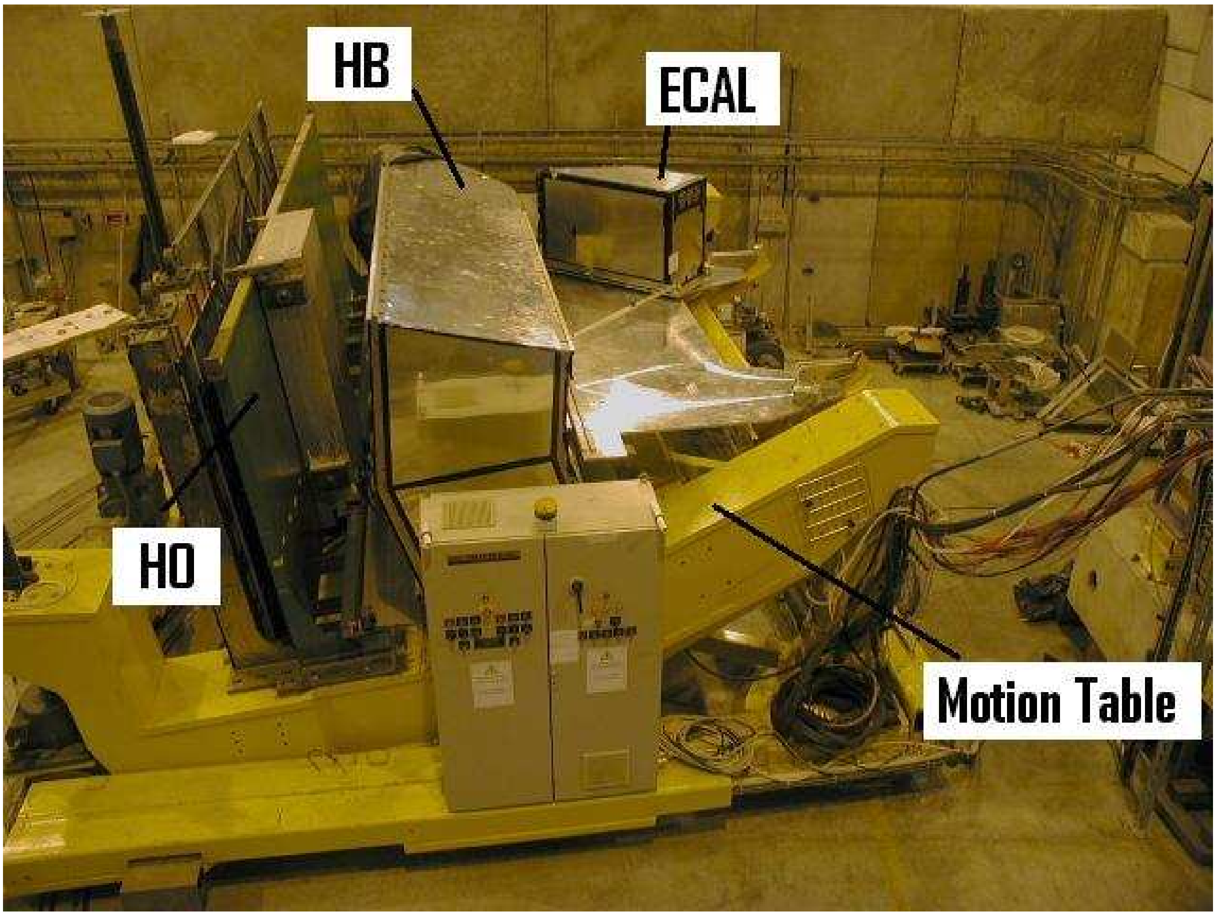

Figure 5.1: CMS detectors including ECAL prototype and HCAL detectors (HB wedges and HO trays) are shown at motion table used in the test beam.

mm thick scintillator (Bicron BC408) is placed. The scintillators between brass plates are 3.7 mm thick (Kuraray SCSN81). The last scintillator plate is also 9 mm thick (Bicron BC408) [5]. An aluminum slab accounts for the solenoid material and precedes the HO. The HO depicted in Fig. 5.2 consists of scintillators modules called trays and acts as a hadron tail catcher. The inner layer consists of only one panel (ring 0 covering the central η region), and the outer layer of three panel (rings 0, 1, 2 covering a larger η range). For the HB and HO, the light from the scintillators is transported to the hybrid photo diodes (HPDs) through clear fibers. The signal is then processed by the Charge Integration Electronics (QIE) which gives a short output pulse.

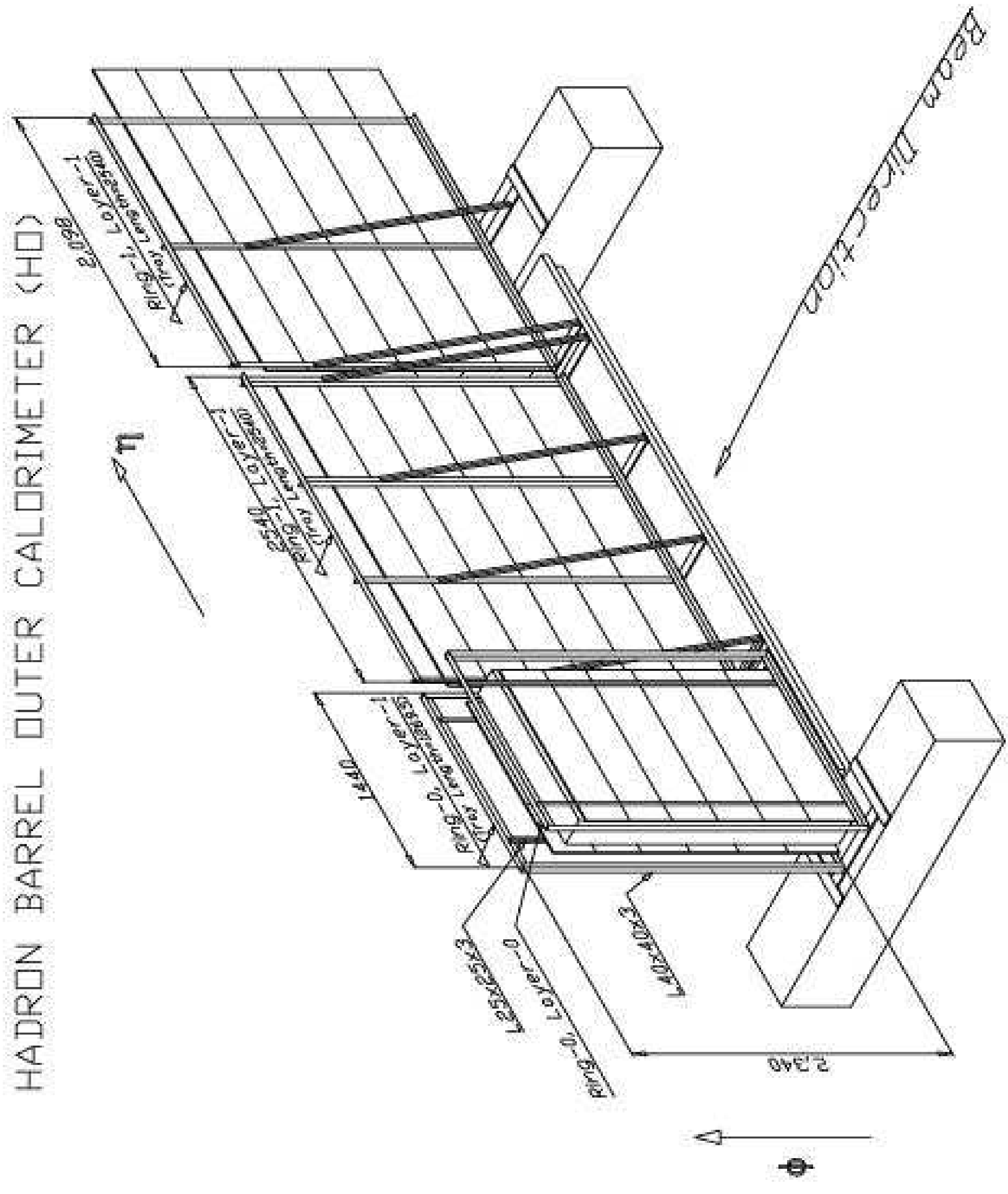

Figure 5.2: Diagrammatic view of the HO scintillator trays in the test beam.

5.2.1 H2 Beam Line

The beam line is designed to operate in two distinct modes. In the high energy mode, various particles are produced when 400 GeV/c protons from the Super Proton Synchrotron (SPS) strike a production target (T2) 590.9 m upstream of the calorimeters and particle momenta range is between 10 GeV/c to 350 GeV/c. In the very low energy (VLE) mode, an additional target is used for particle production and the momenta of particles are limited 1 to 9 GeV/c. The maximum usable beam momentum was 100 GeV/c for electrons and 350 GeV/c for hadrons.

5.2.2 Beam and Run Conditions

The test beam experiment included an energy scan of ECAL-HB configuration with energy range of 30, 50, 100, 150, 300 GeV to measure pion energy resolution and response. The pion beam was directed onto specific tower, and the ECAL system translated and rotated so that the beam passed through the central crystal of the ECAL 7 $\times$ 7 matrix. The ECAL crystals were calibrated relative to each other using a wire source. The high voltage was adjusted to equalize the crystal to crystal response to within a factor of two. The final calibration was performed with 100 GeV electron beams directed towards the center of each crystal. The electron energy was reconstructed from the energy depositions in a 5 $\times$ 5 crystal matrix centered around the targeted crystal, which contained most of the shower energy.

The individual calibration factors for each crystal were determined by iterating simultaneously over the 49 crystals. The energy scale of the HB was derived in the test beam 2003 experiment in several steps. First of all a Cs^{137} source was used to calibrate the individual scintillator tiles to make the detector uniform. Secondly, a beam of 100 GeV electrons was directed onto a given HB tower to provide an estimate of the ADC counts to GeV conversion factor. In the third step, a beam of 50 GeV pions were directed to the ECAL-HB configuration. Only those pions which showered late, that is they deposited less than 2 GeV in the crystals and most of their energy in the HB, were selected. The calibration factor was extracted from the ratio between the initial pion energy and the mean of the sum of the energy depositions in the scintillators associated with a 5 × 5 tower matrix around the target tower.

5.2.3 HCAL DAQ Software

The 2003 HCAL test beam DAQ is based on the XDAQ toolkit developed by the CMS DAQ group as a common set of tools for creating a data acquisition system. The XDAQ toolkit provides methods for communication between modules of a DAQ system and for managing memory for those communications.

The test beam has demonstrated that the structure of the HCAL readout/DAQ is functional and giving adequate performance. The development of HCAL DAQ code needed for test beam 2004 was built directly on the code base developed in 2003. The HCAL DAQ code needed to follow developments in XDAQ as well as the arrival of the CMS-wide run control and monitoring solution, RCMS.

5.3 Data Sets Collected

Several data sets were recorded during HCAL test beam in H2 beamline at CERN in 2003 and 2004. The main task performed in CMS HCAL test beam were

1. Calibration of ECAL crystals (using wire-source, and electron beam).

2. Calibration of HCAL detectors (using wire-source and muon beam).

3. Energy scan using very low energy (VLE) and highly energy pions.

4. To see the longitudinal particle shower profiles in the calorimeters.

5.4 ECAL Calibration using Electron Beam

The task of the ECAL is to measure the energy and location of the electromagnetic showers and to contribute to the measurement of hadron showers and missing energy in combination with the HCAL. The test beam calibration provides calibration constants for the ECAL+HCAL shower studies. Also, for an accurate calibration of the CMS hadron calorimeter (HCAL), influence of ECAL must be fully understood and accounted for. Enumeration of crystals started from the left-upper crystal when looking from a beam direction and is shown in Fig. 5.3.

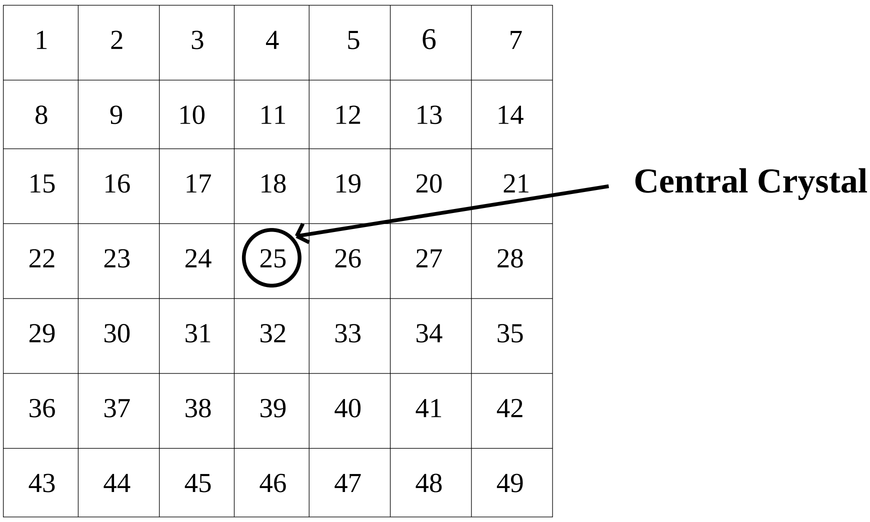

Figure 5.3: Enumeration of ECAL crystals used in CMS HCAL test beam.

There were two ways of recording data for the ECAL calibration process [6]. By using a well focused beam, with transverse size of 1×1 cm^2, all electrons were hitting one particular crystal (called central). In a second method the beam was strongly defocussed so that, in a single run, electrons were hitting many crystals, usually situated in 4×4 matrix around central. Fig. 5.4 shows a shape of the beam in sample run. In this method it was necessary to find which crystal was hit by a particular electron and treat this crystal as central.

The charge of the phototube signals was integrated in charge to digital converter

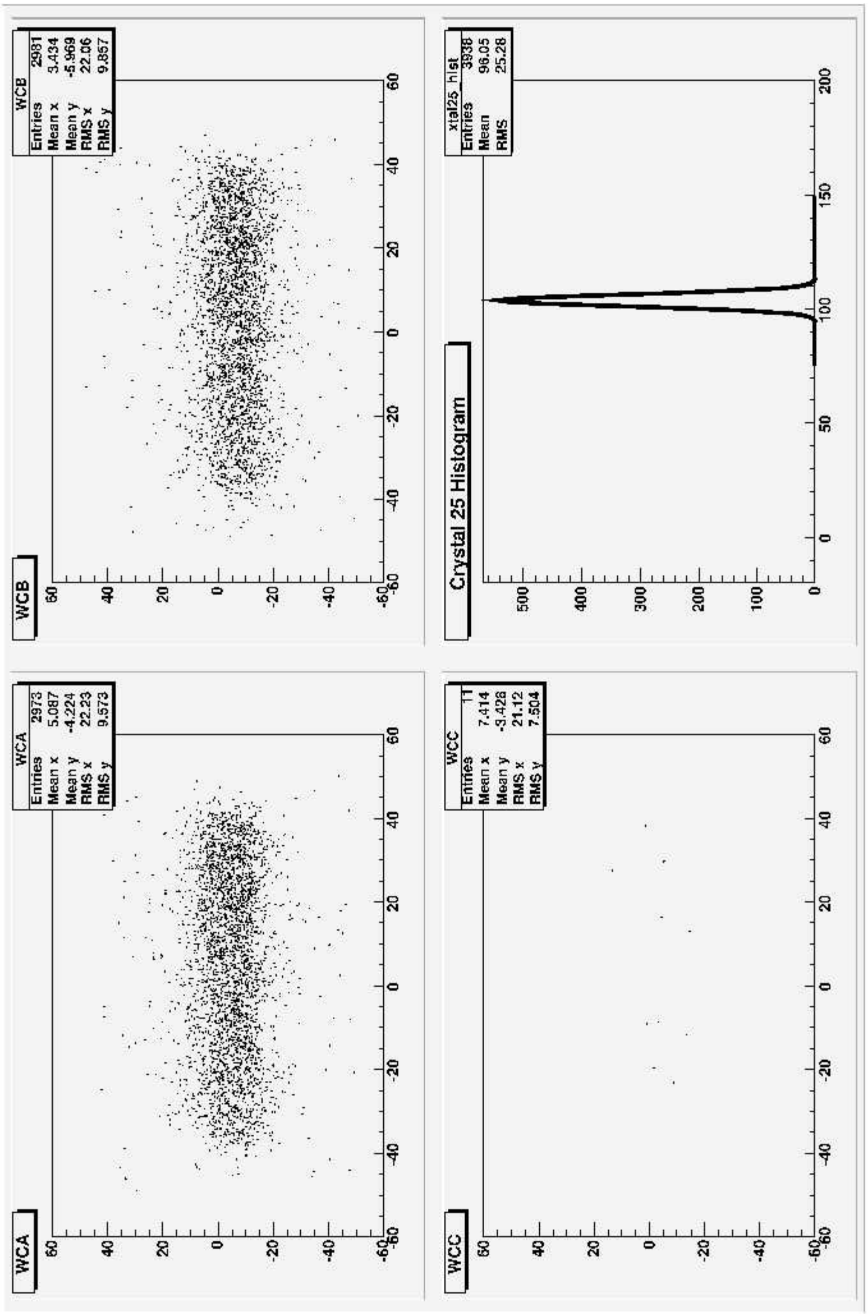

Figure 5.4: Wire chambers (A, B and C) showing the shape of beam. Plot also shows the energy distribution of ECAL central crystal for 100 GeV electron beam.

(QDC) and corresponded to the energy of a particle incident on a crystal. Because of electronic noise, including the phototube, QDC values were present, even without a particle signal. This value is called the pedestal. During the 2003 test beam the pedestals were measured for each run individually using random triggers recorded during the SPS spill (in spill pedestals). With pedestals subtracted from the QDC output, we were ready to convert them to energies. To do so, the pedestal subtracted QDC counts were divided by the conversion factor to obtain a value in GeV i.e.

$$E = \frac{QDC}{g} \tag{5.1}$$

where E is the energy in GeV, QDC is the value from a particular crystal and g is the conversion factor. If a single electron of known energy were completely contained by a single crystal, then the conversion factor would be easily obtained using this equation alone.

The g_i values were obtained in an iterative process. The initial values were set to 10 because the raw QDC values were ranging around 1000 counts for 100 GeV electrons. For each 3x3 array, the energy for each crystal was calculated using the current values of gains. Then, looping over all events, histograms for each crystal were filled. Assuming that each crystal sees approximately the same energy distribution we can obtain a measurement of this observed energy by a gaussian fit. The mean of this fit should be equal to the beam energy. In case it is not we can re-scale the gains to make the mean equal to the expected energy. For the first iteration:

$$g_j^{new} = \tfrac{<E_j>}{100} g_i^{old}$$

where ‘j’is the index of crystal, changing from 1 to 49.

This iteration process was not always successful, especially if the initial gain was far off the actual value or if there was a lot of energy sharing between crystals. When this happened it was necessary to intervene manually. For border crystals this procedure was less precise. The reason is obvious since some of the particles created in a shower were leaking out of ECAL and the electron energy was not fully contained.

5.4.1 Cuts used

A number of cuts had to be applied to the data to get clean energy sum distributions. These include:

- **Seed cut**: Histograms were filled only if a particular crystal had the highest 3×3 energy in the 7×7 matrix. Fig 5.5 shows the histogram after seed cut on crystal no. 25.

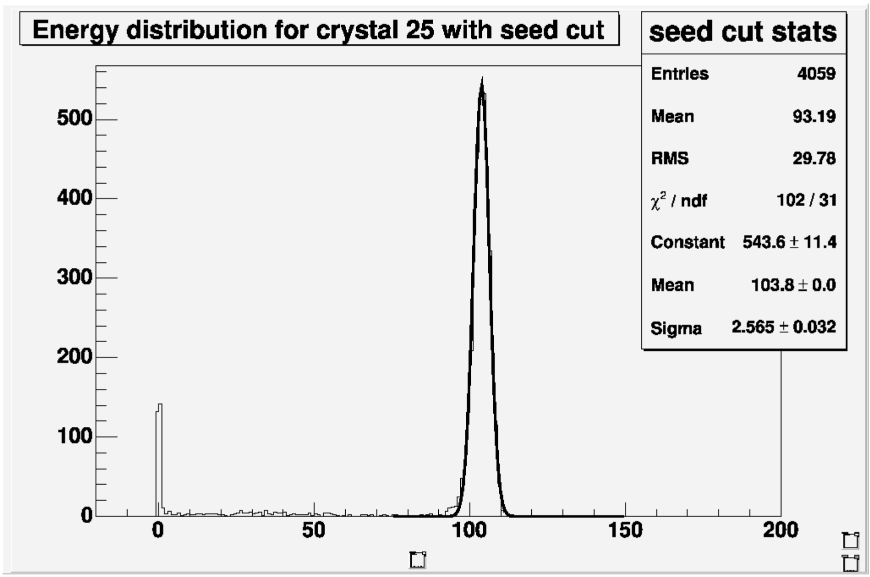

Figure 5.5: Energy distribution of the ECAL central crystal for 100 GeV electron with seed cut.

- **Energy cut**: Events with 3×3 energy which was lower than 50 GeV or higher than 150 GeV were removed. This cut excludes events triggered by muons or two electrons hitting the seed crystal at the same time. It also excluded events with energy leakage.

- **Fraction cut**: Fraction cut variable was defined as the energy in the seed crystal divided by the 3 $\times$ 3 energy around it. This cut was excluding events in which particles were hitting border of the seed crystal. If an electron doesn't hit exactly in the center of the seed crystal, energy would be contained in a bigger matrix. To check this, a new variable was defined as energy in central crystal divided by energy in 3 $\times$ 3 matrix. This ratio described the percentage of the electron energy collected in the central crystal. Fig. 5.6 shows the histogram after f1 cut.

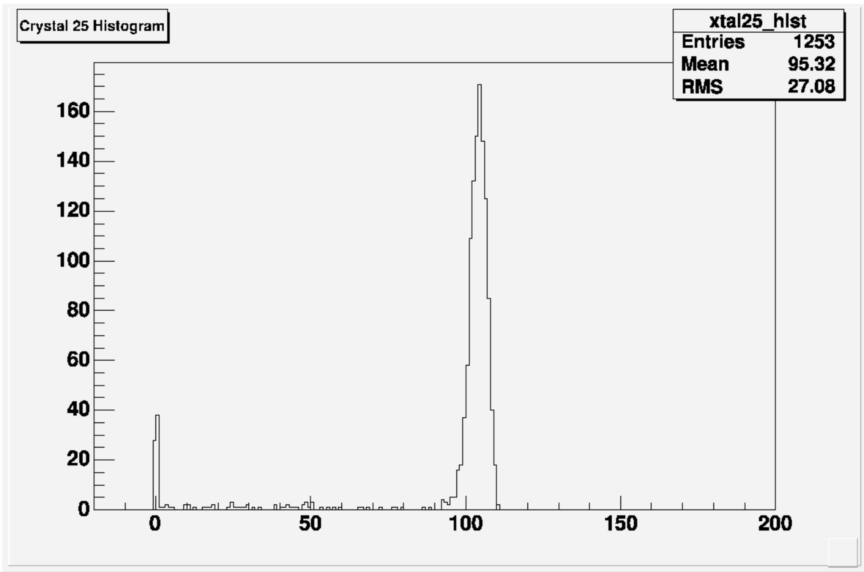

Figure 5.6: Energy distribution of the ECAL central crystal for 100 GeV electron with f1 cut.

Fig. 5.7 shows the energy distribution after all cuts [7]. Fig. 5.8 shows the response of the crystal no. 25 after getting the good calibration constant after the iterations.

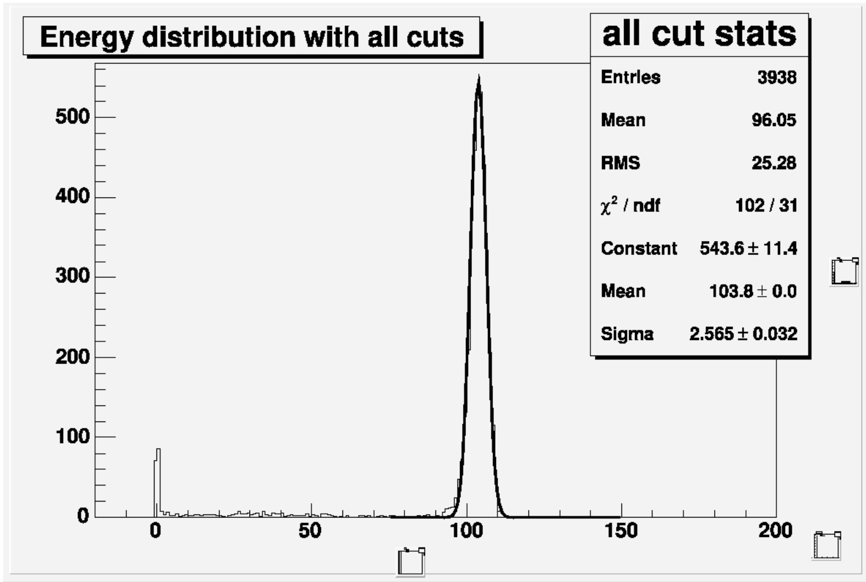

Figure 5.7: Energy distribution of the ECAL central crystal for 100 GeV electron after all cuts.

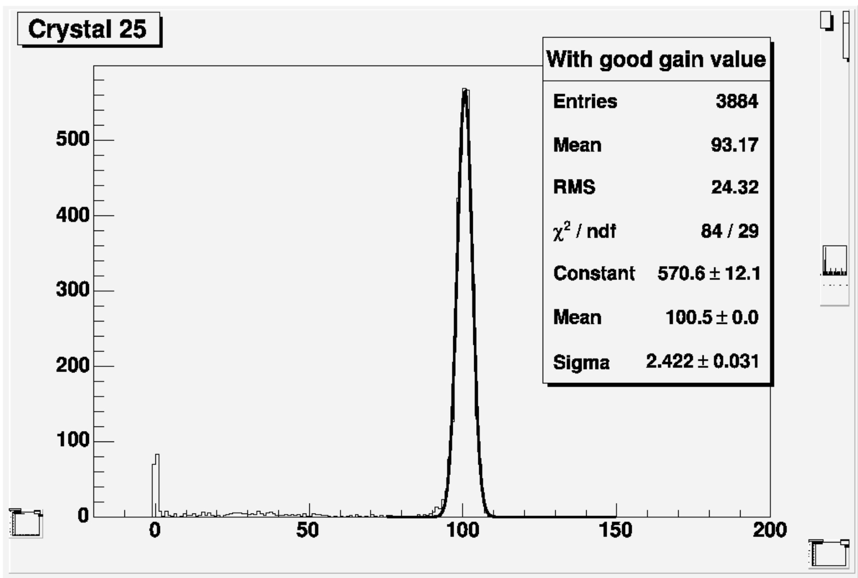

Figure 5.8: Energy distribution of the ECAL central crystal for 100 GeV electron after using good gain value obtained through iteration process.

5.5 ECAL Response to Test Beam

Electromagnetic showers developing inside crystals are mostly contained in a 3 × 3 matrix of crystals centered around target crystal. Thus the energy (E) deposited by electrons in ECAL is defined as:

$$E_{ECAL} = \frac{1}{Normalisation\ constant} \times \sum_i^{49} ADC_i \times Tower\ weight_i$$

In the above equation ADC_i is the pedestal subtracted ADC value of the particular tower. The Normalization constant is found using data from 100 GeV electron run. The sum can represent 9 central towers (3 × 3) as shown in Fig. 5.9 or 25 central towers (5 × 5) as shown in Fig. 5.10 or all 49 towers (7 × 7) as shown in Fig. 5.11.

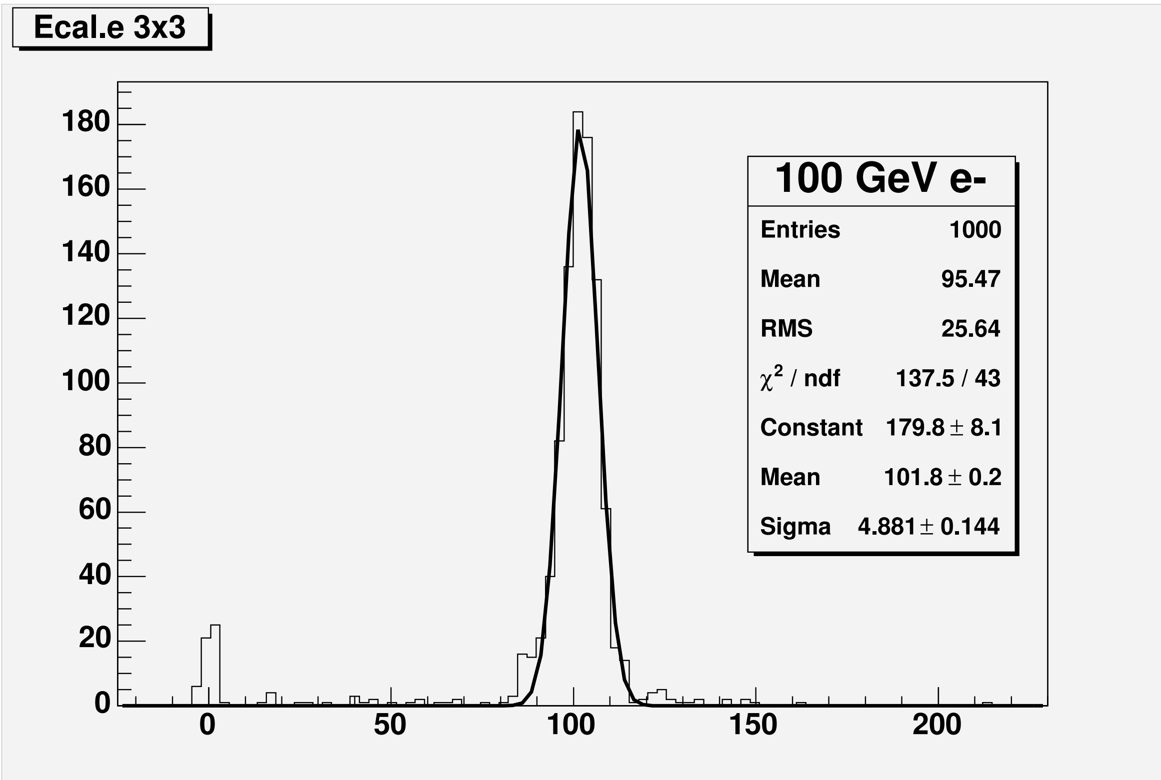

Figure 5.9: Energy distribution for 100 GeV electron by using ECAL (3 × 3) crystal matrix.

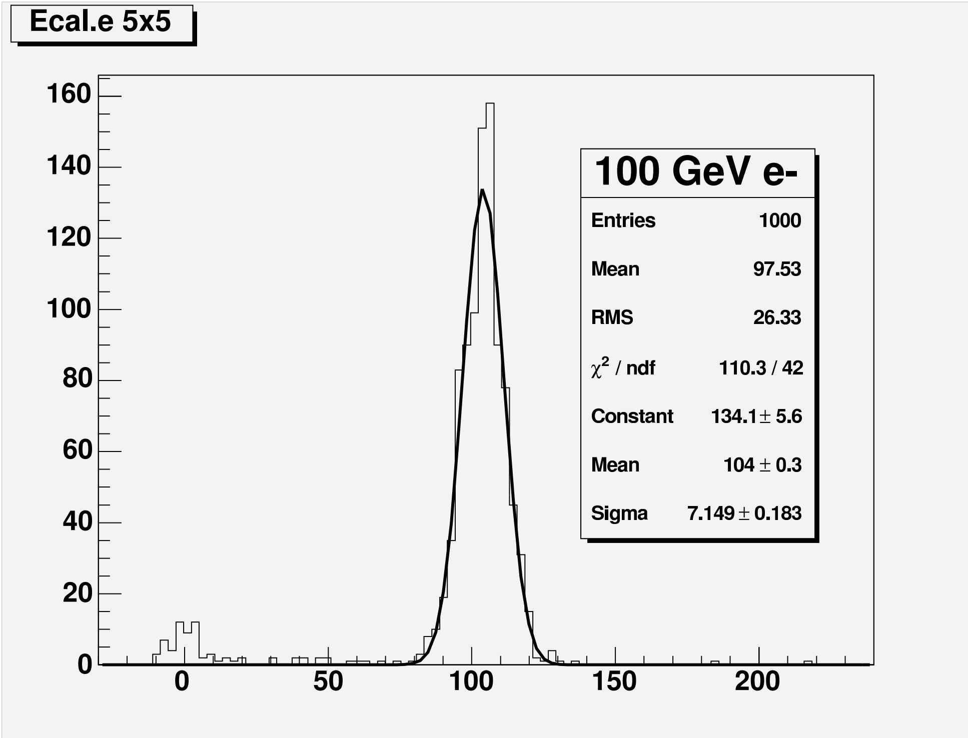

Figure 5.10: Energy distribution for 100 GeV electron by using ECAL (5 $\times$ 5) crystal matrix.

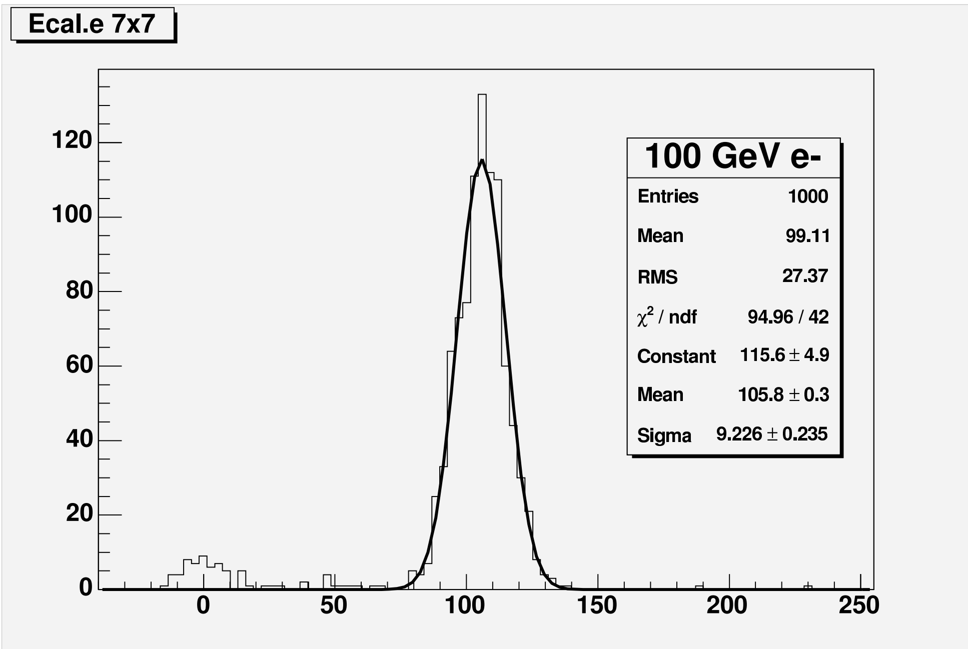

Figure 5.11: Energy distribution for 100 GeV electron by using ECAL (7 $\times$ 7) crystal matrix.

Normally for electrons a (5 × 5) energy sum is sufficient to calculate the energy properly. The (7 × 7) sum adds only to the width of the distribution. The energy distribution for 50 GeV and 150 GeV electrons in ECAL are shown in Figures 5.12 and 5.13 respectively.

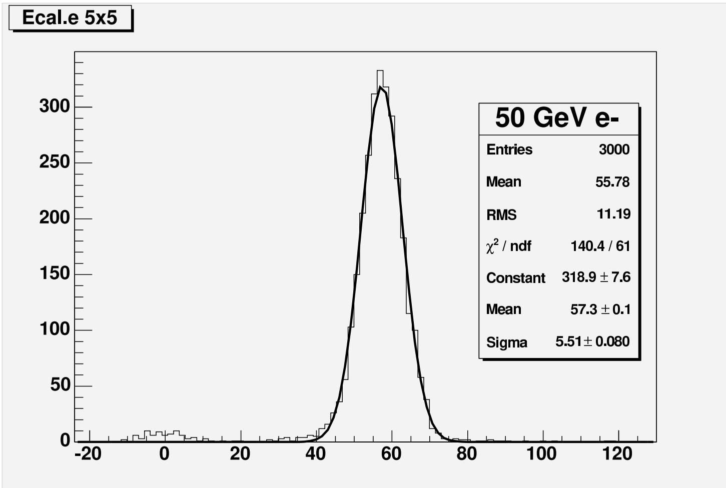

Figure 5.12: Energy distribution for 50 GeV electron by using ECAL (5 × 5) crystal matrix.

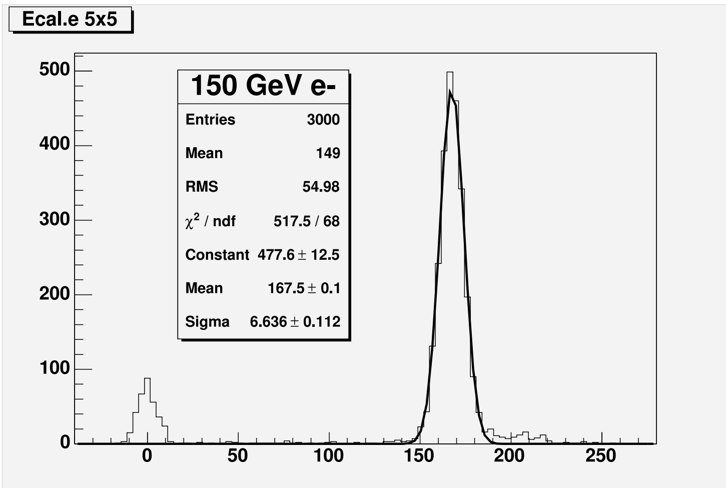

Figure 5.13: Energy distribution for 150 GeV electron by using ECAL (5 × 5) crystal matrix.

Fig. 5.14 shows the linearity response of ECAL i.e. variation of electron energy response (Measured energy vs. beam energy) with beam energy in the ECAL. The resolution is calculated as the measured sigma per fitted mean of the electron energy distribution. Fig. 5.15 shows variation of energy resolution with electron beam energy in the ECAL. The ultimate limit for the energy resolution of a calorimeter is determined by fluctuations inherent in the development of showers, and by instrumental and calibration limits.

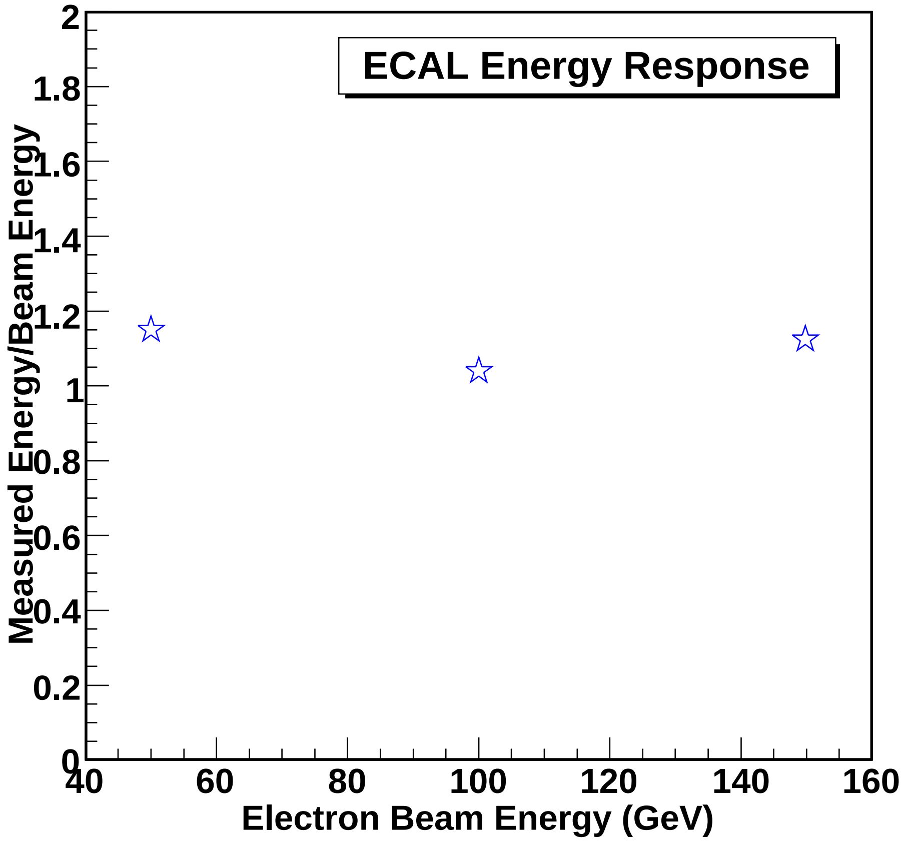

Figure 5.14: Variation of electron energy response (measured energy vs. beam energy) with beam energy in the ECAL.

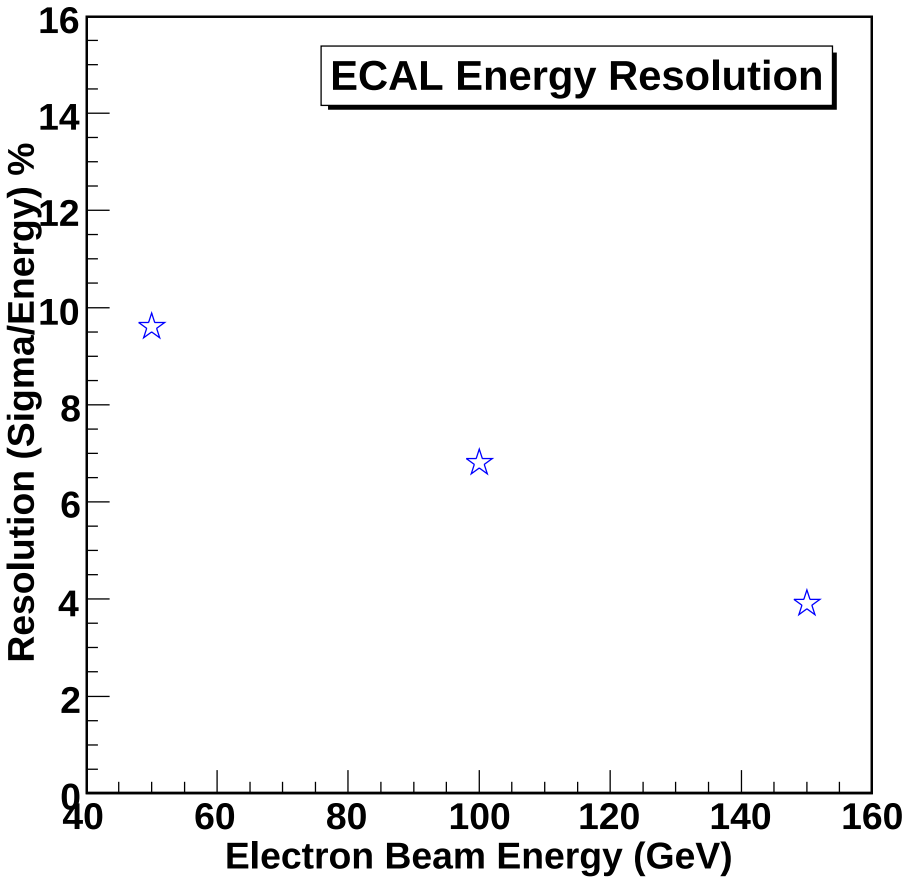

Figure 5.15: Variation of energy resolution with electron beam energy in the ECAL.

5.6 HCAL Calibration and Monitoring

The uniformity of response must, to first order, be assured by the construction and quality control. The assembly can be monitored by radioactive source and by injecting light from UV lamps. There are several complementary calibration and monitoring methods. While we use the radioactive sources for calibration, the LED and lasers are typically useful for front-end electronics debugging and monitoring.

5.6.1 Calibration with Cs^{137} Source

All layers of the hadron calorimeter are equipped with thin stainless tubes that route radioactive sources throughout the system [8]. A wire with a point-like Cs^{137} source is pushed through these tubes by a remotely controlled system of drivers. The DC current induced by the source traversing one tile of a tower provides an accurate measurement of the response of the entire measuring chain. The change of response due to photodetector or electronics show up as a change of the response of all tiles of a given tower and can be compensated by an adjustment of the overall calibration factor. Change of response due to radiation damage leads to a change of the measured current that is dependent on the depth of the layer. The HB wire source output as shown in Fig. 5.16 clearly depicts the signal in the active detector layer of the sampling calorimeter.

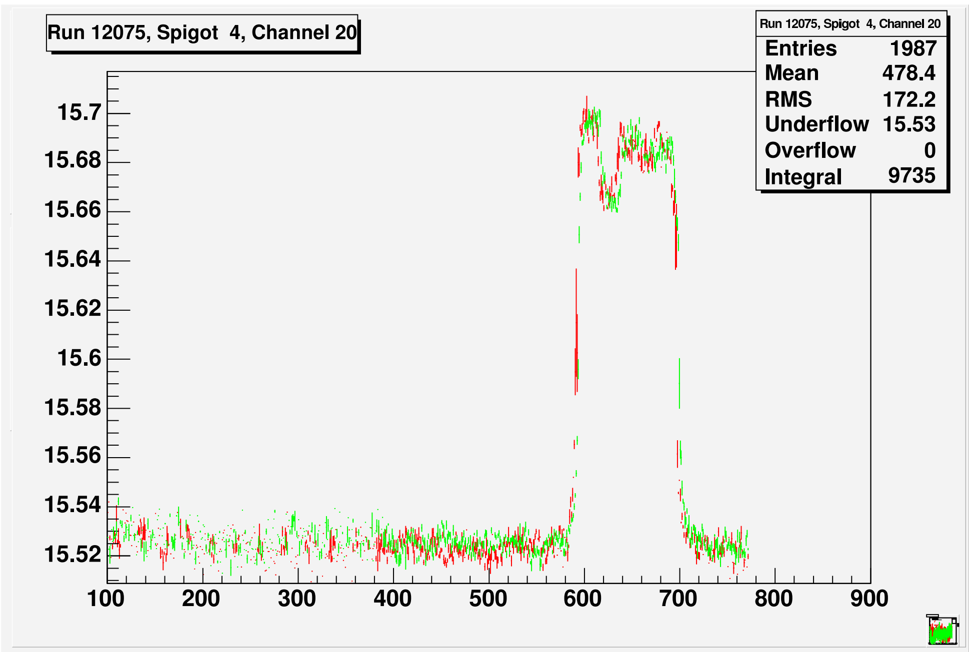

Figure 5.16: The HB wire source output. It clearly depicts signal when wire source traverses in the active detector material of the sampling calorimeter.

5.6.2 Using Muon Beam

The calibration of the HCAL (HB & HO) tiles were performed using the minimum ionizing particle (MIP) or muon beam. The calibration of HO towers were done for each tower. To calibrate each HCAL tower 150 GeV muon beam is used and the pedestal subtracted signal ADC distribution is plotted for each longitudinal segment of a tower [9]. The signal ADC distribution is fitted to gaussian and the peak of the gaussian is taken as the MIP response of the scintillator tile of tower and can be used as normalization constant in case of pion runs. If due to low gain of the HPD, the peak of the signal is not clearly visible, then the mean of the muon ADC distribution is taken as the MIP value. These values of all the channels are stored in separate file and is used to calibrate the towers for pion runs.

The signal and pedestal for 150 GeV muon, shown in Fig. 5.17, suggests that pedestal is slightly overlapping with signal for HO. The overlapping is more for far off ring 2 and is least for central ring 0 because it is having two layers. So one had to be careful while subtracting pedestal from the signal for different HO rings.

5.7 HCAL Response to Test Beam

The HCAL surrounds the ECAL and acts in conjunction with it to measure the energies and directions of particle jets, and to provide hermetic coverage for measuring missing transverse energy. The pseudorapidity range ($|\eta| < 3.0$) is covered by the barrel and endcap hadron calorimeters which sit inside the 4 T field of the CMS solenoid. In the central region around $\eta = 0$ a hadron shower 'tail catcher' is installed outside the solenoid coil to ensure adequate sampling depth. The active elements of the barrel and HE consist of plastic scintillator tiles with wavelength-shifting (WLS) fiber readout. The layers of these tiles alternate with layers of copper or stainless steel absorber to form the sampling calorimeter structure. The tiles are arranged in projective towers with fine granularity to

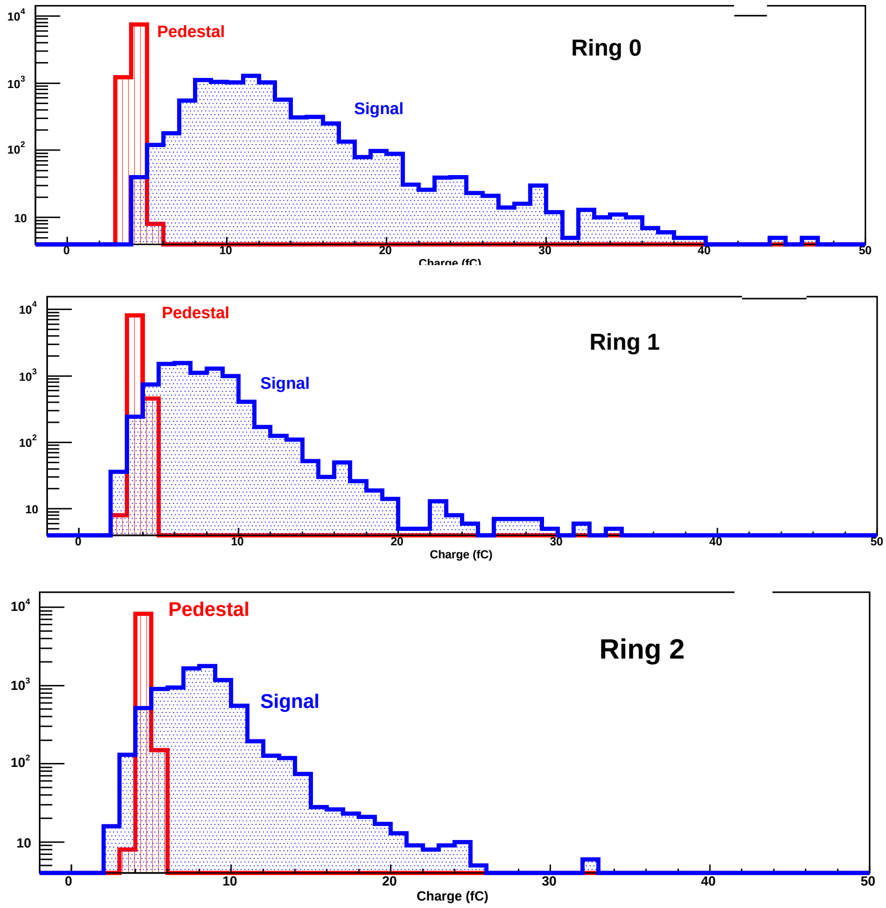

Figure 5.17: The signal and pedestal distribution for HO trays exposed to 150 GeV muon in the test beam. There is a significant signal overlapping with the pedestal for different HO rings.

provide good di-jet separation and mass resolution. The choice of lead tungstate crystals as the active element of the ECAL influences the HCAL design and performance. The optimization of the HCAL/ECAL combination requires prototype work in test beams. Studies using a realistically sized HCAL prototype are also required to study the effect of cracks and dead areas that may be introduced when building a 4π calorimeter. For these prototypes to be realistic it is essential that the mechanical design be fully developed, taking into account the need for hermetic calorimetry and the provision of supports for inner elements of the CMS detector.

5.7.1 Energy Distributions for Pions

One of the two HB wedges was configured according to the normal CMS design, called HB1, such that light from all the scintillator tiles in each tower were summed optically and routed to one pixel of an HPD photo detector. Thus, the configuration has only transverse segmentation. The pion beam in the test beam 2003 experiment contained a significant amount of contamination, or background, coming from residuals of the pion production process, and scrapping along the beam line. With ECAL+HB+HO configuration, The HCAL energy versus ECAL energy stands for the fraction of the pion energy deposited in an HB 5x5 tower matrix or a 5x5 crystal matrix in the ECAL box, centered about the direction of the beam. The large concentration of events in the area of low HCAL and ECAL energy correspond to the muon background (also called minimum ionizing particles or MIPs), while the electron contamination populates the region of low HCAL energy and covers a broad ECAL energy range. The way to determine the pion energy distributions was to reject the background by means of cuts in the HCAL energy versus ECAL energy plane. Fig. 5.18 clearly shows some of the 300 GeV hadronic energy in HO even with ECAL+HB+HO configuration.

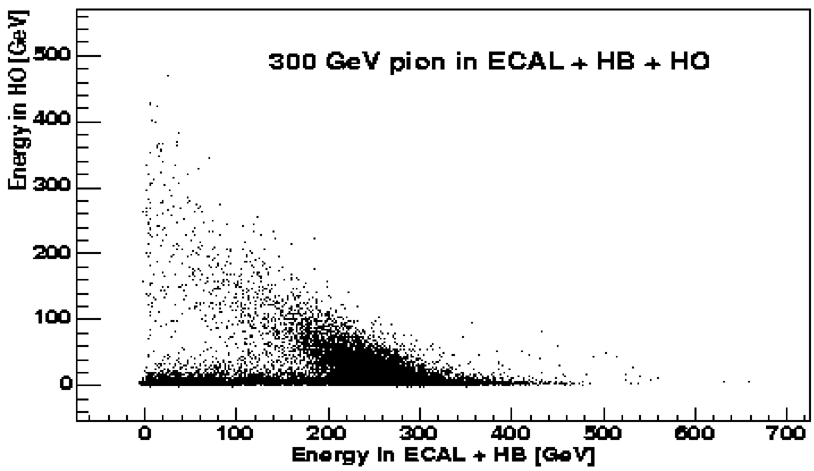

Figure 5.18: Scatter plot for ECAL+HB vs. HO using 300 GeV pion beam energy.

The pion energy distributions are illustrated in Fig. 5.19 for 50-300 GeV range, using HB+HO (no ECAL) detector configuration.

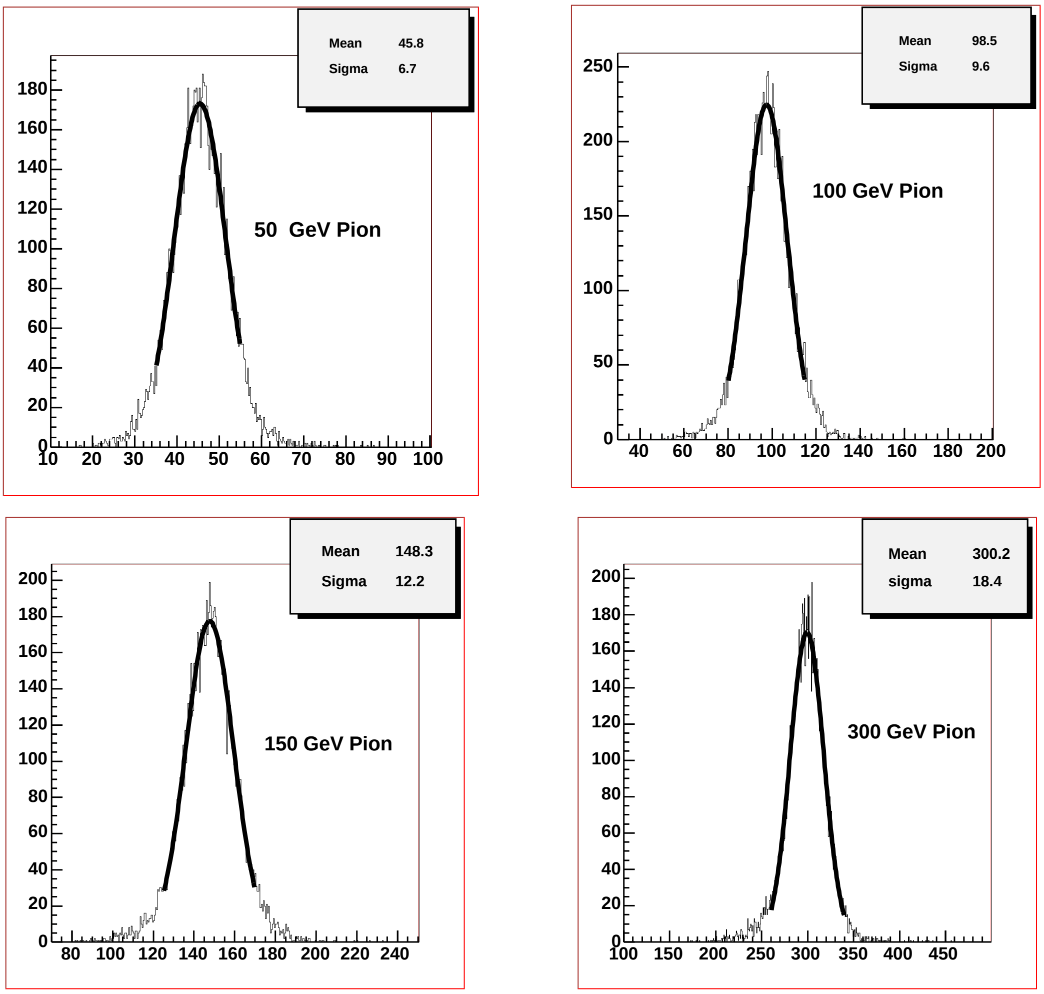

Figure 5.19: Pion energy distributions for 50, 100, 150 and 300 GeV beam energies in HCAL.

Longitudinal Shower Profiles in HCAL

The second HB wedge (HB2) was configured to measure the longitudinal shower development in the calorimeter. This was implemented by replacing the normal optical decoding unit (ODU) in the readout box with special ODU. Due to the limited number of HPD channels available in a readout box, this special ODU summed the light from the scintillator tiles along η at the same depth in the center HCAL towers (5-9). The remaining towers were optically masked out to reduce the possible contribution from the halo muons. The resulting energy measurements from each of 17 HCAL layers provided a complete longitudinal sampling of the hadron shower [10].

The average energy loss of a hadrons is mainly due to strong interactions. The hadronic showering process is dominated by a succession of inelastic hadronic interactions. At high energy, these are characterized by multi-particle production and particle emission originating from nuclear decay of excited nuclei. The hadronic showers spread over a large volume. The longitudinal profiles of pion showers at different energies were studied using the HCAL alone configuration. The energy deposited is studied as a function of HB layers numbering from 1 to 17. Fig. 5.20 clearly illustrates the fraction of the shower energy measured in each HB layer for 50, 100, 150 and 300 GeV pions. The pionic multi-particle cascades produced due to the strong interactions between the particle and the active detector material in the HCAL sampling calorimeter develops at the beginning, reaches a threshold at the maximum near to layer 5 and then falls off almost exponentially in the remaining layers.

Linearity

A particle loses all its energy in calorimeter and it is utilized in generating shower. So the total number of particles produced in the medium must be, on average, proportional to the initial energy of the particle and the response of a detector is linear with energy. Fig. 5.21 shows the response, measured energy divided by the incident beam energy, as a function of incident beam energy.

The total energy deposited by 300 GeV pion in HB2 configuration is calculated by adding the energy deposited in all layers of HB2. Fig. 5.22 shows energy distribution

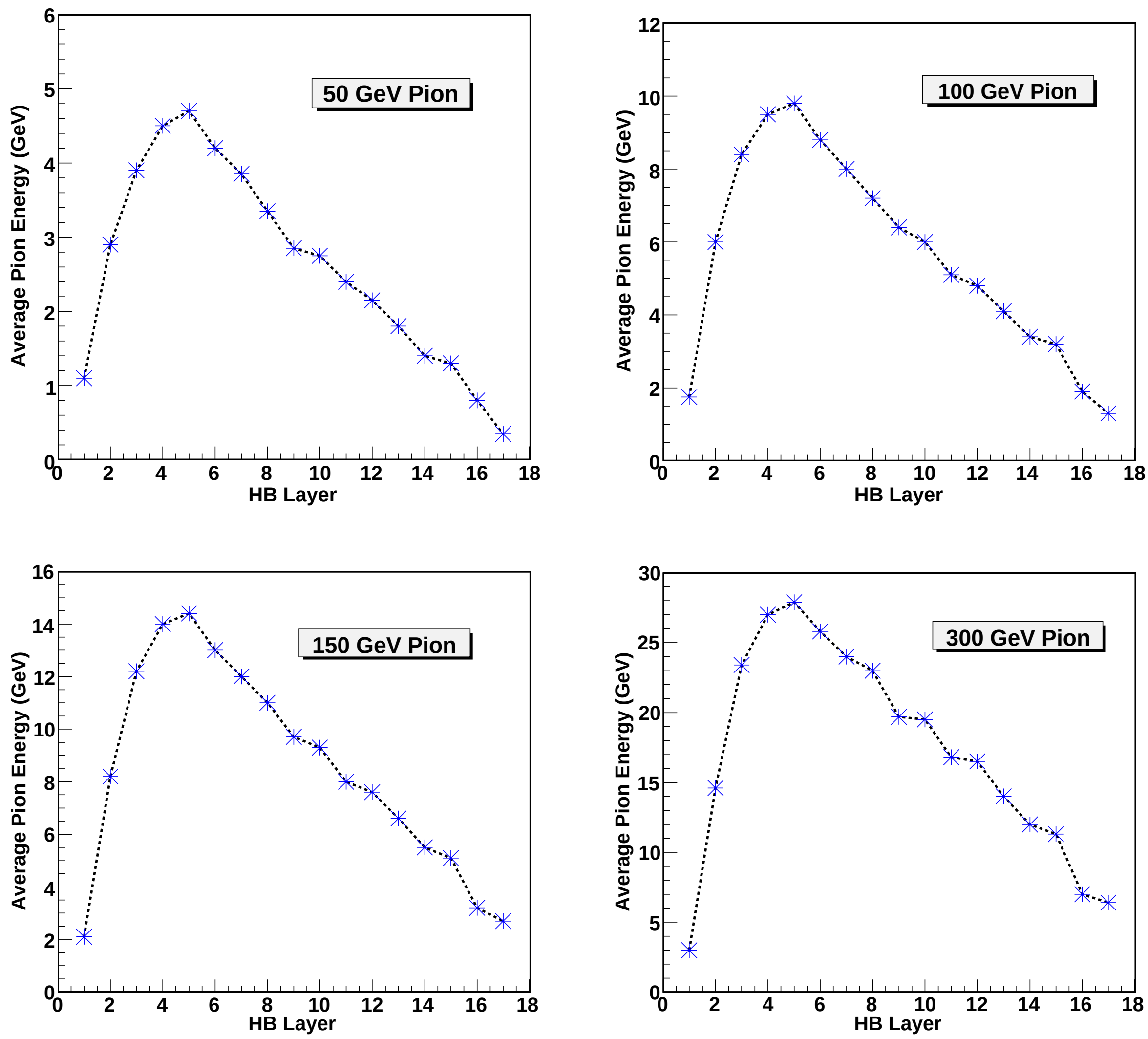

Figure 5.20: Longitudinal shower profiles for 50, 100, 150 and 300 GeV pion energies in HCAL.

for a 300 GeV pion energy, with and without HO energy to the HB matrix.

The measured distribution for this energy is more symmetric and have smaller widths after adding HO to the energy calculation. It is clear that adding HO layer to HB2 configuration helps in increasing the resolution of the energy of the calorimeter and reduces the leakage of energy from the calorimeter thus describing the importance of HO.

Resolution

Whatever may be the energy of the particle, it degrades down to the level of atomic excitations and deposits its entire energy. Because of the probabilistic nature of the processes involved in the production of shower particles, there is an intrinsic fluctuation in the number of particles. This intrinsic fluctuation gives an ultimate limit on the performance of the calorimeter. CMS HCAL being a sampling calorimeter, only a fraction of energy is deposited in sensitive detector. Since there is always a fluctuation in the number of particles produced at a given depth of calorimeter, the sampling fluctuations also worsens the resolution. In addition, there is a contribution from the photo-statistics. The photons produced inside the calorimeter have to be collected and directed to the readout boxes to be converted to an electronic signal. The effect of digitization by QIE is expected to further degrade the resolution. Event-to event fluctuation is larger at lower energies as compared to the higher energies. Therefore, the resolution is expected to improve with the energy of the incident particle. The fluctuations in the fraction of energy shared by electromagnetic component of hadronic shower for a given energy may worsen the resolution.

The HCAL resolution as function of test beam pion energies is plotted in Fig. 5.23. The resolution is calculated as the measured sigma per fitted mean of the pion energy distribution. beginfigure

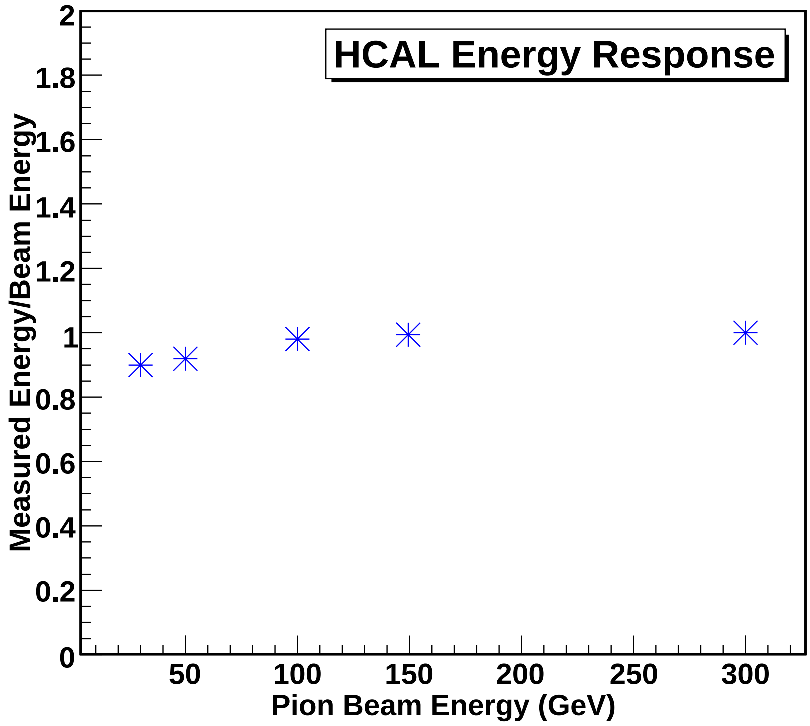

Figure 5.21: Variation of pion energy response (measured energy vs. beam energy) with beam energy in the HCAL alone setup.

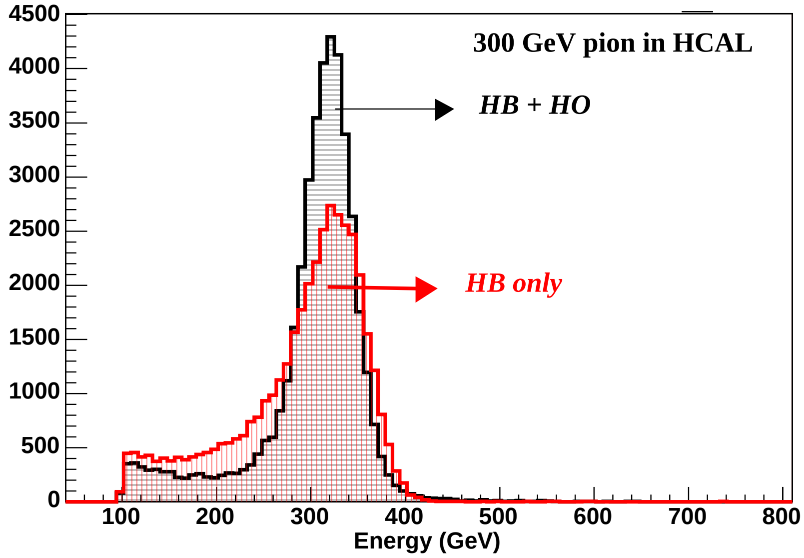

Figure 5.22: With and without HO energy sum for 300 GeV pion.

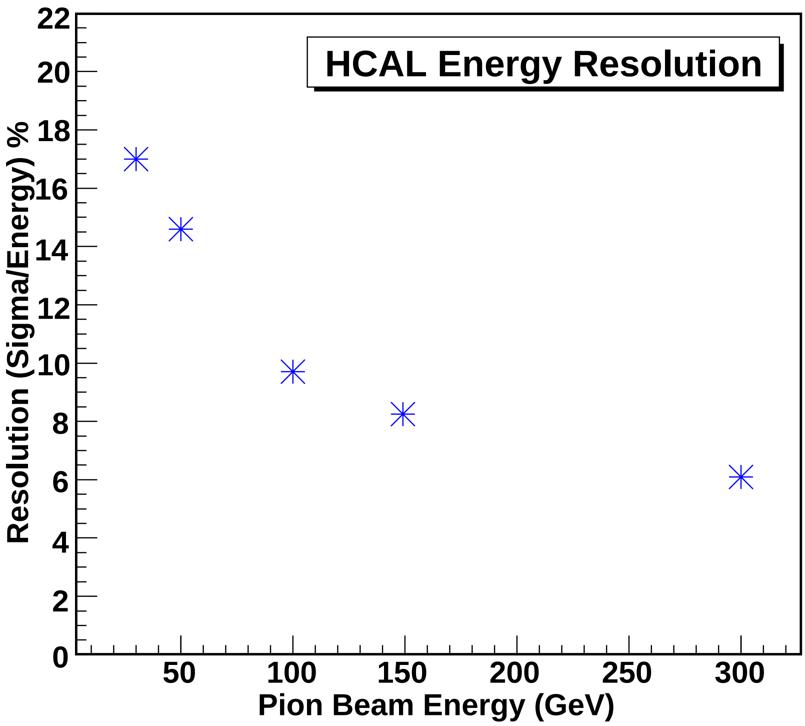

Figure 5.23: Variation of energy resolution with pion beam energy in the HCAL alone setup.

5.8 Relevance of HO

The HO production modules together with 2 wedges of HB and a prototype of one sector of endcap hadron calorimeter module were tested in the test beam facility at CERN. These detectors were exposed to a variety beams of hadrons, electrons and muons over wide energy range.

The actual performance of the HO system has been measured in the CERN test beams where a test module in test beams 1999 and 2002 and production HO scintillator trays in the test beams 2003 and 2004 were used with ECAL, HCAL barrel, forward and endcap prototypes. These were exposed to negative hadrons, electrons and muons with energies varying from 20 GeV to 300 GeV on specially made and movable test beam table (in both η-ϕ directions) in the H2 beamline [11] [12]. After calibrating ECAL with 100

GeV electrons, HCAL was calibrated with muons of fixed energy (100 or 150 GeV). Wire sourcing of the whole HCAL calorimeter was done for cross calibration factors. HO was also calibrated with muons. It was seen that average longitudinal hadron showers extend past the inner HCAL (mainly HB) located inside the magnetic coil mock up. Thus HO helps in measuring the high energy hadronic shower tail. The hadronic multiplication process is measured at the scale of nuclear interaction length (λ_I), which is essentially energy-independent. The addition of HO leads to a total ECAL+HCAL+HO depth of at least 9.5 λ_I for the entire η range spanned by the CMS hadron calorimeters [13].

5.8.1 Energy Measurements and Missing p_T Measurements

For the CMS detector, the number of interaction lengths including the HB and the preceding subdetectors is approximately 8 at $\eta = 0$. Since approximately 5% of the energy of a 300 GeV pion would be deposited beyond the outer limits of the HB, CMS has incorporated the HO to improve shower containment. The total depth of the calorimeter system is thus extended to $\simeq 11.8\ \lambda_I$, with an improvement in both linearity and energy resolution. The simulation studies show net improvement in missing E_T measurements at LHC energies. Inclusion of HO reduces the background cross section by a factor of 1.5 or even more than moderate missing E_T values around 200 GeV [14] . Single particle studies demonstrate that in the central muon ring, the HO starts playing a significant role for particles with transverse energies above 70 GeV. This effect gets somewhat reduced at larger η values (side muon rings) and the importance of leakage is shifted to higher energies.

5.8.2 Muon Trigger

The muon spectrometer for the CMS detector is realized by instrumenting the return iron yoke for the solenoidal magnet. The yoke is confirmed as four iron disks on each end and four cylindrical wheels in between. Layers of the drift chambers for tracking and resistive plate chambers (RPCs) for triggering are inserted into the gaps between the layers of iron. The HO is a good match to the RPC system in the sense that the region with the greatest noise and fewest planes is at high η, where muons give a larger signal in the HO due to the crossing angle. The second noisiest RPC trigger towers are at small η, where the HO has two layers of scintillators. The phase of the HO readout(energy vs. time) may be adjusted independent of the rest of the HCAL to yield the best signal-to background for the RPC trigger. 90% of the HO deposited energy is contained in two consecutive time samples. The preliminary interface specifications between two has been worked out. Backgrounds, efficiencies and trigger rates have been calculated [15] and the rate reduction factors as high as 100 can be obtained with approximately 90% efficient confirmation requirement even if the performance is not as good, the rate reduction factors are important enough to be considered.

5.9 Summary

The goals and the setup of the CMS HCAL test beam at CERN is included and discussed. The calibration constants are calculated for ECAL by exposing 100 GeV electrons. The ECAL response to electrons was also studied using electrons at different energies ranging from 50 GeV to 200 GeV. The calibration constants are calculated for HCAL detectors using 150 GeV muon beam. The HCAL response for pions is studied for energies ranging from 30 GeV to 300 GeV. The pion interacts with organic scintillator in the sampling calorimeter and results in secondary particle cascades. The longitudinal deposition profiles for pions are characterized by a sharp peak near to the HCAL depth where maximum MIPs are produced followed by a exponential fall-off. An important concern in hadron calorimetry is the energy leakage which causes degradation of the energy resolution with tails in the energy distributions. The importance of HO in the CMS HCAL relies in the improvement of energy resolution and shower containment of high energy hadrons. Recent attempts are also made to use HO as a muon triggering counter.

Bibliography

[1] S. Abdullin, A. Kumar, S. B. Beri, J. M. Kohli et al., Design, Performance, and Calibration of CMS Hadron-Barrel Calorimeter Wedges, CMS NOTE 2006/138.

[2] S. Abdullin, A. Kumar, S. B. Beri, J. M. Kohli et al., Design, Performance, and Calibration of CMS Hadron-Endcap Calorimeter Wedges, to be submitted to Nucl. Inst. and Meth (NIM).

[3] S. Abdullin, A. Kumar, S. B. Beri, J. M. Kohli et al., Design, Performance, and Calibration of CMS Forward Calorimeter Wedges, CMS NOTE 2006/044.

[4] S. Abdullin, A. Kumar, S. B. Beri, J. M. Kohli et al., Synchronisation and Timing in the CMS Hadron Calorimeter, CMS NOTE 2006/139.

[5] N. Akchurin et al., The Response of CMS Combined Calorimeters to Single Hadrons, Electrons and Muons, CMS NOTE 2007/012.

[6] P. Sopicki et al., Calibration and performance of lead tungstate electromagnetic calorimter for the HCAL test beam 2003, CMS IN 2004/033.

[7] Ashok Kumar, Suman Beri, J. M. Kohli et al., (CMS Collaboration), Response of CMS Calorimeter to electrons and muons, proceedings of at XVI DAE HEP symposium, Nov. 2004, SINP, Kolkata, India.

[8] E. Hazen et al.,Radioactive source calibration technique for the CMS hadron calorimeter, Nucl. Instrum. Methods Phys. Res., A 511 (2003) 311-327.

[9] Harinder Singh, J. M. Kohli, N. K. Mondal et al., (CMS Collaboration), Muon Trigger Studies using CMS Outer Hadron Calorimeter, proceedings of XVI DAE HEP symposium, Nov. 2004, SINP, Kolkata, India.

[10] S. Abdullin, A. Kumar, S. B. Beri, J. M. Kohli et al., Longitudinal Shower Profiles Measured in CMS HCAL and Comparison with Geant4, CMS NOTE 2006/143.

[11] V. D. Elvira, Measurement of the Pion Energy Response and Resolution in the Hadron Barrel Calorimeter using CMS HCAL Test Beam 2002 Data, CMS NOTE 2004/020.

[12] V. D. Elvira, Validation of Geant4 Physics Using the CMS HCAL Test Beam 2002 Experiment, CMS NOTE 2004/021.

[13] V. V. Abramov et al., Studies of the Response of the Prototype CMS Hadron Calorimeter, Including Magnetic Field Effects, to Pion, Electron, and Muon Beams, CMS NOTE 2000/003, Nucl. Instrum. Methods Phys. Res., A 457 (2001) 75-100, hep-ex/0007045.

[14] Sunanda Banerjee and Sudeshna Banerjee, Performance of Hadron Calorimeter with and without HO, CMS NOTE 1999/063.

[15] C. Albajar et al., Conceptual Design of Hadron Outer Scintillators in the RPC Muon Trigger, CMS NOTE 2003/009.

Chapter 6

$H \to \mu^+\mu^-$ Simulation Study

6.1 Physics Simulations

What happens when two particles collide in the center of a detector? At the interaction point, either the two particles are just scattered away, or new-born particles sort out with a given momentum. If those particles are unstable, they tend to decay with their proper lifetime, and at a distance typical of the size of the detectors only stable, or practically stable, particles survive. The particles coming out from the collision point interact in the detector material. Such a material can be either active, that is a material in which the modifications induced by the passing particle can be recorded somehow and thus give out some sort of signal, or passive, that is a region in which interactions just happen, but locally no signal can be extracted out of them. Sensitive areas of the detector produce electronic signals as result of the particle-material interaction. Those signals get shaped, discriminated and read out by dedicated electronic devices, whose output can be digitized and provided to the subsequent steps of the data acquisition (DAQ). Fast hardware components (triggers) use part of those signals to decide on-line whether to accept the event or not. Only in case of a positive trigger decision, the DAQ reads out the digitized signals and write them onto a permanent support by using an appropriate format (raw data). Typically, before writing the whole raw data on the permanent disks, a further decision is taken by software modules (like high level trigger, HLT) which can compute a few physics quantities relevant to the event with fast algorithms. Starting from the raw data one then tries to reconstruct the particles which originated those signals, that is one has to estimate the trajectory, the momentum, the energy and possibly the mass (if some particle identification is effective) of all particles that generated the digitized output of the data acquisition chain. A complex, detailed, dedicated software, which combines the information contained in the raw data with huge geometry and calibration data-bases, accomplishes this task. First, raw data from a single subdetector are used to extract the hits. Hits are then combined to produce intermediate analysis objects within the subdetector (local reconstruction), which in turn constitute the building blocks for the higher level analysis objects, at different degrees of complexity, used for the final physics analysis.

Simulation of HEP Event

It takes time to built an high energy accelerator and relevant detectors. Question is to get the feeling of what can be the physics outcome of such prolonged hard work. Simulations are performed by using the different Monte-Carlo event generators. After event generation, detector level simulations are performed to get the feeling of overall detector response to some particular interaction. The particles interact with the detector material and events are registered in the form of electronic signals. A data acquisition stored a digitized version of the information. In the event reconstruction process the digitized electronic signals are turned back into a list of a particle momenta and charges. The reconstructed events can be used for real physics outcome. This helps in shaping the entire collaborative effort in some particular goal of an experiment.

To simulate an event and take into account all what happens in a high energy physics experiment, one has to provide the following steps:

- Event generation.
- Simulation of the interaction of the generated particles with the detector.

- Simulation of the digitization phase.

- Local and global event reconstruction.

While the first part (generation) remains a task of the model builders and phenomenologists, the simulation of the interactions with the detector, digitization and event reconstruction are worked out by the experimental collaborations that design, build and maintain the detectors. In the detector simulation, one tries to simulate the result of all the physics processes and intermediate steps that lead from the four-vectors and vertices of the generated particles to the final analysis objects. If the output of the simulation after the digitization phase has the same format as the really collected raw data, the same reconstruction software can be used on raw data. Effects as electronic noise in the detectors, event overlapping (pile-up), instrumental dead-times, etc., must be properly taken into account to provide realistic reconstructed analysis objects.As experiments get more complex, also their simulations become more complex, CPU time (and physicist time) consuming. Therefore, while for several tasks the most possibly detailed simulation is advised, there are many where the required level of precision makes more suitable a less detailed but much quicker simulation [1]. One of the domains in which a fast simulation is certainly more suitable than a full simulation is when a new theoretical model is available and physicists want to evaluate the experimental accessibility of their own scenario: there is no reason to study all the complex details of an experimental apparatus implicit in the use of a full simulation, and wait uselessly for days, weeks, (or even months, if those events have no high priority for the collaboration production teams) if one just wants to estimate whether a given scenario can be visible, and how. My analysis in this chapter is performed upon simulated data in $H \to \mu^+\mu^-$ channel. The Large Hadron Collider Grid (LCG) is used for data production and is described in section 6.5.

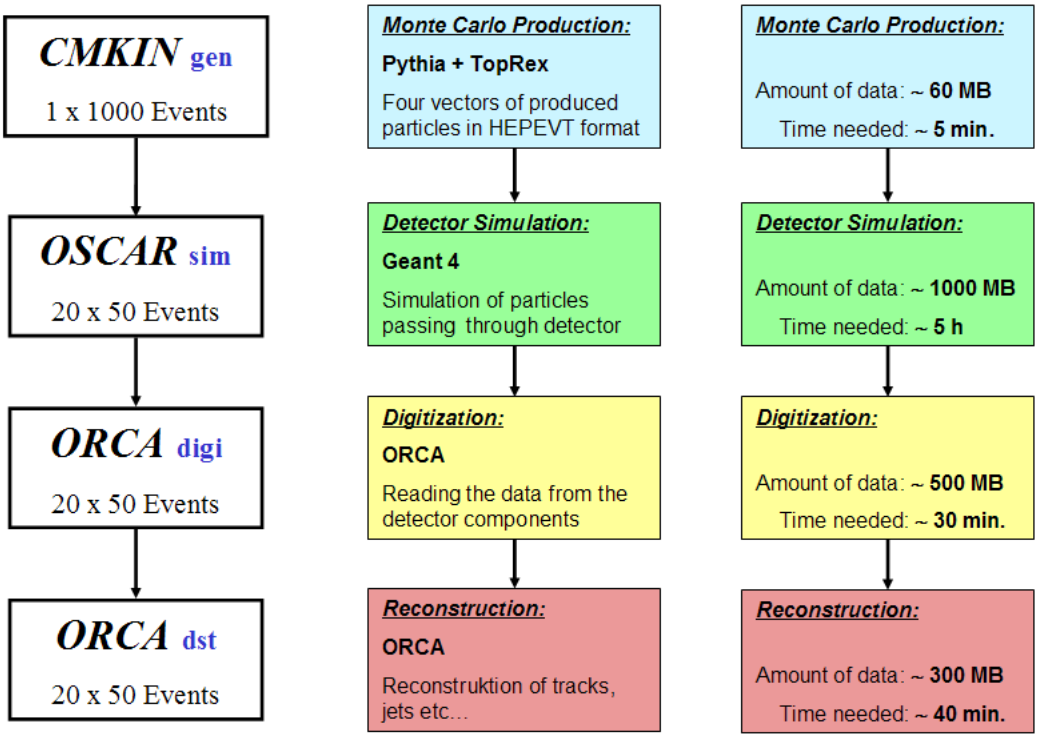

Figure 6.1: An overview of the different steps in a CMS production chain (the numbers refer to a production set of about 1000 top events)

6.2 CMS Simulation Structure

The CMS experiment at LHC will be unique tool for fundamental physics research specially at the TeV energy scale. Monte Carlo simulations are critical component of physics analysis in a large HEP experiment such as CMS. Until the first LHC run, the Monte Carlo softwares are used to generate events. To simulate the passage of particles and their interactions with the CMS detector usage of detector simulation packages based upon object oriented C++ create adequate computer model of the detector and simulate the response of its detectors up to the level of real data. The reconstruction of events in order to provide the reliable estimation of detector efficiencies for all the particles is needed and done with C++ object oriented reconstruction softwares. Hence, the CMS event production chain is comprised of monte carlo generation, detector simulation, digitization, reconstruction and DST production as depicted in Fig. 6.1. In a simulation of an event at LHC, in order to obtain realistic final state analysis objects one has to simulate all the relevant processes that happen in the real life, when the particles produced in the p-p collision propagate through the detector volume and interact with its material.

6.2.1 Event Generation

Standard Monte Carlo generators, such as PYTHIA [2], ALPGEN [3], ISAJET [4], HERWIG [5] etc. can be used to simulate the collisions between two protons at a centre of mass energy of 14 TeV. The events produced are stored in the standard HEPEVT - a HEP standard to store particle kinematics for one event. The interface to the user, the interface to the Monte Carlo generator, and the input/output software is steered by the CMKIN [6]. So, basically CMKIN is interface between generators and CMS detector simulation. This package can be also be used as a tool for direct analysis and verification of generated events without detector simulation.

6.2.2 Detector Simulation

It is important that in the simulation studies of the LHC experiments as realistic as possible information about the detectors an the physics processes is used. Detailed simulation of the CMS experiment is based on the Geant4 toolkit The purpose of the detector simulation is to understand the detector response to physics events for signal and background studies. C++ based detector simulator, Geant4 is a detector simulation toolkit for high energy physics experiments, A variety of system requirements also come from heavy ions physics, cosmic rays physics, space science applications, and medical applications. In the CMS simulation approach, Geant4 [7] based Object oriented Simulation for CMS Analysis and Reconstruction (OSCAR) [8] does the tracking of particles through the detector, including all interactions with the material, and delivers simulated hits called SimHits. The SimHits are directly readable by Object-oriented Reconstruction for CMS Analysis (ORCA) [9]. GEANT4 simulation employs the full set of electromagnetic and hadronic physics processes provided by Geant4 and detailed particle tracking in the 4 Tesla magnetic field. The design also previews the use of parameterizations of the electromagnetic and hadronic showers, instead of full modeling of high energy particles passage through a complex hierarchy of volumes and materials, allowing a significant gain in speed while tuning the simulation to test beam and collider data. Its also provides the tools for the implementation of the full CMS detector geometry and the interfaces required for recovering information from particle tracking in the detectors. It implements their sensitive detector behavior, track selection mechanisms, hit collections and numbering schemes. This functionality is interfaced to the CMS framework which allows the user to selectively load desired modules and to configure and tune the final application. The physics simulation has been extensively validated by comparison with test beam data and previous simulation results. The redesigned and upgraded simulation software was exercised for performance and robustness tests, running on the US and EU grids. The OSCAR is based on CMS object-oriented framework Coherent Object-oriented Base for simulation Reconstruction and Analysis (COBRA).

6.2.3 Detector Response Simulation and Reconstruction

The CMS reconstruction software ORCA uses modern technology and in particular C++ object-oriented programming. The ORCA project covers currently not only the reconstruction tasks, but also includes code for simulating detector response and the level-1 trigger, as well as high level trigger and analysis code.

ORCA has adopted a two-level decomposition - subsystems and packages - to match the different tasks it covers. Typical subsystems are Calorimetry, Tracker, Muon or Trigger matching the hardware components of CMS. Other subsystems provide common services for several subdetectors (CommonDet, CommonReco) or analysis tasks (Jets) or high level reconstruction (ElectronPhoton, JetMetAnalysis, Muonanalysis, HiggsAnalysis). We have used HiggsAnalysis package for Higgs decay to dimuon channel simulation study.

The reconstruction software is based on the COBRA software framework. COBRA provides basic services and utilities: physics type services such as histogrammers, fitters, mathematical algorithms, geometry and physics calculation and computer services such as data access, inter-module communication, user interface etc. It also have classes which can handle flow control, module scheduling, input/output etc. Two main concepts implemented in the COBRA framework to steer the event processing are 'action on demand' and 'implicit invocation'.

6.2.4 Digitization

The digitization step is a second level of detector simulation, placed just at the interface with the reconstruction program, where the physical information registered, reprocessed in order to simulate the detector output, and eventually written out (DIGI structure) to be used by the reconstruction programs. The output from the digitization is obtained in a form similar to that which might be expected from the readout electronics in the actual experiment.

De-coupling the digitization from the tracking allows to study the same signal event under different beam conditions, without always having to redo the time consuming tracking of the particles through the detector. After combining a signal event with the selected pile-up events for a particular luminosity, the detector response is simulated taking in to account the simulated hits of all events of a crossing. The time information of each hit shifts according to the bunch crossing to which the corresponding event belongs. The finite response time and the time resolution of the CMS subdetectors defines for each subdetector a time window of sensitivity, ranging from a tens of nanoseconds to several hundred nanoseconds. To simulate the full detector response and occupancy, simulated hits in the full time interval of sensitivity need to be taken in to account. Hence, combination of pile-up treatment with pixel detectors + Silicon microstrip detectors +

ECAL detectors + HCAL detectors + muon detectors is the simulation of CMS detector response.

6.2.5 Reconstruction

The reconstruction process is carried out in two steps. First a local reconstruction is performed separately for the various subdetectors in terms of digital response from the readout electronics. For simulated data the result of the digitization step (DIGIs) are used to produce reconstructed hits (RecHits). The framework provides a mechanism to store and retrieve RecHits to/from databases. The access to RecHits is provided via DetectorUnit objects that can also encapsulate geometrical properties and calibrations. DetectorUnits also provide access to the raw data via ReadOutUnits. These model the readout electronics of the detector and have the responsibility to create DIGIs - from the online DAQ or during the digitization - or read the DIGIs from the database. They are observers of physics events.

The second step is global reconstruction which delivers reconstructed objects (RecObjs) suitable for further global reconstruction for physics analysis. Reconstruction is performed by RecUnits that register as observers to the framework and get notified about the arrival of new physics events. The RecObjs are produced in collections and iterators are provided to access them. The reconstruction algorithms are contained in Reconstrcutor objects that interact with the RecUnits. They obtain from the framework the handle to the "event" and contain the algorithm, Different Reconstruction/RecUnit combinations may produce the same RecObjs. This allows an easy exchange or comparison of different algorithms. The RecObjs produced by different Reconstructors are identified with ASCII strings. It is required that reconstructed objects can be made persistent, and COBRA provides full support to store and retrieve RecObjs belonging to a given event. An application of this is to enforce the re-reconstruction of RecObjs with the same Reconstructor but using different calibrations, alignments or parameters to the reconstruction algorithms.

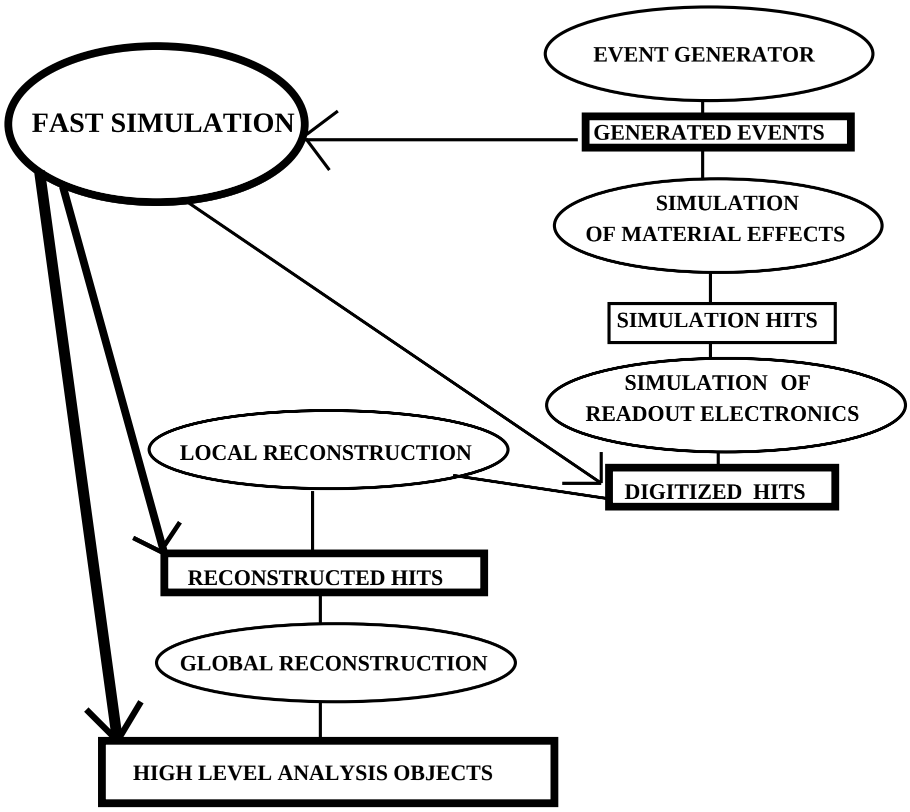

Figure 6.2: Block diagram of a full and a fast simulation in a typical LHC experiment. They all start from the same MC generated events and aim to produce as similar as possible final analysis objects.

6.3 Fast Simulation

Fast simulation of a high energy physics experiment is a tool used by experimentalists to quickly assess the potentiality of their detectors on a specific analysis or reconstruction technique, before embarking themselves into a more time and CPU expensive detailed study with the full simulation as shown in Fig. 6.2. In some cases, it can also be considered the access point for theoreticians wanting to see 'how do their model looks like in the real life'. A fast simulation is not meant to be a replacement of the full simulation. Its purpose is to produce some final analysis object in the shortest possible time, compatibly with the level of accuracy required to satisfy the needs of the task it is used for. Emulation of intermediate quantities, as digitized or reconstructed detector hits, could also be provided. Fast simulation emulates the combined result of detector simulation and reconstruction, and it is therefore generally tuned and validated with the full simulation results (while full simulation is tuned and validated with the real data). Domains where a fast simulation is more suitable than a full one are:

- Quick and approximate estimates of signal and background rates.
- Fast development of analysis methods and algorithms.
- Test of new generators or new theoretical ideas in a realistic environment.
- Scan of complex, multi-parameter spaces (like e.g. SUSY).
- Possibly cross-check a few aspects of a full simulation.

Fast simulation in CMS

Software package FAMOS [10] is used for the fast simulation of particle interactions in the CMS detector. The output of FAMOS is designed to be as close as possible to the output of the full simulation and reconstruction of CMS. It delivers the same physics objects (calorimetric hits and clusters, tracker hits, and reconstructed tracks and muons), with identical interface: they can be used as inputs of the same higher-level analysis algorithms (b-tagging, electron, muon and tau candidates, jet clustering, lepton isolation, etc.) as the real or fully simulated data. Particles in FAMOS are propagated in the nominal magnetic field through the inner tracker and up to the entrance in the calorimeters. The following interactions are simulated in the tracker material:

- Electron bremsstrahlung.
- Photon conversion.

- Charged particles energy loss by ionization.
- Charged particles multiple scattering.

Electron, photon and hadron showering is allowed in the ECAL and HCAL. Nuclear interactions are not simulated in FAMOS, which implies that hadronic showers never initiate before the calorimeters, and there is a lower number of secondary vertices.

6.4 CMSSW : An Application Framework

The overall collection of software, referred to as CMSSW [11], is built around a framework, an Event Data Model (EDM), and services needed by the simulation, calibration and alignment, and reconstruction modules that process event data so that physicists can perform analysis. The primary goal of the Framework and EDM is to facilitate the development and deployment of reconstruction and analysis software.

The CMSSW framework implements a software bus model wherein there is one executable, called cmsRun, and many plug-in modules which run algorithms. The same executable is used for both detector and Monte Carlo data. This framework is distinct from a more traditional approach in which several executables are used, one per task or set of tasks. The CMSSW executable, cmsRun, is configured at run time by the user's job-specific configuration file (set of parameters). This file tells cmsRun which data to use, which modules to run, which parameter settings to use for each module, and in what order to run the modules. Required modules are dynamically loaded at the beginning of the job.

The CMS EDM is centered around the concept of an Event as a C++ object container for all RAW and reconstructed data pertaining to a physics event. During processing, data are passed from one module to the next via the Event, and are accessed only through the Event. All objects in the Event may be individually or collectively storable as ROOT [12] files, and are thus directly browsable in ROOT.

6.5 LHC Computing Grid

The LHC, currently being built at CERN near Geneva, is the largest accelerator on the earth. When it begins operations in 2008, it will produce roughly 15 Petabytes of data annually, which thousands of scientists around the world will access and analyze. The mission of the LHC Computing Project (LCG) [13] is to build and maintain a data storage and analysis infrastructure for the entire high energy physics community all over the world that will use the LHC.

The immediate goal of this development is to cope with the storage and analysis of millions of gigabytes of particle physics data that will flow annually from CERN's LHC, due to be launched next year. However, just like the World Wide Web, invented at CERN in the early 90s for research purposes, scientific Grid projects led by CERN are expected to create new opportunities for commerce and industry. CERN's flagship Grid initiative, the LHC Computing Grid (LCG) project, already runs a Grid service for particle physicists spanning over 200 sites at universities and research institutes worldwide. CERN also leads the Enabling Grids for E-sciencE (EGEE) project, a multi-science Grid infrastructure with 91 partners in Europe, Russia, the U.S. and Asia. EGEE supports a wide range of scientific applications, from biomedicine to astrophysics, and is being tested for business applications as diverse as financial modeling and petroleum prospects. CERN also has established the CERN openlab partnership with leading IT companies - including HP, Intel and Oracle - to investigate future trends in hardware and software that will influence the development of Grid technology.

As the Web was CERN's response to a new wave of scientific collaboration at the end of the 1980s, the GRID is the answer to the need for data analysis to be performed by the world particle physics community. With the LHC, the CERN experiments will have to handle petabytes of data that can not even be handled by the most advanced computers currently available. The proposed solution is the GRID, a very powerful tool tying computing resources distributed around the world into one computing service for all requesting applications. A rapid and natural consequence of the GRID has been the development of a Europe-wide database of mammograms for epidemiological, as well as teaching purposes. Today, 32 Mbytes are needed to store a mammogram image, giving a total of 128 Mbytes per person per visit.

The data from the LHC experiments will be distributed around the globe, according to a four -tiered model. A primary backup will be recorded on tape at CERN, the "Tier-0" center of LCG. After initial processing, this data will be distributed to a series of Tier-1 centers, large computer centers with sufficient storage capacity for a large fraction of the data, and with round-the-clock support for the Grid. The Tier-1 centers will make data available to Tier-2 centers, each consisting of one or several collaborating computing facilities, which can store sufficient data and provide adequate computing power for specific analysis tasks. Individual scientists will access these facilities through Tier-3 computing resources, which can consist of local clusters in a University Department like one in Panjab University.

Data production using LCG

A Realization of Distributed Analysis for LHC (ARDA) [14] is a project to coordinate the different activities that are needed to prototype distributed analysis systems for the LHC experiments using a grid. Arda Support for cms Analysis Process (ASAP) [15] is a framework which contains two distinct components, the JobGenerator and JobManager. The JobGenerator uses the information obtained from the CMS Data Management tools (RefDB/PubDB) to create and submit jobs to a given scheduler (currently LCG-2 or gLite). The JobManager deals with job monitoring after submission, resubmission in case of Grid and processing failures and retrieval of the output. ASAP provides a simple command line interface and generates Web pages which the user can view to monitor the current state of their task. ASAP provides two possible modes of interacting with the system:

- **Simple mode:** All actions required to process the data samples (job generating, job submission, querying job status, retrieving the output) are done by the user by issuing corresponding ASAP commands.

- **Advanced mode:** In the advanced mode user only needs to generate the jobs for a given sample by calling ASAP job generation command. They can then delegate the job submission, resubmission and output retrieval to the Job Manager and monitor progress via the Web.

6.6 Study of Higgs Decay to Dimuon Channel

The Higgs mechanism is widely believed to be responsible for the electroweak gauge symmetry breaking and possibly for the fermion mass generation. Searching for Higgs bosons have thus become high priority in future collider experiments, and the LHC. The phenomenological aspects of a fundamental Higgs particle are well understood. After the initial discovery, it would be more important and more challenging to understand the properties of the Higgs bosons, in particular their couplings to the Standard Model (SM) particles. Precisely because of the role of the Higgs bosons in the mass generation mechanism, they couple to the SM particles proportional to their masses. Such characteristics of Higgs bosons should be thoroughly tested at collider experiments and hopefully provide new insight for the development of a more complete particle theory up to Planck scale. The H $\rightarrow \mu^+\mu^-$ channel would be the first observation for a Higgs boson to decay to second-generation fermions. It is necessary to confirm the proportionality of m_μ for the Higgs coupling $H\mu^+\mu^-$ as predicted by the SM and hence Higgs particle that generates mass for the weak boson is also responsible for mass generation of the second generation of fermions.

Due to the rather small branching fraction for $H \rightarrow \mu^+\mu^-$, it will be very challenging to observe this channel. In the Minimal Supersymmetric Standard Model (MSSM) the associated production with b quarks $gg \rightarrow b\bar{b}H/A/h$ is enhanced at large tanβ yielding good prospects for the $H \rightarrow \mu^+\mu^-$ decay channel [16]. Two search methods are possible for the SM Higgs boson searches with $H \rightarrow \mu^+\mu^-$: the inclusive search exploiting all production channels and the exclusive search in the weak boson fusion (WBF) channel. In the inclusive search the backgrounds, mainly from Z production, remain large under the tiny signal peak and therefore large luminosities are required for a significant signal. In the weak gauge boson fusion the quark jets emitted in the forward rapidities can be used to suppress efficiently Z and $t\bar{t}$ backgrounds. The low jet activity in the central area between the tagging jets can be exploited to suppress further the $t\bar{t}$ background vetoing on jets in this area. In this present thesis the exclusive channel is studied.

6.7 Higgs Production via WBF Process

Although the production cross section for a low mass Higgs is largest in the gluon fusion process, the WBF cross section at the LHC is sizeable for all relevant Higgs masses. The WBF cross section is 1/3rd of the gluon fusion cross section. The gluon fusion cross section depends significantly on the Yukawa coupling of the Higgs to the top quark, while the WBF depends only on the weak boson couplings to the quarks and to the Higgs boson. Thus, WBF process has emerged as potentially the channel where a light or medium mass Higgs particle might be discovered first.

$$pp \rightarrow jjH \quad (qq \rightarrow qqH)$$

The distinctive feature of this process is the forward and backward jets that are generated by the quarks from the incoming protons and preserve the initial parton direction due to the absence of color exchange in the t-channel. This results in energetic forward jets (large pseudo rapidity $|\eta|$) and suppressed hadronic activities in the central region. These jets are referred as forward “tagging jets”. Nearly half of these jets can be detected and measured by the CMS hadron forward (HF) calorimeter, covering the pseudo rapidity range $|\eta| \approx 3$ to 5, and other half by the CMS hadron endcap (HE) calorimeter with $|\eta| \approx 1.5$ to 3.

6.8 Motivation for $H \to \mu^+\mu^-$ Channel

Some analysis based on Particle level and fast simulation studies were earlier performed on the $H \to \mu^+\mu^-$ decay channel at the LHC. It has been shown that by including both gluon fusion channel and the weak boson channel for both ATLAS and CMS detectors, LHC with 300 fb^{-1} can observe the $H \to \mu^+\mu^-$ to statistical significance of 3σ over a Higgs boson mass range of $110 < m_H < 140$ GeV/c^2 [17]. A particle level study of this channel at the LHC based on the weak-boson fusion, $WW, ZZ \to H \to \mu^+\mu^-$, was carried in Ref. [18] and predicts an about 1-2σ statistical effect for an integrated luminosity of 300 fb^{-1}. A fast simulation study in CMS has been carried out for the Higgs boson with $m_H = 120$ GeV/c^2 [19]. A statistical significance of 1.9 and a signal-to-background ratio of 0.4 has been obtained for the inclusive channel with 300 fb^{-1}. The exclusive (WBF) channel has been found to yield a statistical significance of 1.1 and a signal-to-background ratio of 40%. Since no results are available based on full detector simulation, this study was undertaken in present analysis. Full simulation in comparison to fast simulation is actual tool to tune and validate physics results with the real data.

6.9 Production Cross Sections and Branching Fractions

Fig. 6.3 shows the NLO production cross sections for the SM Higgs boson for $m_{top} = 175$ GeV/c^2 as a function of m_H [20]. The cross section for the weak gauge boson fusion with $m_H = 120$ GeV/c^2 is 4.43 pb. Branching fractions for the SM Higgs boson decays at the low part of the mass spectrum are shown in Fig. 6.4 [21]. The branching fraction slowly decreases up to $m_H = 150$ GeV/c^2, beyond which the branching fraction becomes vanishingly small. In this work the mass value $m_H = 120$ GeV/c^2, close to the LEP limit, is chosen. The branching fraction to $\mu^+\mu^-$ is 2.4 $\times 10^{-4}$. Only 66 events are expected for the $qq \rightarrow qqH, H \rightarrow \mu^+\mu^-$ channel for 60 fb^{-1}.

6.9.1 Background Processes

The main backgrounds for the $H \rightarrow \mu^+\mu^-$ signal are listed below:-

- $t\bar{t} + jets$ production where the missing transverse momentum is small, as for the $WWjj$ background. Either the bottom quarks from the top quark decays or the additional jets are tagged as forward jets. It has been shown that $t\bar{t}j$ is expected to be most severe of these, followed by $t\bar{t}jj$ and a negligible contribution from $t\bar{t}$. The Branching fraction for the clean double-muon final state from the top pair decay is $\frac{1}{81}$. The suppression of the $t\bar{t} + jets$ background is achieved mainly by forward jet selection and an extra jet veto in the central region [22].

- QCD Zjj production followed by the decay $Z \rightarrow \mu^+\mu^-$. Before cuts this is the dominant Z background. It consists of radiation of a Z boson off initial state and final state quarks.

- Electroweak (EW) Zjj production with a subsequent decay $Z \rightarrow \mu^+\mu^-$. This background includes the signal diagram where the Higgs line is replaced by a Z boson, which makes it particularly hard to remove using kinematical cuts.

- W^+W^-jj and $b\bar{b}jj$ production (with both bottom quarks decaying to muons), missing transverse momentum plays crucial role to suppress these backgrounds. Both of them are not simulated in this study.

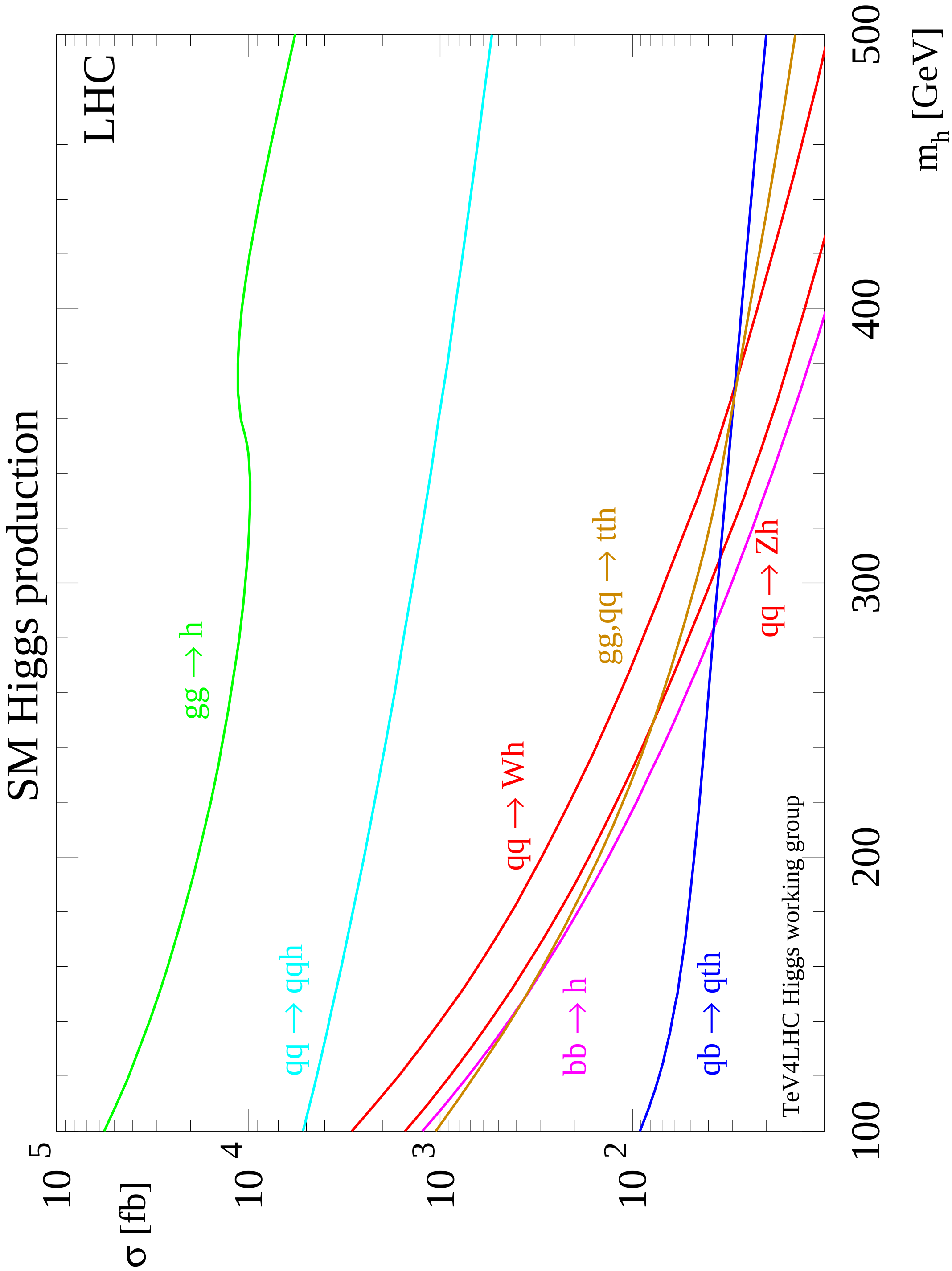

Figure 6.3: The NLO cross sections for the SM Higgs boson as a function of m_H with $m_{top} = 175$ GeV/c^2 [20].

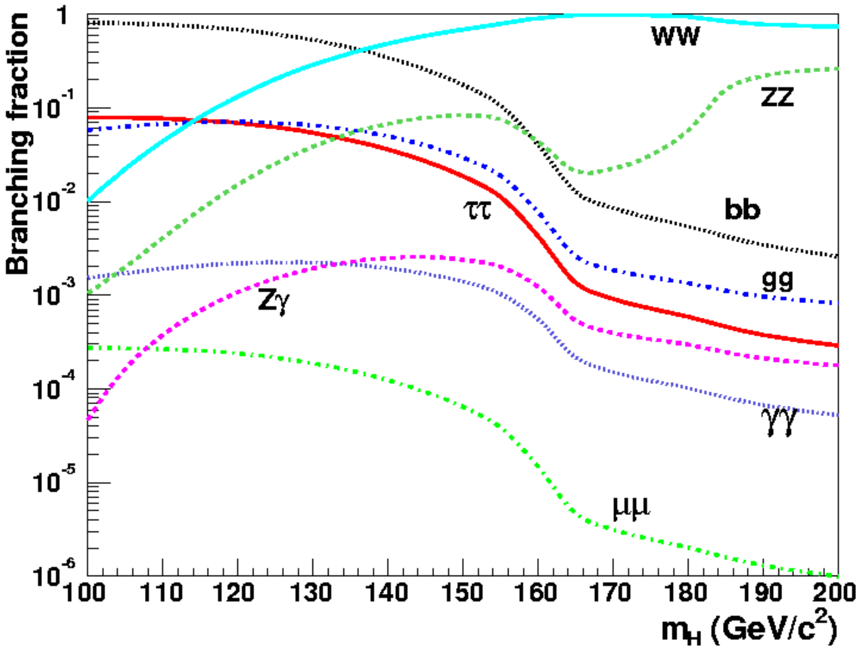

Figure 6.4: Branching fractions for the low mass SM Higgs boson as a function of m$_H$.

6.10 Event Generation, Simulation and Reconstruction for $H \rightarrow \mu^+\mu^-$ Study

The signal events were generated with PYTHIA with the WBF processes $qq \rightarrow WW \rightarrow qqH$ and $qq \rightarrow ZZ \rightarrow qqH$ and normalized to the cross section and branching fraction of Figs. 6.3 and 6.4. The Higgs boson was forced to decay to muons. The background, Z production in association of jets was generated with PYTHIA with the processes $qq' \rightarrow gZ$ and $qg \rightarrow qZ$ in the range of $10 < \hat{p}_T < 100$ GeV/c. All leptonic decay channels, including the Z decays to $\tau\tau$, were generated. The cross section for this data set is 5.1 nb. The electro-weak qqZ background was generated with MadGraph [23] imposing the cuts $p_T^q > 20$ GeV/c, $\eta^q < 5$, $|\eta^{q1} - \eta^{q2}| > 4.2$, $\eta^{q1} \times \eta^{q2} < 0$, $M_{q1,q2} > 900$ GeV/c^2, $M_{\mu\mu} > 70$ GeV/c^2 on the generation level. The cross section for this event sample is 86 fb.The $t\bar{t}$ events were generated with PYTHIA. Two muons with $p_T > 20$ and 10 GeV/c within $|\eta^\mu| < 2.5$ and with $M_{\mu\mu} > 10$ GeV/c^2 were required at the generation level. The total cross section was normalized to the NLO cross section of 850 pb, yielding a cross section of 20.9 pb after the kinematic selection.

The response of the CMS detector was simulated with the OSCAR package, as discussed in section 6.2, including a pile-up corresponding to the luminosity of $2{\times}10^{33} cm^{-2} s^{-1}$. The physics objects were reconstructed with the standard methods available in the CMS reconstruction software. The version ORCA_8_7_4 of the CMS OO Reconstruction was used. The primary vertex was reconstructed and selected with an algorithm searching for the highest sum of the transverse momenta of the associated tracks. Muons were reconstructed with the GlobalMuonReconstructor package. The jets were reconstructed in a cone of 0.5 and the jet energies were calibrated with correction factors obtained from MC studies [24]. In the correction method, energy and E_T thresholds of 0.8 GeV and 0.5 MeV, respectively, were set on the electromagnetic calorimeter (ECAL)-plus-hadron calorimeter (HCAL) cells. The missing transverse energy (E_T^{miss}) was reconstructed from the full calorimeter response summing the ECAL-plus-HCAL towers. For this measurement the hadronic jet energies were calibrated with correction factors obtained from a simulation of QCD photon+jet events [24]. These corrections were applied on corrected jets with $E_T > 20$ GeV.

6.11 Event Selection

6.11.1 Trigger

At the first step of the analysis the event was required to pass the logical OR of single-muon (1 μ) and di-muon (2 μ) trigger streams, both Level-1 and HLT [24]. The p_T thresholds of 19 and 7 GeV/c were used for the single and double muon triggers, respectively. The trigger efficiencies for the signal and backgrounds samples are shown in Table 1. The difference of the Level-1 trigger efficiency between Z+jet events and the other samples is due to imposing the leptonic branching fraction and pre-selection cuts. For the signal and qqZ background the Higgs boson and the Z were forced to decay to muons. For the $t\bar{t}$ background two muons with $p_T > 20$ and 10 GeV/c from any source were required at the generation level. For the Z+jet background, on the contrary, all leptonic (electron, muon, τ) decay channels were generated and no pre-selection cuts were applied on the muons.

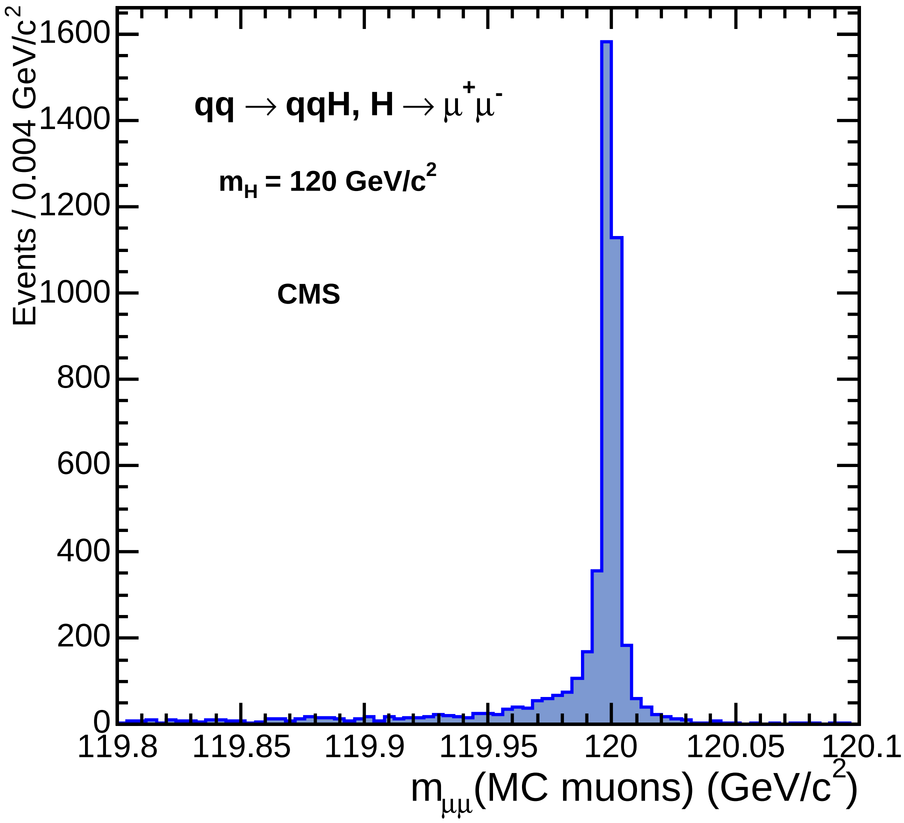

Figure 6.5: Invariant di-muon mass from the generated (MC) muons in the $qq \rightarrow qqH$, $H \rightarrow \mu^+\mu^-$ signal events with $m_H = 120$ GeV/c^2.

6.11.2 Selection Cuts on Muons

In the off-line analysis the events with at least two reconstructed muons with $p_T > 20$ GeV/c and $|\eta| < 2.4$ were first searched for. The muon isolation was performed in the tracker demanding that no track with $p_T > 1$ GeV/c was found in the cone of $\Delta R < 0.4$ around the muon direction. This p_T cut and the strong isolation cuts ensure the suppression of the potential $b\bar{b}$+jets background. Efficiency of the isolation on the reconstructed muons is 69% in the signal events and 42% in the $t\bar{t}$ background. The event selection was continued for the events with exactly two isolated opposite sign muons.

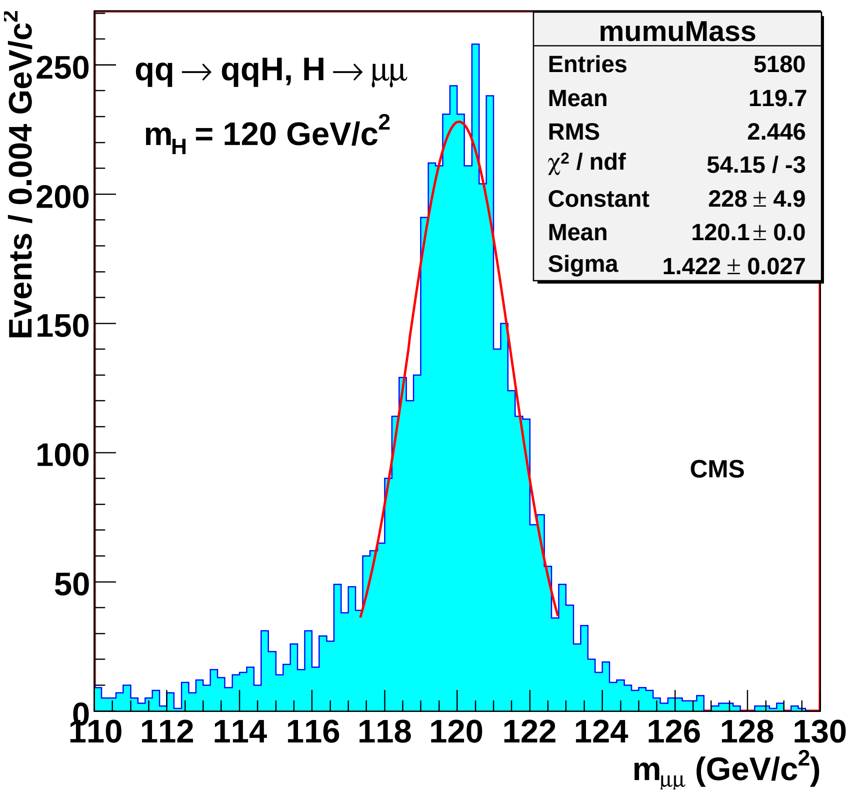

Figure 6.6: Invariant di-muon mass from the reconstructed muons in the $qq \rightarrow qqH$, $H \rightarrow \mu^+\mu^-$ signal events with $\mathrm{m}_H = 120$ GeV/c^2 and with muon selection cuts.

Fig. 6.5 shows the Monte-Carlo generated invariant mass peak for $qq \rightarrow qqH, H \rightarrow \mu^+\mu^-$ with $m_H = 120\ GeV/c^2$. The mass distribution has a tail at low mass values due to the internal bremsstrahlung from muons. In about 18% of the signal events one of the selected muons was found to radiate a photon with a $p_T > 1$ GeV/c^2. In about 1.7% of events both of the selected muons radiate such a photon. The invariant mass from the reconstructed muons is shown in Fig. 6.6. The Gaussian fit yields a mass resolution of

1.18% and the Higgs boson mass of 120.1 GeV/c^2.

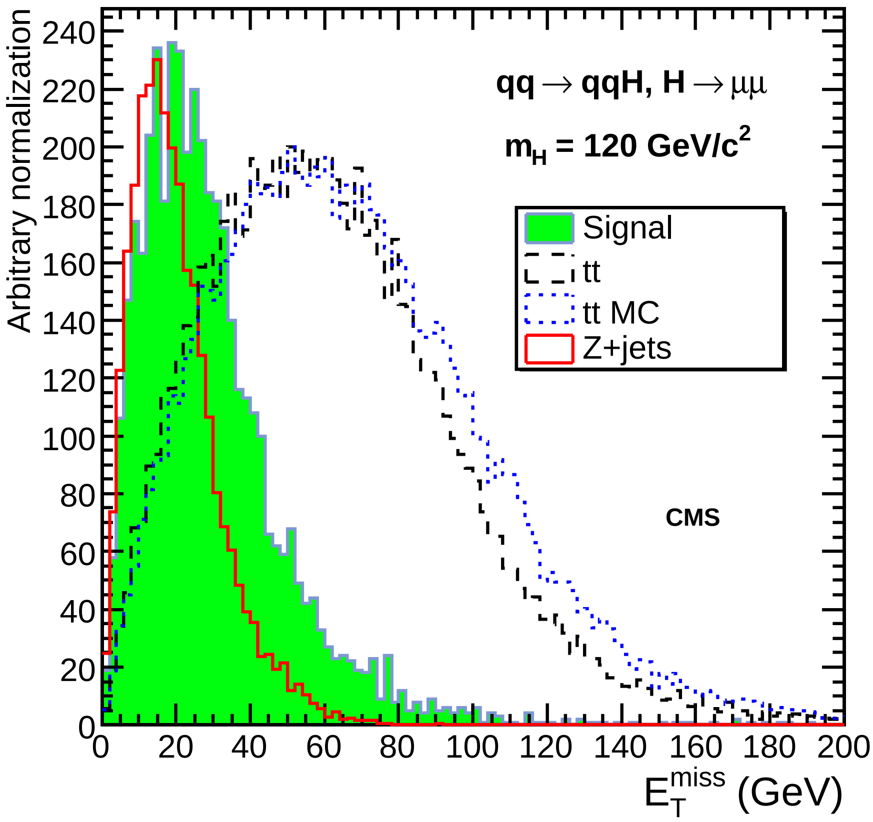

Figure 6.7: Reconstructed missing transverse energy for the signal events (filled histogram), for the $t\bar{t}$ background (dashed line) and for the Z+jets background (solid line). The generated (MC) missing transverse energy is shown for the $t\bar{t}$ background (dotted line).

6.11.3 Central Event Cuts

Fig. 6.7 shows the reconstructed missing transverse energy (E_T^{miss}) for the signal and for the $t\bar{t}$ and Z+jet backgrounds. An upper bound of $E_T^{miss} < 50$ GeV reduces the $t\bar{t}$ background with a factor of 3.9. A transverse momentum scale of $O(m_W)$ is expected for the Higgs boson in the $qq \to qqH$ process, while the p_T distribution is expected steeply falling in the Z+jets background. The p_T distribution for the selected muon pair is shown in Fig. 6.8 for the signal and for the $t\bar{t}$, Z+jets and qqZ backgrounds. A lower bound of

$p_T^{\mu\mu} > 60$ GeV/c suppresses the Z+jets background with a large factor of ~ 12.5.

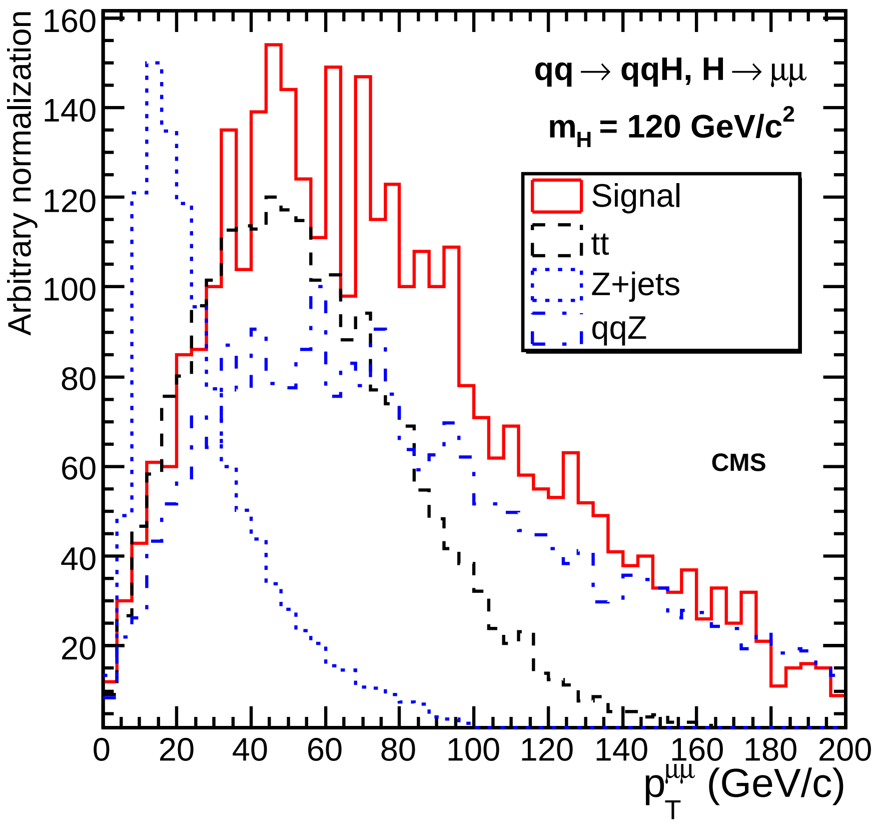

Figure 6.8: Di-muon transverse momentum distribution for the signal (solid line), the $t\bar{t}$ background (dashed line), the Z+jets background (dotted line) and the qqZ background (dad-dotted line).

Table 6.1 shows the number of events for the signal and backgrounds in the mass window of $118 < m_{\mu\mu} < 122$ GeV/c^2. This window was found to be the most optimal for the signal significance. Due to this small mass window, the Monte Carlo statistics in the window is low in particular for the Z+jet background, generated in a wide mass range in the reconstructed event samples. For the estimate of the forward jet tagging efficiencies the mass window was somewhat opened ($100 < m_{\mu\mu} < 140$ GeV/c^2) and the muon isolation, $p_T^{\mu\mu}$ and E_T^{miss} cuts were assumed to decouple from the forward jet tagging cuts.

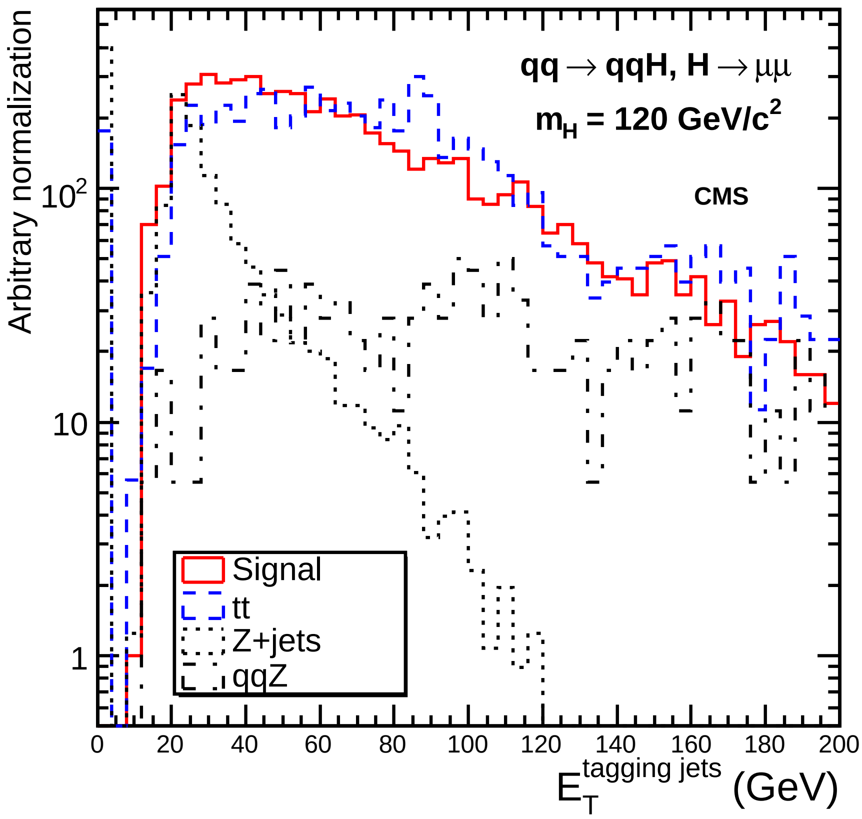

Figure 6.9: Distribution of transverse energy for the tagging jets in the signal events (solid line), in the $t\bar{t}$ background (dashed line), in the Z+jets background (dotted line) and in the qqZ background (dash-dotted line) with the central event cuts.

6.11.4 Forward Jet Tagging in $qq \to qqH$

An algorithm of searching the two most energetic hadronic jets in the full rapidity range and requiring these jets to be in opposite η hemispheres was used. As the dynamics of the forward jets is largely independent of the decays of the central objects, the Higgs boson and the W and Z bosons for the backgrounds, the tagging procedure studied in Ref. [25] for the similar mass scale was adopted in this work. Fig. 6.9 shows the E_T distribution of the forward jets in the signal events and in the $t\bar{t}$, Z+jets and qqZ backgrounds. The selected jets are more energetic in the signal process than in the $t\bar{t}$ and Z+jets backgrounds. To avoid underestimation of the Z background, generated with the $q\bar{q} \to gZ$ and $qg \to qZ$

processes with $10 < \hat{p}_T^q < 100$ GeV/c, the E_T threshold was set to a low value of 20 GeV on the corrected jet energies and no cut was set on the energy of the jet. The distributions for the qqZ background are affected with generator level cuts used for this background. The larger probability of a quark line to emit a Z boson than to emit a Higgs boson can also lead to some differences between the signal events and the qqZ background.

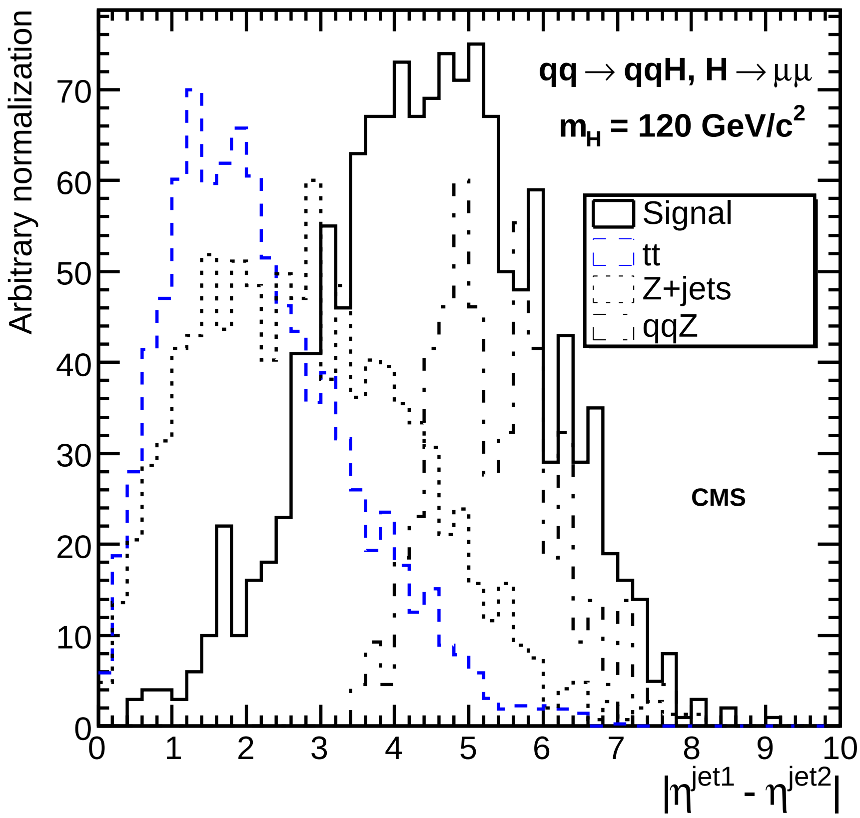

Figure 6.10: Distribution of $|\eta^{jet1} - \eta^{jet2}|$ for the tagging jets in the signal events (solid line), in the $t\bar{t}$ background (dashed line), in the Z+jets background (dotted line) and in the qqZ background (dash-dotted line) with the transverse energy cut for the tagging jets and with the central event cuts.

The mechanism of the weak gauge boson fusion is expected to lead to large rapidity gap between the two quark jets. Fig. 6.10 shows the η difference of the two selected jets for the signal events and for the Z+jets, $t\bar{t}$ and qqZ backgrounds. The Suppression of the low rapidity gap values for the qqZ background is due to the $|\eta^{jet1} -$

$\eta^{jet2}| > 4.2$ cut used at the generator level. Fig. 6.11 shows the cut efficiencies for the signal and for the $t\bar{t}$ and Z+jets backgrounds as a function of lower bound on $|\eta^{jet1} - \eta^{jet2}|$. The cut $|\eta^{jet1} - \eta^{jet2}| > 4.5$ is selected and suppresses the Z+jets and $t\bar{t}$ backgrounds by factors of ~ 7 and ~ 30, respectively.

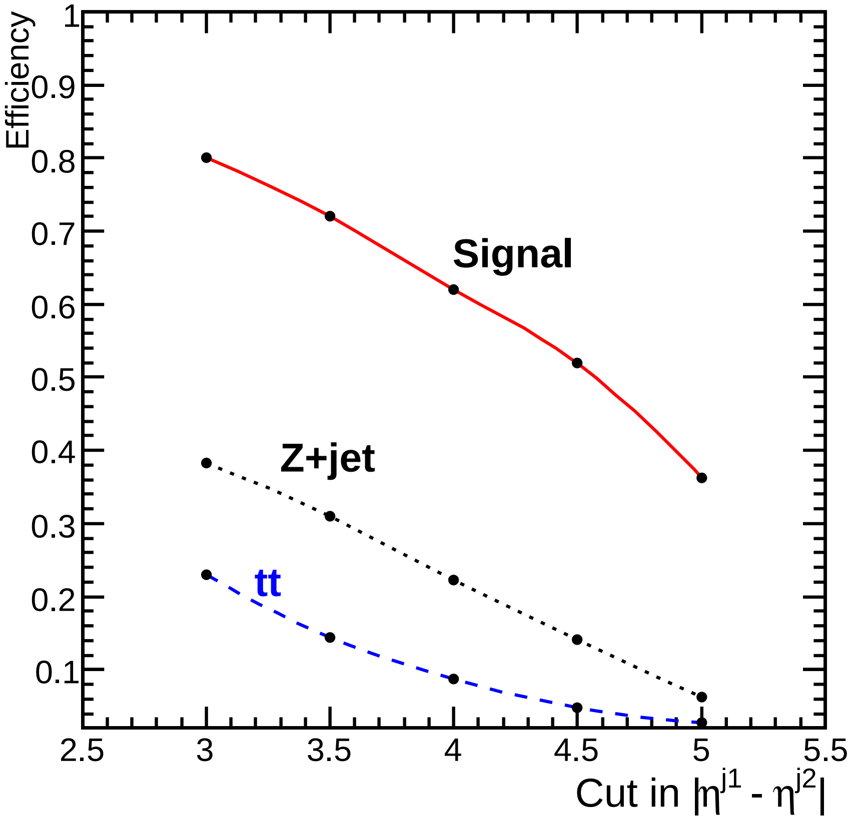

Figure 6.11: Efficiencies for for the signal (solid line), for the $t\bar{t}$ background (dashed line) and for the Z+jets background (dotted line) as a function of lower bound in $|\eta^{jet1} - \eta^{jet2}|$.

The large rapidity gap and the large jet energy in the qq$\rightarrow qqH$ and $qq \rightarrow qqZ$ processes is reflected in the invariant mass of the tagging jets. Fig. 6.12 shows the distribution of the invariant mass for the signal and for the Z+jets, $t\bar{t}$ and qqZ backgrounds with the $|\eta^{jet1} - \eta^{jet2}| > 4.5$ cut. The Cut efficiencies for the signal and backgrounds as function of lower bound in m_{jj} are shown in Fig. 6.13, including the $|\eta^{jet1} - \eta^{jet2}| > 4.5$ cut. The cut $m_{jj} > 1$ TeV$/c^2$ is found to be optimal for the signal significance. This cut suppresses further the Z+jets background with a factor of ~ 13. The reduction for the $t\bar{t}$ background is somewhat smaller, ~ 4, due to the tendency of more energetic jets in this background.

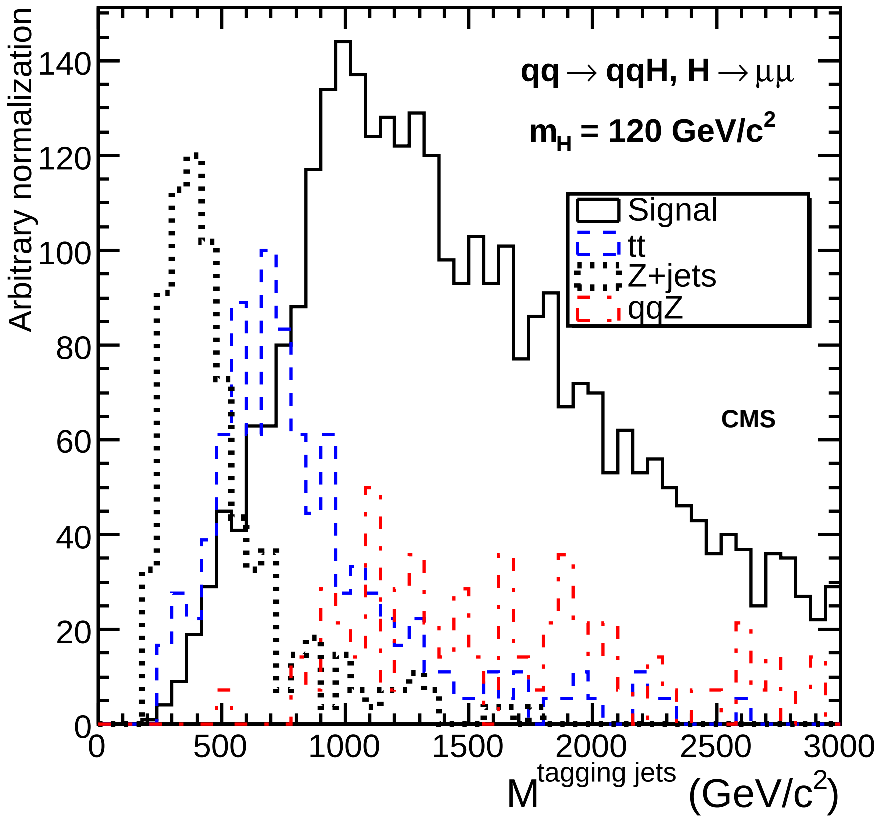

Figure 6.12: Invariant mass reconstructed from the two tagging jets in the signal events (solid line), in the $t\bar{t}$ background (dashed line), in the Z+jets background (dotted line) and in the qqZ background (dash-dotted line) with the transverse energy cut and the $|\eta^{jet1} - \eta^{jet2}| > 4.5$ cut for the tagging jets and with the central event cuts.

6.11.5 Central Jet Veto

Due to the absence of color exchange in the weak gauge boson fusion, a low jet activity is expected in the η region between the two tagging jets. This feature can be exploited to suppress further the backgrounds. The corrected hadronic jets were searched for within $\eta^{min} + 0.5 < \eta < \eta^{max} - 0.5$, where $\eta^{min}(\eta^{max})$ are the η values of the tagging jets in the two hemispheres. Fig. 6.14 shows the efficiency for vetoing these jets for signal and for the $t\bar{t}$ background as a function of the jet E_T threshold, including the forward jet tagging cuts. The efficiency curves for the signal and for the $t\bar{t}$ background have similar behavior. The lowest possible threshold $E_T = 20$ GeV is however selected as the jet veto is important for the suppression of the Z production in multi-jet final states with the ALPGEN generation. A signal efficiency of 69% and a rejection factor of 4.2 against the $t\bar{t}$ background is obtained.

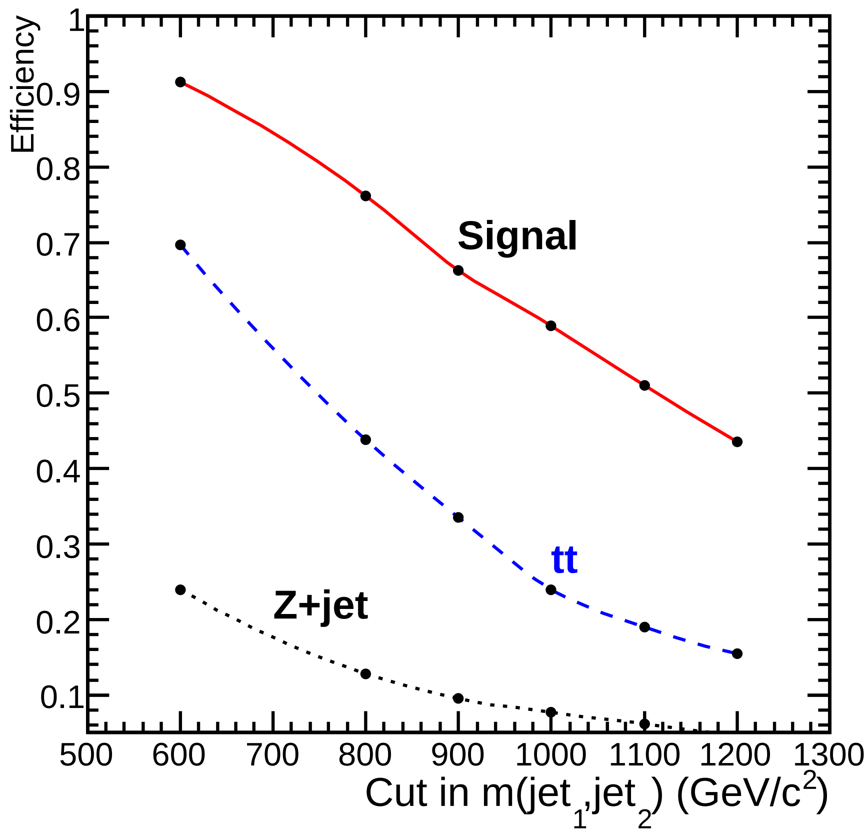

Figure 6.13: Efficiencies for the signal (solid line), for $t\bar{t}$ background (dashed line) and for the Z+jets background (dotted line) as function of lower bound in m_{jj},including the $|\eta^{jet1} - \eta^{jet2}| > 4.5$ cut.

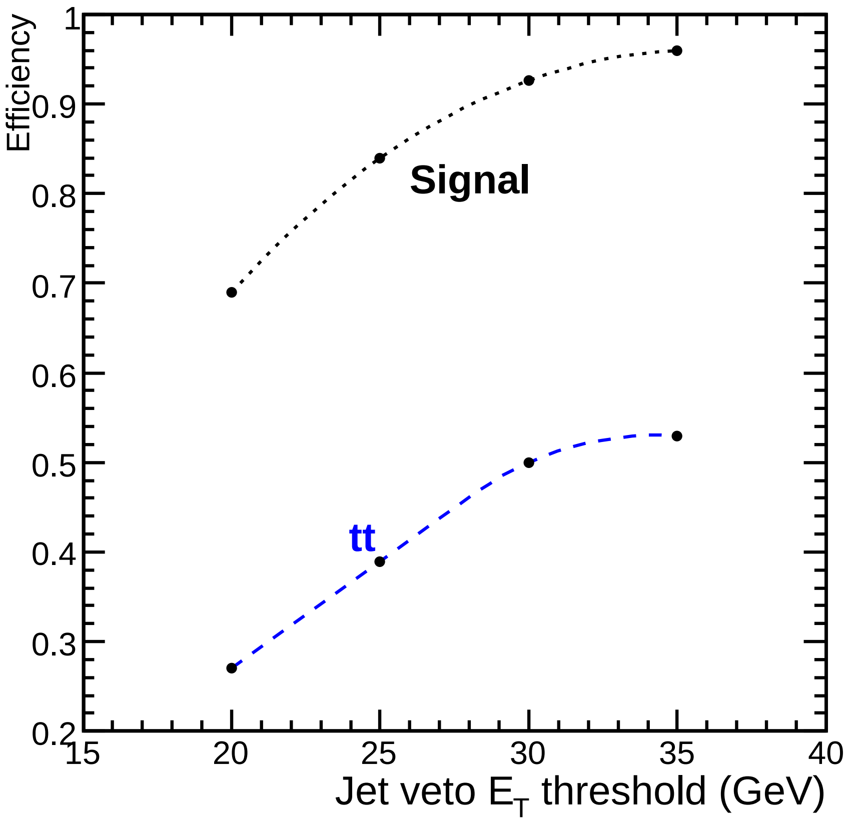

Figure 6.14: Fraction of events passing the jet veto cut as a function of the jet threshold for the signal events (solid line), for the $t\bar{t}$ background (dashed line) and for the Z+jets background (dotted line), including the cuts $|\eta^{jet1} - \eta^{jet2}| > 4.5$ and $m_{jj} > 1$ TeV/c^2.

6.11.6 Comparison of PYTHIA and ALPGEN Generation for the QCD Z Production

In this study the background from Z production in the QCD processes was generated with PYTHIA with the $q\bar{q} \to gZ$ and $qg \to qZ$ subprocesses in the interval of $10 < \hat{p}_T^q < 100$ GeV/c. These processes lead to events with a Z boson, one energetic jet from the hard process and jets from the parton shower processes. As the event selection requires two energetic jets in the opposite hemispheres the PYTHIA generation could then lead to underestimation of this background. To avoid underestimation of the background, a low E_T threshold of 20 GeV was selected on the corrected jet energies and no cut was set on

Table 6.1: Cross section times branching fraction for the signal process and for the Z+jets, $t\bar{t}$ and qqZ backgrounds, number of events and efficiency for the selection cuts with an integrated luminosity of 60 fb^{-1}. For the Z+jets background all leptonic decay channels of Z, including the τ's, have been generated and no pre-selection cuts have been applied at the generator level. For the $t\bar{t}$ and Z+jets backgrounds, the final number of events in the mass window is obtained with cut factorization.

	signal	qqZ	Z+jets	$t\bar{t}$
$\sigma \times BR$, pre-selections	1.1 fb	86 fb	5.1 nb	20.9 pb
Events for 60 fb^{-1}	66	5160	3.05×10^8	1.25×10^6
Level-1 trigger	61.8 (93%)	5142 (99%)	1.18×10^8 (39%)	1.25×10^6 (99%)
High level trigger	57.5 (93%)	4930 (96%)	4.84×10^7 (41%)	1.00×10^6 (80%)
Rec. primary vertex	56.6 (98%)	4863 (99%)	4.74×10^7 (98%)	9.97×10^5 (99%)
$p_T(\mu) > 15$ GeV/c	41.9 (74%)	3668 (75%)	2.09×10^7 (44%)	5.12×10^5 (51%)
Muon isolation	28.8 (69%)	2546 (69%)	1.44×10^7 (69%)	2.16×10^5 (42%)
$E_T^{miss} < 50$ GeV	25.7 (89%)	2179 (86%)	1.37×10^7 (95%)	5.77×10^4 (27%)
$p_T^{\mu\mu} > 60$ GeV	16.6 (64%)	1396 (64%)	1.10×10^6 (8.0%)	3.00×10^4 (52%)
$118 < m_{\mu\mu} < 122$ GeV/c^2	11.1 (67%)	2.06 (0.2%)	2968 (0.3%)	619 (2%)
$\eta_{j1} \times \eta_{j2} < 0$	8.5 (77%)	1.88 (91%)	1033 (35%)	273 (44%)
$E_T^{jet}(f,b) > 20$ GeV	7.7 (90%)	1.81(96%)	373 (36%)	259 (95%)
$\Delta\eta^{jj} \geq 4.5$	4.0 (52%)	1.52 (84%)	52.6 (14%)	8.0 (3%)
$M_{jj} > 1$ TeV	2.4 (59%)	1.36 (89%)	4.05 (8%)	1.9 (23%)
$E_T^{jet}(veto) < 20$ GeV	1.7 (69%)	0.95 (70%)	2.28 (56%)	0.45 (24%)

the energy of the jet. ALPGEN is a matrix element generator which is dedicated to the study of multiparton hard processes in hadronic collisions. Table 6.2 shows comparison of production cross sections for the Z+jet production with ALPGEN and PYTHIA. The leptonic Z decays to electrons, muons and τ's are are generated. The ALPGEN samples contain exclusive 2, 3, 4 and 5 jet final states, and are generated for $\hat{m}_{\ell\ell} > 40$ GeV/c^2. This cut is included in the event generation with PYTHIA, otherwise taken identical to that used in Table 6.1. The jets are reconstructed at the generator level exploiting the PYTHIA jet reconstruction package. The main selection cuts on leptons and jets are applied on the events. The ALPGEN generation, with more energetic jets, leads to a higher efficiency for the forward jet tagging cuts (2.2×10^{-3} versus 1.1×10^{-3} for PYTHIA). For the same reason the efficiencies for the central jet veto cut are lower in the ALPGEN generation than in the PYTHIA generation (12% versus 33% for PYTHIA), in particular in the multi-jet components. The cross section after all cuts with PYTHIA supersedes that with ALPGEN, thus indicating that the level of the Z+jet background in Table 6.2 is not underestimated.

Table 6.2: Comparison of production cross sections as a function of main selection cuts at the generator level for the Z+jet production with ALPGEN and PYTHIA, including Z decays to leptons (electron, muon, tau). Shown are the cross sections for exclusive Z production with ALPGEN with 2-5 jets (2j-5j) and for Z+jets production with PYTHIA generated with $10 < \hat{p}_T < 100$ GeV/c and $\hat{m}_{\ell\ell} > 40$ GeV/c^2. Electrons and muons are selected. The numbers after all cuts have a statistical uncertainty of 30-50%.

	2j	3j	4j	5j	2j-5j	PYTHIA
$\sigma \times BR$(pb)	230	66	17	4.0	317	4500
2ℓ,$p_T > 15GeV/c$	104.7	30.4	7.8	1.8	144.7	830.9
$p_T^{\ell\ell} > 60$ GeV/c	34.8	13.5	4.1	1.1	53.5	60.4
2j, $\eta_{j1} \times \eta_{j2} < 0$	10.4	5.0	1.6	0.45	17.2	18.8
$\Delta\eta^{jj} \geq 4.5$	0.16	0.14	3.4×10^{-2}	1.5×10^{-2}	0.35	0.12
$M_{jj} > 1$ TeV	4.7×10^{-2}	5.1×10^{-2}	1.4×10^{-2}	1.2×10^{-2}	0.12	6.7×10^{-2}
$E_T^{jet}vt. < 20$ GeV	8.4×10^{-3}	5.3×10^{-3}	3.6×10^{-4}	2.6×10^{-4}	1.4×10^{-2}	2.2×10^{-2}

6.11.7 Backgrounds from WW+jets and $b\bar{b}$+jets

The WW+jets background with $W \to \mu\nu$ decays and the $b\bar{b}$+jets background with b's decaying semi-leptonically were not simulated in this study. The WW+jets background with $W \to \mu\nu$ was estimated exploiting the event samples generated with ALPGEN. The cross section for the WW+2jet events is 1.22 pb. The jets were reconstructed with the PYTHIA jet reconstruction package and the event selection procedure of Table 6.2 was applied on the events. This selection leads to a cross section of 6.5×10^{-5} pb, which is about 0.8% of the cross section obtained for the Z+2jet events. The upper bound on the missing E_T, which cannot be applied in a particle level simulation, would further reduce this background. The $b\bar{b}$+jets events with semileptonic b decays have been studied for the MSSM Higgs boson searches in the $H/A \to \tau\tau \to e\mu + X$ channel [26]. Requirement of the leptonic decays, trigger, lepton p_T cuts and isolation has been found to lead to a rejection factor of $\sim 10^6$. The lepton isolation, which is the main asset against the $b\bar{b}$ background, has been taken identical to that used in this work. The p_T cuts, 19 GeV/C for the muon and 29 GeV/c for the electron, are somewhat more stringent than the muon p_T threshold used in this work. Assuming the efficiencies of the remaining selection cuts to be close to those for the Z+jets events, an estimate of 4×10^{-3} events in the mass window can be obtained. It can be concluded that the backgrounds from WW+jets and $b\bar{b}$+jets are significantly lower than main backgrounds and can be neglected with the event selection used in this work.

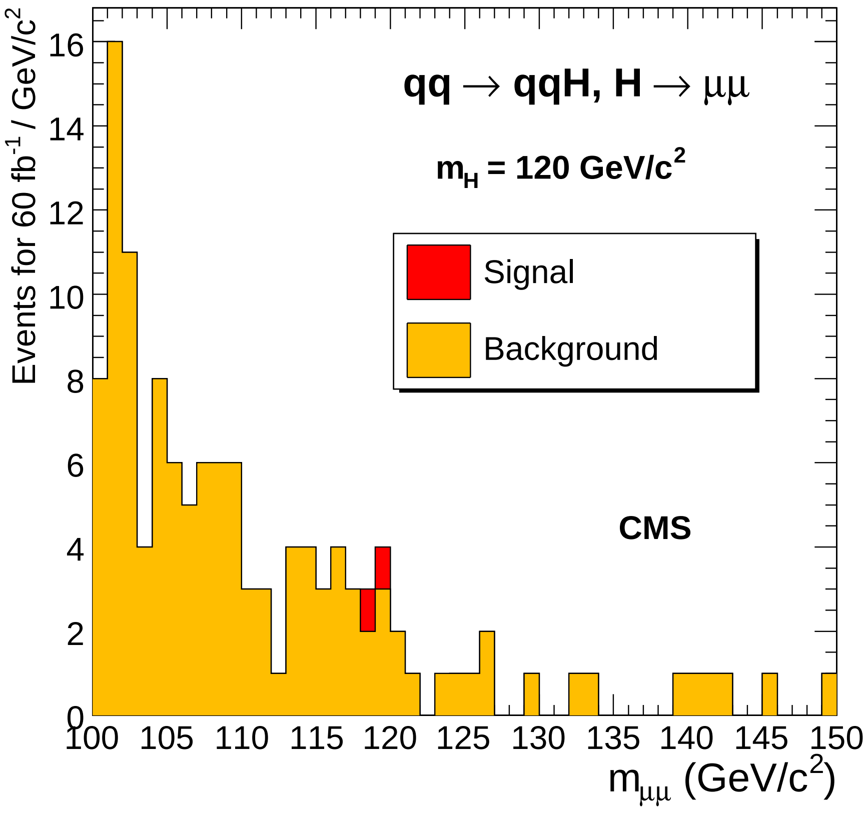

Figure 6.15: Reconstructed Higgs boson mass for the signal with $m_H = 120$ GeV/c^2 and for the total background for an integrated luminosity of 60 fb^{-1}.

6.12 Effect of Jet Energy Scale Uncertainty on Background Determination

Fig. 6.15 shows the signal superimposed on the total background for 60 fb^{-1} with all selection cuts. Although the signal mass resolution is good, the signal visibility cannot be reached with this integrated luminosity and the background determination from the side bands is not possible. Before any evidence in this channel, the Higgs boson mass can be assumed to be already known from the inclusive $H \rightarrow \gamma\gamma$ search in CMS [26]. The main source of systematic uncertainty on the determination of the background level in the known signal area is the uncertainty of the jet energy scale through the forward jet tagging and central jet veto methods. The jet energy scale uncertainty in the CMS detector increases from 3% for jets with $E_T > 50$ GeV to 10% for jets with $E_T < 20$ GeV [26]. Fig. 6.16 shows the average uncertainty on the selected number of events (including a 10% uncertainty for the E_T^{miss} measurement) on the Z+jets, $t\bar{t}$ and qqZ backgrounds as a function of the jet energy scale uncertainty. The Z+jets and $t\bar{t}$ backgrounds are found to be sensitive to the increase of the uncertainty of the jet energy scale, thus indicating the need for a study of the Z+jets background with a matrix element Monte-Carlo generator.

An upper bound study [28] was also performed by assuming an uncertainty of 100% for the present background determination. It was found that an upper bound of 6.6 fb is obtained for $qq \rightarrow qqH, H \rightarrow \mu^+\mu^-$ at 95% CL for $m_H = 120$ GeV/c^2.

6.13 Summary

The Higgs simulation study in the channel $qq \rightarrow qqH, H \rightarrow \mu^+\mu^-$ presented in this chapter, has been performed with multi-purpose event generator, PYTHIA and some comparison also performed using ALPGEN. The CMS detector response was simulated using the package OSCAR. It is an application of the Geant4 toolkit for detector description and simulation, which includes and uses information about the magnetic field. OSCAR

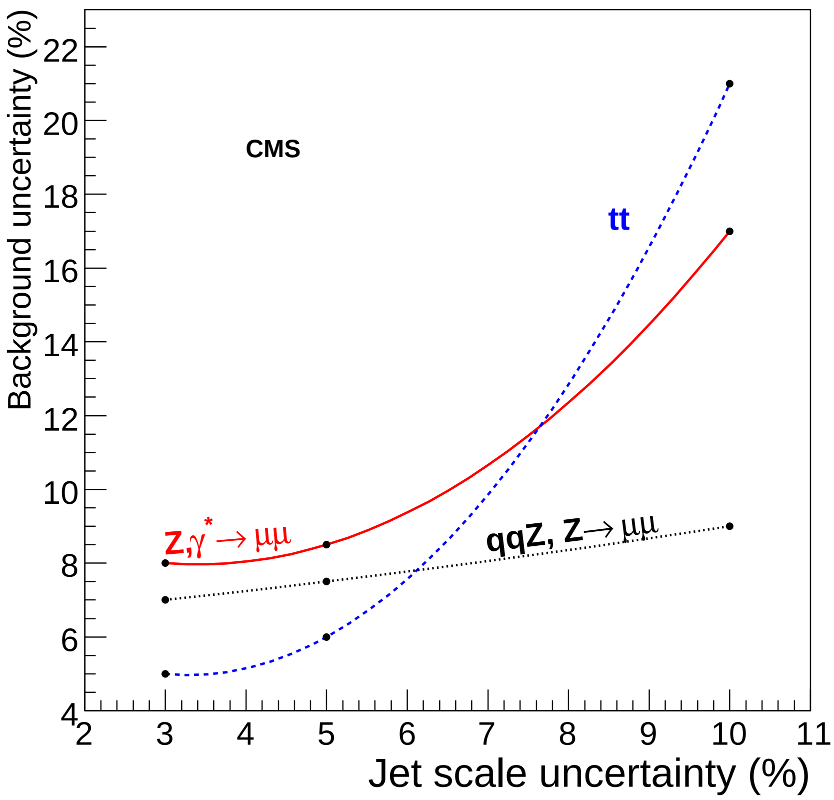

Figure 6.16: Uncertainty on the number of events in the Z+jets background (solid line), $t\bar{t}$ background (dashed line) and in the qqZ background (dotted line) as a function of the jet energy scale uncertainty. Uncertainty of 10% is included in the E_T^{miss} scale. The uncertainty due to Monte-Carlo statistics on the estimate is about 30% for the Z+jets and $t\bar{t}$ backgrounds.

reads the individual generated events and simulates the effects of energy loss, multiple scattering and showering in the detector materials. The digitization (simulation of the electronic response), the emulation of the level-1 trigger and high level trigger (HLT), and the offline reconstruction of physics objects is done using the CMS full-reconstruction ORCA package.

Discovery potential for the SM Higgs boson in the $H \to \mu^+\mu^-$ channel with $m_H = 120$ GeV/c^2 in the Weak Gauge Boson fusion (WBF) at the low luminosity was studied, with full simulation and reconstruction of the CMS detector and using cut-based analysis method. A resolution of 1.2% was obtained for the reconstructed Higgs boson mass. The main backgrounds from Z+jets, $t\bar{t}$ and qqZ events were simulated. An efficient background suppression was obtained tagging the forward quark jets in the $qq \rightarrow qqH$ production process. The analysis leads to a signal-over-background ratio of 46% [29].

For the final significance estimate for this channel, generation of the main background from Z+jets with a matrix element Monte-Carlo generator is needed. Assuming an uncertainty of 100% for the present background determination an upper bound of 6.6 fb is obtained for $qq \rightarrow qqH, H \rightarrow \mu^+\mu^-$ at 95% CL for $m_H = 120$ GeV/c^2 [30].

Bibliography

[1] A. Giammanco and A. Perrotta, Fast Simulations of the ATLAS and CMS experiments at LHC, presented at the INFN Workshop on Monte Carlo, Physics and Simulation at LHC, CMS CR 2007/010.

[2] T. Sjostrand et al., High-Energy Physics Event Generation with PYTHIA 6.1, Comput. Phys. Commun. 135 (2001) 238, http://www.thep.lu.se/ torbjorn/Pythia.html.

[3] M.L. Mangano et al., ALPGEN, a generator for hard multiparton processes in hadronic collisions, JHEP 0307 001, 2003, hep-ph/0206293.

[4] H. Baer et al., ISAJET, A Monte Carlo Event Generator for pp, $\bar{p}p$, and e^+e^- Interactions, http://www.hep.fsu.edu/ isajet/.

[5] G. Corcella et al., HERWIG 6.5, JHEP 0101 (2001) 010 [hep-ph/0011363]; hep-ph/0210213, http://hepwww.rl.ac.uk/theory/seymour/herwig/.

[6] V. Karimaki et al., User's Guide for CMS Physics Generators Interface CMKIN Version 4, CMS IN 2004/052.

[7] S. Agostinelli et al. (GEANT4 Collaboration), GEANT4: A simulation toolkit, Nucl. Instrum. Meth. A 506 (2003) 250-303.

[8] OSCAR, Object oriented Simulation for CMS Analysis and Reconstruction, http://cmsdoc.cern.ch/oscar/.

[9] ORCA, CMS reconstruction package, http://cmsdoc.cern.ch/orca/.

[10] FAMOS, CMS fast simulation package, http://cmsdoc.cern.ch/FAMOS/.

[11] CMSSW, CMSSW application framework, http://cmsdoc.cern.ch/cms/cpt/Software/html/General/.

[12] R. Brun et al., ROOT, An Object-Oriented Data Analysis Framework, http://root.cern.ch/.

[13] C. Eck et al., LHC computing Grid Technical Design Report, LCG TDR 1, CERN LHCC 2005/024.

[14] P. Buncic et al., Architectural Roadmap Towards Distributed Analysis, CERN LCG 2003/033.

[15] ASAP, Arda Support for cms Analysis and Production, https://twiki.cern.ch/twiki/bin/view/LCG/ARDA-CMS-ASAP.

[16] G. Masetti and S. Marcellini, Search for the MSSM Neutral Higgs Bosons in the Two Muons Channel, CMS AN 2005/033.

[17] Tao Han and Bob McElrath, Phys. Lett. B 528 (2002) 81, hep-ph/0201023.

[18] T. Plehn and D. Rainwater, Phys. Lett. B 520, 108 (2001), hep-ph/0107180.

[19] R. Kinnunen, P. Mehtala, A. Zibellini, Study of the Standard Model Higgs Boson Decaying to Muons in CMS, CMS IN 2004/013.

[20] M. Spira, SM Higgs boson production cross sections at NLO and SM Higgs boson BRs, 2005, Available at http://cmsdoc.cern.ch/ anikiten/cms-Higgs/.

[21] A. Djouadi, J. Kalinowski and M. Spira, HDECAY: a program for Higgs Boson Decays in the Standard Model and its Supersymmetric Extension, hep-ph/9704448.

[22] N. Kauer, T. Plehn, D. Rainwater, D. Zeppenfeld, Physics Letters B 503 (2001) 113-120.

[23] F. Maltoni and T. Stelzer, MadEvent: Automatic event generation with MadGraph, JHEP,02 (2003).

[24] CMS Collaboration, Detector Performance and Software, Technical Design Report, vol. 1, CMS TDR 8.1, CERN LHCC 2006/001.

[25] C. Foudas, A. Nikitenko and M. Takahashi, Observation of the Standard Model Higgs Boson via H$\rightarrow \tau\tau \rightarrow$ lepton+jet Channel, CMS NOTE 2006/088.

[26] CMS Collaboration, CMS Technical Design Report: Physics Performance, vol. 2, J. Phys. G: Nucl. Part. Phys. 34 (2007) 995-1579.

[27] S. I. Bityukov, S. E. Erofeeva, N. V. Krasnikov and A. N. Nikitenko, Program for evaluation of significance, confidence intervals and limits by direct calculation of probabilities, Proceedings of PhyStat 2005, Sept. 2005, Oxford, UK.

[28] K. Cranmer, 'Progress, Challenges, and Future of Statistics for the LHC', PhyStat 2007, June 2007, CERN, Switzerland.

[29] Ashok Kumar, Suman Beri, Ritva Kinnunen, Study of Higgs Decay to dimuons, proceedings of XVII DAE HEP symposium, Dec. 2006, IIT, Kharagpur, India.

[30] Ashok Kumar, Suman Beri, Ritva Kinnunen, Search for the Standard Model Higgs Boson Decaying to Muons in the Weak Gauge Boson Fusion, CMS AN 2006/105.

Chapter 7

Conclusions and Outlook

The CMS hadron calorimeter is a sampling calorimeter with brass absorber and plastic scintillator tiles with wavelength shifting fibers for carrying the light to the readout device. The barrel hadron calorimeter was complimented with a outer hadron calorimeter to ensure high energy shower containment in CMS and its working as a tail catcher. Its importance relied in the energy measurement of jets in view of linearity and resolution. The performance of HO was depending on the quality of grooving of the tiles, painting on the sides, tightly packed tray assembly, good splicing and fine polishing of the fibers in the pigtail assembly.

HO is divided in to 5 rings ±2, ±1, 0 (with inner and outer scintillator layers). The scintillator tiles were fabricated and assembled in to a complete HO megatile called tray. The testing and quality control of the trays was done with three tests, Cosmic MIP test, sliding wire source Co^{60} test and collimated Cs^{137} X-Y scanner test. Testing of the assembled HO scintillator modules using cosmic test ensured the required light yield in terms of number of photoelectrons produced. The criteria was made and trays were accepted for some minimum number of photoelectron yield. All HO trays were exposed to radioactive source which was mounted on a tip of a stainless steel and was sent through tubes installed along megatiles. Radioactive wire sourcing ensures inter-calibration of individual tiles present inside the assembled HO tray. This test will also help in testing

HO detectors inside the CMS detector. X-Y scanner helped in testing signal output of HO trays at any of the desired point. All HO trays passed the stringent testing procedure and quality control. No damage was observed after shipment of HO trays from India to CERN when HO trays were cross-checked for stable response by using wire-source and collimated X-Y scanning at CERN.

The test beam data allowed us to evaluate and study the physics potential of the HCAL detectors. HO trays were mounted on the test beam motion table of H2 beam-line of the along with other hadron calorimeter (HCAL) detectors and electromagnetic calorimeter (ECAL) prototype. After calibrating ECAL using 100 GeV electron beam it was observed that (5 × 5) crystal matrix energy sum is sufficient to calculate the energy properly as the (7 × 7) sum adds only to the width of the distribution. The ECAL calorimeter was found to be linear with electron beam energies. After calibrating HCAL with 150 GeV muon beam, the pion data was analyzed and studied for different energies. The HCAL response was also found to be linear with pion beam energies. Constrained to the outside of the CMS tracker and ECAL, the HB was found to be thin to effectively absorb high energy pions specially near the central region. This may lead to degraded sensitivity for establishing new physics signals whose main signature is missing E_T. The pion interacts with organic scintillator in the sampling calorimeter and results in secondary particle cascades. The longitudinal deposition profiles for pions are characterized by a sharp peak near to the HCAL depth where secondaries are produced followed by a exponential fall-off. The average longitudinal hadron(pion) showers extend past the inner HCAL (mainly HB) located inside the magnetic coil mock up. Thus HO helps in measuring the high energy hadronic shower tail. Hence, the addition of sensitive detector layers of HO just outside the magnet ensures much smaller energy leakage and hence improvement in the energy resolution. The importance of HCAL test beam study relies in calculating preliminary calibration constants for the simulation and reconstruction softwares. It also helps in directing trigger related algorithms for real physics analysis.

Precisely because of the role of the Higgs bosons in the mass generation mechanism, they couple to the SM particles proportional to their masses. The $H \to \mu^+\mu^-$ channel would be the first observation for a Higgs boson to decay to second-generation fermions. It is necessary to confirm the proportionality of m_μ for the Higgs coupling $H\mu^+\mu^-$ as predicted by the SM and hence Higgs particle that generates mass for the weak boson is also responsible for mass generation of the second generation of fermions.

The observability of the Standard Model Higgs boson decay into two muons in the Vector Boson Fusion Higgs boson production $qq \to qqH$ was studied with the full detector simulation for Higgs boson mass 120 GeV at luminosity 2 $\times 10^{33}$ cm^{-2}s^{-1}. The events were selected by single or double isolated muon trigger. Off-line selections include upper cut 50 GeV on the missing E_T against $t\bar{t}$ background, lower cut 60 GeV on di-muon p_T against Z+jets background, di-muon mass window 4 GeV and a set of WBF cuts for tagging jets. The WBF cuts include rapidity separation 4.5 between two highest E_T jets, lower cut 1 TeV on di-jet invariant mass and central jet veto. The dominant backgrounds considered were QCD and electroweak Z+2jets and $t\bar{t}$. The background from WW+jets and $b\bar{b}$+jets was found to be negligible. The QCD Z+jets background was generated using PYTHIA Z+j process. Comparison with ALPGEN Z+jets generation shows that PYTHIA does not underestimate Z+2jets background after event selections. The electroweak Z+2jets background was generated with MadGraph and $t\bar{t}$ was generated by PYTHIA. After all selections 1.7 event of signal and 3.7 events of the total background are expected in the di-muon mass window 118-122 GeV for 60 fb^{-1}. Assuming the background uncertainty of 100 % the upper limit 6.6 fb can be set up at 95 % confidence level on the cross section times branching ratio $qq \to qqH$, $H \to \mu^+\mu^-$, mode for Higgs boson mass 120 GeV at 60 fb^{-1} luminosity. For the final significance estimate for this channel, generation of the main background from Z+jets with a matrix element Monte-Carlo generator is needed. In the inclusive search the backgrounds, mainly from Z production, remain large under the tiny signal peak and therefore large luminosity is required for a significant signal.